NASA/TP-2007-214612

Displacement Theories for In-Flight Deformed Shape Predictions of Aerospace Structures

William L. Ko, W. L. Richards, and Van T. Tran
NASA Dryden Flight Research Center
Edwards, California

NASA STI Program ... in Profile

Since its founding, NASA has been dedicated to the advancement of aeronautics and space science. The NASA scientific and technical information (STI) program plays a key part in helping NASA maintain this important role.

The NASA STI program is operated under the auspices of the Agency Chief Information Officer. It collects, organizes, provides for archiving, and disseminates NASA's STI. The NASA STI program provides access to the NASA Aeronautics and Space Database and its public interface, the NASA Technical Report Server, thus providing one of the largest collections of aeronautical and space science STI in the world. Results are published in both non-NASA channels and by NASA in the NASA STI Report Series, which includes the following report types:

- TECHNICAL PUBLICATION. Reports of completed research or a major significant phase of research that present the results of NASA programs and include extensive data or theoretical analysis. Includes compilations of significant scientific and technical data and information deemed to be of continuing reference value. NASA counterpart of peer-reviewed formal professional papers but has less stringent limitations on manuscript length and extent of graphic presentations.

- TECHNICAL MEMORANDUM. Scientific and technical findings that are preliminary or of specialized interest, e.g., quick release reports, working papers, and bibliographies that contain minimal annotation. Does not contain extensive analysis.

- CONTRACTOR REPORT. Scientific and technical findings by NASA-sponsored contractors and grantees.

- CONFERENCE PUBLICATION. Collected papers from scientific and technical conferences, symposia, seminars, or other meetings sponsored or cosponsored by NASA.

- SPECIAL PUBLICATION. Scientific, technical, or historical information from NASA programs, projects, and missions, often concerned with subjects having substantial public interest.

- TECHNICAL TRANSLATION. English-language translations of foreign scientific and technical material pertinent to NASA's mission.

Specialized services also include creating custom thesauri, building customized databases, and organizing and publishing research results.

For more information about the NASA STI program, see the following:

Access the NASA STI program home page at *http://www.sti.nasa.gov.*

- E-mail your question via the Internet to help@sti.nasa.gov.

- Fax your question to the NASA STI Help Desk at (301) 621-0134.

- Phone the NASA STI Help Desk at (301) 621-0390.

- Write to:
  NASA STI Help Desk
  NASA Center for AeroSpace Information
  7115 Standard Drive
  Hanover, MD 21076-1320

Displacement Theories for In-Flight Deformed Shape Predictions of Aerospace Structures

William L. Ko, W. L. Richards, and Van T. Tran
NASA Dryden Flight Research Center
Edwards, California

October 2007

PATENT PENDING NOTICE

The **invention** described in this report is the subject of a currently pending patent application: ***Real-Time Structural Shape Sensing Techniques using Surface Strain Sensor Measurements*** (Inventors: William Leslie Ko and W. Lance Richards) before the U.S. Patent and Trademark Office and, therefore, those interested in using the invention should contact NASA for more information.

Cover art: NASA Dryden Flight Research Center, photograph ED01-0209-2.

ERRATA

NASA/TP-2007-214612

Displacement Theories for In-Flight Deformed Shape Predictions of Aerospace Structures

William L. Ko, W.L. Richards, and Van T. Tran

October 2007

Page 14, equation (24) should read as follows:

$$
y(x) = \underbrace{\int_{x_{i-1}}^{x} \tan\theta(x)\,dx}_{\text{Integration of slope}} + \underbrace{y_{i-1}}_{\substack{\text{Deflection} \\ \text{at } x_{i-1}}} = \underbrace{\int_{x_{i-1}}^{x}\int_{x_{i-1}}^{x} \frac{\varepsilon(x)}{c(x)}\,dx\,dx}_{\text{Deflection increment}} + \underbrace{\int_{x_{i-1}}^{x} \tan\theta_{i-1}\,dx}_{\substack{\text{Deflection at } x \\ \text{due to } \tan\theta_{i-1}}} + \underbrace{y_{i-1}}_{\substack{\text{Deflection} \\ \text{at } x_{i-1}}} \quad ; \quad x_{i-1} \le x \le x_i
$$

Issued June 2009

CONTENTS

ABSTRACT

Displacement theories are developed for a variety of structures with the goal of providing real-time shape predictions for aerospace vehicles during flight. These theories are initially developed for a cantilever beam to predict the deformed shapes of the Helios flying wing. The main structural configuration of the Helios wing is a cantilever wing tubular spar subjected to bending, torsion, and combined bending and torsion loading. The displacement equations that are formulated are expressed in terms of strains measured at multiple sensing stations equally spaced on the surface of the wing spar. The bending and torsion strain data are to be input to the displacement equations for calculations of slopes, deflections, and cross-sectional twist angles of the wing spar at the strain-sensing stations. Displacement theories for other structures, such as tapered cantilever beams, two-point supported beams, wing boxes, and plates also are developed. The accuracy of the displacement theories is successfully validated by finite-element analysis and classical beam theory using input-strains generated by finite-element analysis. The displacement equations and associated strain-sensing system (such as fiber optic sensors) create a powerful means for in-flight deformation monitoring of aerospace structures. Because local strains are used as inputs for the structural deformation predictions described in this report, this method serves multiple purposes for structural shape sensing, loads monitoring, and structural health monitoring. Ultimately, the calculated displacement data can be visually displayed to the ground-based pilot or used as input to the control system to actively control the shape of structures during flight. The displacement theories could also be easily applied to calculate the deformed shapes of a variety of high-aspect-ratio flexible structures, aircraft wing rotorcraft vehicles, space vehicles, wind turbine blades (for the alternative energy community), space-based structures (such as booms and antennae), and long-span civil structures (such as bridges and dams).

NOMENCLATURE

A	cross-sectional area of uniform cantilever beam, in^2
Al	aluminum
a	mean radius of 4-ply composite tube wall and aluminum tube wall, or mean radius of Helios 31-ply reinforced spar cap wall, in.
c	outer radius of tubular beam, or half depth of beam, in.
c_i	distance from the neutral axis to the surface strain-sensing station, x_i, in.
c_n	value of c_i at beam tip $(i = n)$, in.
c_0	value of c_i at beam root $(i = 0)$, in.
d	chord-wise distance between front and rear sensor lines for cantilever wing box, in.
deg	degree
E	Young modulus, lb/in^2
E_L	Young modulus of lamina in fiber direction, lb/in^2
E_T	Young modulus of lamina in direction transverse to fiber direction, lb/in^2

e	finite-element span-wise length, in.
G	shear modulus, lb/in^2
G_{LT}	shear modulus of lamina, lb/in^2
h	thickness of plate, in.
I	moment of inertia of tube cross section, in^4
i	$= 0, 1, 2, 3, \ldots .n$, strain-sensing station identification number
J	polar moment of inertia, in^4
j	index
l	length of cantilever tube, in.
M	moment, in-lb
M_i	moment at strain-sensing station, x_i, in-lb
n	number associated with the last span-wise strain-sensing station
P	applied load, lb
SPAR	Structural Performance And Resizing
T	twisting moment, in-lb
T_i	twisting moment at the distortion-sensing station, x_i, in-lb
t	thickness of 4-ply composite wall (or aluminum wall), in.
$\bar{t}$	thickness of 31-ply composite reinforced wall region, in.
V_i	local shear force at strain-sensing station, x_i, lb
w	width of wing box, in.
x, y	Cartesian coordinates, in.
y	deflection in y-direction at any point, x, between two strain-sensing stations, in.
x_i	i-th strain-sensing station, or its axial coordinate, $x=x_i$, in.
y_i	deflection in y-direction at strain-sensing station, x_i, in.
y_i^B	deflection of two-point supported beam at strain-sensing station, x_i, in.
y_i^s	shear-induced deflection, in.
y_i'	deflection in y-direction of the wing box rear sensing line at strain-sensing station, x_i, in.
γ_i	surface distortion angle (shear strain) at distortion strain-sensing station, x_i, rad
$\bar{\gamma}_i$	deflection shear strain at strain-sensing station, x_i, rad
Δl	$= l/n$, distance between two adjacent strain-sensing stations (equally spaced), in.
δ_1, δ_2	displacements at two ends of finite element, in.
ε	bending strain, in/in.
ε_i	bending strain at strain-sensing station, x_i, due to bending only, in/in.
ε_i'	bending strain of the wing box rear sensing line at strain-sensing station, x_i, due to bending only, in/in.

$\bar{\varepsilon}_i$	true bending strain at strain-sensing station, x_i, due to bending and torsion, in/in.
ε_i^P	principal tensile strain at distortion-sensing station, x_i, in the 45-deg helical direction, in/in.
θ	beam slope at any point, x, between two strain-sensing stations, $x_{i-1} \le x \le x_i$, rad or deg
θ_i	beam slope at strain-sensing station, x_i, rad or deg
ν_{LT}	Poisson's ratio of lamina
ν	Poisson's ratio
σ	bending stress of outermost fiber, lb/in^2
σ_i^p	principal tensile stress at distortion-sensing station, x_i, in the 45-deg helical direction, lb/in^2
τ_{max}	maximum shear stress at distortion-sensing station, x_i, lb/in^2
ϕ_i	cross-sectional twist angle at strain-sensing station, x_i, rad or deg
$(\ )_{i+}$	outboard side of strain-sensing station, x_i
$(\ )_{i-}$	inboard side of strain-sensing station, x_i

INTRODUCTION

The ultralightweight Helios flying wing (fig. 1; see Appendix A for details) has a wingspan of 247 ft. The Helios wingspan is longer than the wingspan of the U.S. Air Force C-5 military transport (Lockheed Martin Aeronautics Company, Marietta, Georgia), which is 222 ft, and that of the Boeing 747 commercial jetliner (Boeing Company, Seattle, Washington), which ranges from 195 to 215 ft depending on the model. The major load-carrying wing main spar is a carbon fiber composite tube (radius of 4 in.), which is thicker on the top and bottom (spar caps) to improve bending stiffness. The spar is wrapped with Nomex® and Kevlar® (both registered trademarks of E.I. duPont de Nemours and Company, Wilmington, Delaware) for additional strength.

Because of an excessively long wingspan and high flexibility, the Helios wing regularly experienced large deformations during flight, with the wingtip deflections reaching as high as 40 ft. This kind of deformed shape is similar to a 72-deg circular arc with a 197-ft radius.

The Helios wing recently experienced a midair breakup while flying at an altitude of approximately 3000 ft. The primary cause of the mishap is believed to have resulted from undamped pitch oscillations of the highly deformed wing.

To avoid future mishaps, a method must be developed in which the deformations of highly flexible structures can be visually monitored during flight. This way, if the wingtip deflections approach the design limit, the ground-based pilot could initiate an emergency maneuver to avoid further deformations.

This report discusses the formulation of displacement theories for uniform and tapered cantilever beams under bending, torsion, and combined bending and torsion. The formulated displacement equations are expressed in terms of strains at multiple strain sensors attached to the wing spar surface and can be used to calculate wing deflections and twist angles during flight. Next, the displacement theories for other structural configurations, such as two-point supported beams, wing boxes, and plates also are developed. Finally, the accuracy of the displacement theories is validated with finite-element analysis and classical beam theory using input-strains generated by finite-element analysis.

The displacement equations and onboard strain-sensing system could be a powerful tool for in-flight monitoring of wing deformations by the ground-based pilot for maintaining safe flights of the unmanned flying wings. In addition, the real-time wing shape could be input to the aircraft control system for aeroelastic wing shape control.

IN-FLIGHT DEFORMATION MONITORING

In-flight wing deformation monitoring of the Helios ultralightweight flying wing is particularly difficult because of weight restrictions and highly flexible nature of the aircraft. Several methods for in-flight monitoring of wing deflections exist for use on conventional aircraft.

One method is the electro-optical flight deflection measurement system, which is composed of onboard cameras and several wing-mounted targets (ref. 1). This system provides wing displacement information during the flight but is too heavy for lightweight flying wing applications.

Another in-flight deflection measurement method is the use of conventional strain gages to collect local strains for wing deflection information. Numerous strain-sensing stations are required to capture the higher displacement modes of the flexible wings. When multiple strain-sensing stations are used, the weight of the strain gage lead wires alone is too heavy and impractical for most weight conscious lightweight flying wing aircraft.

Fiber optic sensors offer the most attractive alternative to conventional strain gages. They are lightweight, fine, and flexible filaments (approximately the size of human hairs) and can be highly multiplexed at desired sensing intervals.

THEORETICAL APPROACH

If multiple strain sensors are installed at discrete sensing stations on a cantilever wing spar, strain sensor data can be used to calculate the deflections and twists of the wing spar during flight. Classical beam theory can be used to develop theoretical slope, deflection, and cross-sectional twist angle equations for uniform cantilever beams. These displacement equations are written in terms of strains for the calculations of the deformed shape of the beam. In the present report, the input strains are calculated from the displacement outputs of finite-element stress analysis. The accuracy of the newly developed displacement equations (for bending and torsion) is then verified by classical cantilever beam theory.

With slight modifications, the displacement equations developed for the uniform cantilever beam could be applied to predict the deformed shapes of two-point supported beams (simple beams) and plates. The displacement equations also can be modified to formulate the displacement equations for tapered, slightly tapered, and stepwise tapered cantilever beams, and for tapered cantilever wing boxes.

UNIFORM CANTILEVER BEAMS

Basic displacement equations are developed for a uniform cantilever beam (for example, the Helios wing tubular spar) subjected to bending, torsion, and combined bending and torsion. Although the highly flexible Helios wing can undergo large deformation (wingtip deflections of as much as 40 ft), the local strains on the wing spar surface remain small. Therefore, the classical small strain theory can be used to derive the slope and displacement equations for the uniform cantilever beam.

Bending

In this section, displacement equations for bending only are formulated. These equations describe the local slopes and deflections at points along the strain-sensing line on the bottom surface of a uniform cantilever beam of arbitrary cross-sectional shape (for example, a tubular Helios spar).

Moment-Strain Relationship

The classical beam differential equation (elastic curvature of the uniform beam) is given by (refs. 2, 3)

$$\frac{d^2y}{dx^2} = \frac{M(x)}{EI} \tag{1}$$

in which y is the vertical displacement, x is the span-wise coordinate, $M(x)$ is the bending moment, E is the Young modulus, and I is the moment of inertia. The bending moment, $M(x)$, in equation (1) may be related to the associated bending strain, $\varepsilon(x)$, at the bottom or top fiber (for example, a Helios tubular spar generatrix, which is a straight line on the tubular surface parallel to the longitudinal axis, x, of the tube) through the outermost fiber bending stress equation, $\sigma(x) = [M(x)c]/I$ (refs. 2, 3):

$$\varepsilon(x) = \frac{\sigma(x)}{E} = \frac{M(x)c}{EI} \quad ; \quad \sigma(x) = \frac{M(x)c}{I} \tag{2}$$

In equation (2), c is the beam half depth (for example, the outer radius of the Helios tubular spar). In light of equation (2), beam bending equation (1) can be written in terms of $\varepsilon(x)$ as

$$\frac{d^2 y}{dx^2} = \frac{\varepsilon(x)}{c} \tag{3}$$

Note that under the strain formulation, beam bending equation (3) contains only the beam geometrical parameter, half depth c, and that the flexural rigidity term EI is eliminated.

Consider the case of a highly flexible, extremely long Helios wing tubular spar that carries concentrated weight (solar powered motors, pods, hydrogen storage tanks, and so forth) at different wing stations. Because the wing is subjected to aerodynamic lift forces during flight, the wing spar bending moment, $M(x)$, could be a complicated nonlinear function of the span-wise coordinate, x.

Consider the uniform cantilever tubular spar with an outer radius, c, and length, l, as shown in figure 2. Let the surface bending strain sensors be installed at $n+1$ $(0, 1, 2, \ldots . n)$ number of equally spaced strain-sensing stations along the bottom or top generatrix of the spar (fig. 2). Although the bending strain is zero at the spar tip, the nth bending strain sensor is installed there because of mathematical convenience in the derivation of the spar tip slope and deflection equations.

The bending moment, $M(x)$, can be assumed to be a piecewise-linear function along the axial coordinate, x. Namely, in the region, $x_{i-1} < x < x_i$, between any two adjacent strain-sensing stations, $\{ x_{i-1}, x_i \}$, $M(x)$ is considered as a linear function of $(x - x_{i-1})$ as

$$M(x) = M_{i-1} - (M_{i-1} - M_i)\frac{x - x_{i-1}}{\Delta l} \quad ; \quad x_{i-1} < x < x_i \tag{4}$$

in which $\{M_{i-1}, M_i\}$ are the bending moments at the two adjacent strain-sensing stations, $\{x_{i-1}, x_i\}$, respectively, and $\Delta l \, (= x_i - x_{i-1} = l/n)$ is the axial distance between the two adjacent strain-sensing stations, $\{x_{i-1}, x_i\}$. In light of equation (2), the local moment equation (4) can be written in terms of the local bending strain, $\varepsilon(x)$, for the region, $x_{i-1} < x < x_i$, as

$$\varepsilon(x) = \varepsilon_{i-1} - (\varepsilon_{i-1} - \varepsilon_i)\frac{x - x_{i-1}}{\Delta l} \quad ; \quad x_{i-1} < x < x_i \quad ; \quad \Delta l = \frac{l}{n} \tag{5}$$

in which $\{ \varepsilon_{i-1}, \varepsilon_i \}$ are the bending strains measured at the two adjacent strain-sensing stations, $\{ x_{i-1}, x_i \}$, respectively.

Slope Equations

The slope, $\tan\theta(x)$, of the uniform beam in the region, $x_{i-1} \le x \le x_i$, between the two adjacent strain-sensing stations, $\{x_{i-1}, x_i\}$, can be obtained by integrating equation (3), with the constant of integration determined by enforcing the continuity of slope at the inboard adjacent strain-sensing station, x_{i-1}, as

$$\tan\theta(x) = \int_{x_{i-1}}^{x} \frac{d^2 y}{dx^2} dx + \underbrace{\tan\theta_{i-1}}_{\text{Slope at } x_{i-1}} = \int_{x_{i-1}}^{x} \frac{\varepsilon(x)}{c} dx + \tan\theta_{i-1} \quad ; \quad x_{i-1} \le x \le x_i \tag{6}$$

in which $\tan\theta_{i-1}$ (constant of integration) is the slope at the inboard adjacent strain-sensing station, x_{i-1}. By substituting strain equation (5) into slope equation (6) and carrying out the integration, one obtains the slope, $\tan\theta_i \equiv [\tan\theta(x_i)]$, at the strain-sensing station, x_i, as (see Appendix B for details of integration) (ref. 4)

$$\tan\theta_i = \frac{\Delta l}{2c}(\varepsilon_{i-1} + \varepsilon_i) + \tan\theta_{i-1} \quad ; \quad (i = 1, 2, 3, ..., n) \tag{7}$$

When $i = 1$, the slope, $\tan\theta_{1-1} = \tan\theta_0$, will be the slope at the left fixed end, which is zero $(\tan\theta_0 = 0)$ for the cantilever beam. If the reference left end is simply supported (as in the two-point supported beam case), then the slope, $\tan\theta_0$, is nonzero $(\tan\theta_0 \ne 0)$.

Writing out equation (7) for different strain-sensing stations, ($i = 1, 2, 3, ..., n$), results in

$$\tan\theta_1 = \frac{\Delta l}{2c}(\varepsilon_0 + \varepsilon_1) + \tan\theta_0 \quad ; \quad (\tan\theta_0 = 0 \text{ at built-in end}) \tag{8-a}$$

$$\tan\theta_2 = \frac{\Delta l}{2c}(\varepsilon_1 + \varepsilon_2) + \tan\theta_1 = \frac{\Delta l}{2c}(\varepsilon_0 + 2\varepsilon_1 + \varepsilon_2) \tag{8-b}$$

$$\tan\theta_3 = \frac{\Delta l}{2c}(\varepsilon_2 + \varepsilon_3) + \tan\theta_2 = \frac{\Delta l}{2c}\left[\varepsilon_0 + 2(\varepsilon_1 + \varepsilon_2) + \varepsilon_3\right] \tag{8-c}$$

$$\tan\theta_4 = \frac{\Delta l}{2c}(\varepsilon_3 + \varepsilon_4) + \tan\theta_3 = \frac{\Delta l}{2c}\left[\varepsilon_0 + 2(\varepsilon_1 + \varepsilon_2 + \varepsilon_3) + \varepsilon_4\right] \tag{8-d}$$

....

$$\tan\theta_n = \frac{\Delta l}{2c}(\varepsilon_{n-1} + \varepsilon_n) + \tan\theta_{n-1} = \frac{\Delta l}{2c}\left[\varepsilon_0 + 2(\varepsilon_1 + \varepsilon_2 + \varepsilon_3 + ... + \varepsilon_{n-1}) + \varepsilon_n\right]$$
$$= \frac{\Delta l}{2c}\left[\varepsilon_0 + 2\sum_{j=1}^{n-1}\varepsilon_j + \varepsilon_n\right] \tag{8-e}$$

The primary objective is to calculate $\tan\theta_i$ ($i = 1, 2, 3....., n$) for all strain-sensing stations. Because the last station, x_n, is located at the beam tip, the slope, $\tan\theta_n$, will give the beam tip slope.

Deflection Equations

The deflection, $y(x)$, of the uniform beam in the region, $x_{i-1} \le x \le x_i$, between the two adjacent strain-sensing stations, $\{x_{i-1}, x_i\}$, can be obtained by integrating slope equation (6) with the constant of integration determined by enforcing the continuity of deflection at the inboard adjacent strain-sensing station, x_{i-1}, as

$$y(x) = \underbrace{\int_{x_{i-1}}^{x} \tan\theta(x)dx}_{\text{Integration of slope}} + \underbrace{y_{i-1}}_{\substack{\text{Deflection} \\ \text{at } x_{i-1}}} = \underbrace{\int_{x_{i-1}}^{x} \int_{x_{i-1}}^{x} \frac{\varepsilon(x)}{c}dxdx}_{\text{Deflection increment}} + \underbrace{\int_{x_{i-1}}^{x} \tan\theta_{i-1}dx}_{\substack{\text{Deflection at } x \\ \text{due to } \tan\theta_{i-1}}} + \underbrace{y_{i-1}}_{\substack{\text{Deflection} \\ \text{at } x_{i-1}}} \quad ; \quad x_{i-1} \le x \le x_i \tag{9}$$

in which y_{i-1} (integration constant) is the deflection at the inboard adjacent strain-sensing station, x_{i-1}. Carrying out the integration of equation (9) in light of strain equation (5), the deflection, $y_i \equiv [y(x_i)]$, at the strain-sensing station, x_i, is obtained as (see Appendix B for details of integration) (ref. 4)

$$y_i = \frac{(\Delta l)^2}{6c}\left(2\varepsilon_{i-1} + \varepsilon_i\right) + y_{i-1} + \Delta l \tan\theta_{i-1} \quad ; \quad (i = 1, 2, 3, ..., n) \tag{10}$$

When $i = 1$, $y_0 = \tan\theta_0 = 0$ at the fixed end. Writing out deflection equation (10) for different strain-sensing stations (i=1, 2, 3, ..., n), one obtains

$$y_1 = \frac{(\Delta l)^2}{6c}\left(2\varepsilon_0 + \varepsilon_1\right) + y_0 + \Delta l \tan\theta_0 = \frac{(\Delta l)^2}{6c}\left(2\varepsilon_0 + \varepsilon_1\right) \quad ; \quad y_0 = \tan\theta_0 = 0 \text{ at built-in end} \tag{10-a}$$

$$y_2 = \frac{(\Delta l)^2}{6c}\left(2\varepsilon_1 + \varepsilon_2\right) + y_1 + \Delta l \tan\theta_1 = \frac{(\Delta l)^2}{6c}\left(2\varepsilon_0 + 3\varepsilon_1 + \varepsilon_2\right) + \Delta l \tan\theta_1 \tag{10-b}$$

$$y_3 = \frac{(\Delta l)^2}{6c}\left(2\varepsilon_2 + \varepsilon_3\right) + y_2 + \Delta l \tan\theta_2 = \frac{(\Delta l)^2}{6c}\left[2\varepsilon_0 + 3\left(\varepsilon_1 + \varepsilon_2\right) + \varepsilon_3\right] + \Delta l\left(\tan\theta_1 + \tan\theta_2\right) \tag{10-c}$$

$$y_4 = \frac{(\Delta l)^2}{6c}\left(2\varepsilon_3 + \varepsilon_4\right) + y_3 + \Delta l \tan\theta_3 = \frac{(\Delta l)^2}{6c}\left[2\varepsilon_0 + 3\left(\varepsilon_1 + \varepsilon_2 + \varepsilon_3\right) + \varepsilon_4\right]$$
$$+ \Delta l\left(\tan\theta_1 + \tan\theta_2 + \tan\theta_3\right) \tag{10-d}$$

....

$$y_n = \frac{(\Delta l)^2}{6c}\left[2\varepsilon_0 + 3\left(\varepsilon_1 + \varepsilon_2 + \varepsilon_3 + ... + \varepsilon_{n-1}\right) + \varepsilon_n\right] + \Delta l\left(\tan\theta_1 + \tan\theta_2 + \tan\theta_3 + ... + \tan\theta_{n-1}\right)$$
$$= \frac{(\Delta l)^2}{6c}\left[2\varepsilon_0 + 3\sum_{i=1}^{n-1}\varepsilon_i + \varepsilon_n\right] + \Delta l\sum_{i=1}^{n-1}\tan\theta_i \tag{10-e}$$

8

In light of slope equation (8), the summation of $\tan\theta_i$ of the last term in equation (10-e) can be written out in terms of strains, ε_i, as

$$\sum_{i=1}^{n-1}\tan\theta_i = \frac{\Delta l}{2c}\left\{(n-1)\varepsilon_o + [2(n-1)-1]\varepsilon_1 + [2(n-2)-1]\varepsilon_2 + [2(n-3)-1]\varepsilon_3 + ... + \varepsilon_{n-1}\right\}$$
$$= \frac{\Delta l}{2c}\left\{(n-1)\varepsilon_o + \sum_{i=1}^{n-1}[2(n-i)-1]\varepsilon_i\right\} \tag{11}$$

In light of equation (11), bending deflection equation (10) takes on the following form, expressed exclusively in terms of the bending strains, ε_i:

$$y_1 = \frac{(\Delta l)^2}{6c}(2\varepsilon_0 + \varepsilon_1) \quad ; \quad (y_0 = \tan\theta_0 = 0 \text{ at the built-in end}) \tag{12-a}$$

$$y_2 = \frac{(\Delta l)^2}{6c}(5\varepsilon_0 + 6\varepsilon_1 + \varepsilon_2) \tag{12-b}$$

$$y_3 = \frac{(\Delta l)^2}{6c}\left[8\varepsilon_0 + 6(2\varepsilon_1 + \varepsilon_2) + \varepsilon_3\right] \tag{12-c}$$

$$y_4 = \frac{(\Delta l)^2}{6c}\left[11\varepsilon_0 + 6(3\varepsilon_1 + 2\varepsilon_2 + \varepsilon_3) + \varepsilon_4\right] \tag{12-d}$$

$$................................$$

$$y_n = \frac{(\Delta l)^2}{6c}\left\{(3n-1)\varepsilon_0 + 6\left[(n-1)\varepsilon_1 + (n-2)\varepsilon_2 + (n-3)\varepsilon_3 + ... + [n-(n-1)]\varepsilon_{n-1}\right] + \varepsilon_n\right\}$$
$$= \frac{(\Delta l)^2}{6c}\left[(3n-1)\varepsilon_0 + 6\sum_{i=1}^{n-1}(n-i)\varepsilon_i + \varepsilon_n\right] \tag{12-e}$$

The deformed shape of the tubular wing spar can be constructed by plotting each deflection, y_i ($i = 1, 2, 3...., n$), at each strain-sensing station, x_i. The shape could then be displayed on the screen so that the ground-based pilot can view the real-time wing deformation status.

The contribution of deflection caused by transverse shear effect usually is very small for a long cantilever beam. If the transverse shear effect is desired, however, an additional transverse shear effect term must be added to equation (12) as shown in Appendix C.

9

Torsion

In this section, displacement equations are developed for a cantilever tubular beam under torsion. The local beam cross-sectional twist angle is written in terms of surface distortion angle at the inboard distortion-sensing stations.

Torque-Twist Relationship

Consider a cantilever tubular spar, with a length of l and $n+1$ (0, 1, 2, ... n) number of equally spaced distortion strain-sensing stations (fig. 3), subjected to varying span-wise twisting moments in addition to bending (fig. 2). Let T_i be the twisting moment at the distortion-sensing station, x_i, and let γ_i be the associated local surface distortion angle (shear strain) at station x_i (fig. 3). The torque-distortion relationship can then be written as (refs.1, 2)

$$\gamma_i = \frac{T_i c}{GJ} \tag{13}$$

in which G is the shear modulus, J is the polar moment of inertia, and c is the outer radius of the wing spar. The surface distortion angle, γ_i (shear strain), in equation (13) is obtained from the distortion sensors as

$$\gamma_i = \frac{(\tau_{max})_i}{G} = \frac{\sigma_i^p}{G} = \frac{E}{G}\varepsilon_i^p = 2(1+v)\varepsilon_i^p \tag{14}$$

in which $(\tau_{max})_i$ is the maximum shear stress at the distortion-sensing station, x_i, and σ_i^p $(=(\tau_{max})_i)$ and ε_i^P are the principal tensile stress and strain, respectively, in the 45-deg helical direction at the distortion-sensing station, x_i (fig. 3).

Cross-Sectional Twists

In light of figure 3, the total cross-sectional twist angle, ϕ_i, at the strain-sensing station, x_i, can be obtained by summing up the partial cross-sectional twist angles, $\frac{\Delta l}{c}\gamma_j$, at all the inboard sensing stations, j (= 1, 2, 3....., i–1), as (fig. 3)

$$\phi_1 = \frac{\Delta l}{c}\gamma_0 \tag{15-a}$$

$$\phi_2 = \frac{\Delta l}{c}(\gamma_0 + \gamma_1) \tag{15-b}$$

$$\phi_3 = \frac{\Delta l}{c}(\gamma_0 + \gamma_1 + \gamma_2) \tag{15-c}$$

$$\phi_4 = \frac{\Delta l}{c}(\gamma_0 + \gamma_1 + \gamma_2 + \gamma_3) \qquad (15\text{-}d)$$

$$\dotsb\dotsb\dotsb\dotsb$$

$$\phi_n = \frac{\Delta l}{c}(\gamma_0 + \gamma_1 + \gamma_2 + \gamma_3 + \gamma_4 + ... + \gamma_{n-1}) \qquad (15\text{-}e)$$

Notice that in the expression of the tip cross-sectional twist angle, ϕ_n (eq. (15-e)), the tip distortion term, γ_n, does not appear. Therefore, installation of the tip distortion sensor for γ_n is not required (fig. 3).

Equation (15) can be applied to a rectangular cantilever beam (for example, a wing box) if c represents the half width of the wing box. For the wing box, the surface distortion sensors can be installed on the vertical or horizontal surface. A simpler way to obtain the cross-sectional twist angle for the wing box, however, is to use two parallel bending strain-sensing lines without the need to install the distortion sensors (see the section entitled "Other Applications: Wing Boxes").

Combined Bending and Torsion

In this section, displacement equations are developed for a tubular cantilever spar under combined bending and torsion. The calculations of true bending strains are presented, from which modified slope and modified deflection equations are established.

True Bending Strain

As shown in figure 3, if the tubular spar is subjected to both bending and torsion, the bending strain-sensing station, x_i (for measuring the bending strain, ε_i), will move tangentially by a cross-sectional twist angle, ϕ_i, and the bending strain-sensing axis will be tilted by a local surface distortion angle, γ_i. Thus, the strain output, ε_i, obtained at the strain-sensing station, x_i, no longer gives the true bending strain. To obtain the true bending strain, $\bar{\varepsilon}_i$, the value of the measured strain, ε_i, must be corrected by using the bending strain correction equation

$$\bar{\varepsilon}_i = \frac{\varepsilon_i}{\cos\phi_i \cos\gamma_i} \qquad (16)$$

in which the surface distortion angle, γ_i, and the cross-sectional twist angle, ϕ_i, are calculated from equations (14) and (15), respectively. With the effect of torsion, slope equation (8) and deflection equation (12) for the bending must be modified by replacing ε_i with $\bar{\varepsilon}_i$.

11

Modified Slope Equation

By replacing the bending strain, ε_i, in slope equation (8) with the true bending strain, $\bar{\varepsilon}_i$, one obtains the following modified slope equation:

$$\tan\theta_1 = \frac{\Delta l}{2c}(\bar{\varepsilon}_0 + \bar{\varepsilon}_1) \tag{17-a}$$

$$\tan\theta_2 = \frac{\Delta l}{2c}(\bar{\varepsilon}_1 + \bar{\varepsilon}_2) + \tan\theta_1 = \frac{\Delta l}{2c}(\bar{\varepsilon}_0 + 2\bar{\varepsilon}_1 + \bar{\varepsilon}_2) \tag{17-b}$$

$$\tan\theta_3 = \frac{\Delta l}{2c}(\bar{\varepsilon}_2 + \bar{\varepsilon}_3) + \tan\theta_2 = \frac{\Delta l}{2c}\left[\bar{\varepsilon}_0 + 2(\bar{\varepsilon}_1 + \bar{\varepsilon}_2) + \bar{\varepsilon}_3\right] \tag{17-c}$$

$$\tan\theta_4 = \frac{\Delta l}{2c}(\bar{\varepsilon}_3 + \bar{\varepsilon}_4) + \tan\theta_3 = \frac{\Delta l}{2c}\left[\bar{\varepsilon}_0 + 2(\bar{\varepsilon}_1 + \bar{\varepsilon}_2 + \bar{\varepsilon}_3) + \bar{\varepsilon}_4\right] \tag{17-d}$$

....

$$\tan\theta_n = \frac{\Delta l}{2c}(\bar{\varepsilon}_{n-1} + \bar{\varepsilon}_n) + \tan\theta_{n-1} = \frac{\Delta l}{2c}\left[\bar{\varepsilon}_0 + 2(\bar{\varepsilon}_1 + \bar{\varepsilon}_2 + \bar{\varepsilon}_3 + ... + \bar{\varepsilon}_{n-1}) + \bar{\varepsilon}_n\right]$$

$$= \frac{\Delta l}{2c}\left[\bar{\varepsilon}_0 + 2\sum_{i=1}^{n-1}\bar{\varepsilon}_i + \bar{\varepsilon}_n\right] \tag{17-e}$$

Modified Deflection Equation

By replacing the bending strain, ε_i, in deflection equation (12) with the true bending strain, $\bar{\varepsilon}_i$, one obtains the following modified deflection equation:

$$y_1 = \frac{(\Delta l)^2}{6c}\left(2\bar{\varepsilon}_0 + \bar{\varepsilon}_1\right) \tag{18-a}$$

$$y_2 = \frac{(\Delta l)^2}{6c}\left(5\bar{\varepsilon}_0 + 6\bar{\varepsilon}_1 + \bar{\varepsilon}_2\right) \tag{18-b}$$

$$y_3 = \frac{(\Delta l)^2}{6c}\left[8\bar{\varepsilon}_0 + 6(2\bar{\varepsilon}_1 + \bar{\varepsilon}_2) + \bar{\varepsilon}_3\right] \tag{18-c}$$

$$y_4 = \frac{(\Delta l)^2}{6c}\left[11\bar{\varepsilon}_0 + 6\left(3\bar{\varepsilon}_1 + 2\bar{\varepsilon}_2 + \bar{\varepsilon}_3\right) + \bar{\varepsilon}_4\right] \tag{18-d}$$

....

$$y_n = \frac{(\Delta l)^2}{6c}\left\{(3n-1)\bar{\varepsilon}_0 + 6\left[(n-1)\bar{\varepsilon}_1 + (n-2)\bar{\varepsilon}_2 + (n-3)\bar{\varepsilon}_3 + \ldots + [n-(n-1)]\bar{\varepsilon}_{n-1}\right] + \bar{\varepsilon}_n\right\}$$

$$= \frac{(\Delta l)^2}{6c}\left[(3n-1)\bar{\varepsilon}_0 + 6\sum_{i=1}^{n-1}(n-i)\bar{\varepsilon}_i + \bar{\varepsilon}_n\right] \tag{18-e}$$

When the true bending strain data $\{\bar{\varepsilon}_0, \bar{\varepsilon}_1, \bar{\varepsilon}_2, \bar{\varepsilon}_3, \bar{\varepsilon}_4, \ldots, \bar{\varepsilon}_n\}$ are substituted, the slopes and deflections of the tubular spar at the strain-sensing stations can be calculated from equations (17) and (18), respectively, for the combined bending and torsion loading case.

TAPERED CANTILEVER BEAMS

For a cantilever beam with a depth that tapers down arbitrarily from the beam root to the beam tip (for example, a conventional aircraft wing), the half beam depth, $c(x)$, is no longer constant along the span. Assuming that $c(x)$ varies linearly in the region $x_{i-1} < x < x_i$ between the two adjacent strain-sensing stations, $\{x_{i-1}, x_i\}$, $c(x)$ can be expressed as

$$c(x) = c_{i-1} - (c_{i-1} - c_i)\frac{x - x_{i-1}}{\Delta l} \quad ; \quad x_{i-1} < x < x_i \tag{19}$$

in which $\{c_{i-1}, c_i\}$ are the values of $c(x)$ at the strain-sensing stations, $\{x_{i-1}, x_i\}$, respectively. If the beam depth tapers down linearly from the beam root to the beam tip, then $\{c_{i-1}, c_i\}$ can be expressed as

$$c_{i-1} = c_0 - (c_0 - c_n)\frac{(i-1)\Delta l}{l} = c_0 - (c_0 - c_n)\frac{(i-1)}{n} \quad ; \quad l = n\Delta l \tag{20}$$

$$c_i = c_0 - (c_0 - c_n)\frac{i(\Delta l)}{l} = c_0 - (c_0 - c_n)\frac{i}{n} \quad ; \quad l = n\Delta l \tag{21}$$

in which $\{c_0, c_n\}$ are the values of $c(x)$ at the beam root and beam tip, respectively.

Slope Equations

The slope, $\tan\theta(x)$, of the tapered beam in the region, $x_{i-1} \le x \le x_i$, between the two adjacent strain-sensing stations, $\{x_{i-1}, x_i\}$, can be obtained by integrating equation (3) (c is replaced with

13

$c(x)$), with constant of integration determined by enforcing the continuity of slope at the inboard adjacent strain-sensing station, x_{i-1} , as

$$\tan\theta(x) = \underbrace{\int_{x_{i-1}}^{x} \frac{d^2y}{dx^2} dx}_{\text{Slope increment}} + \underbrace{\tan\theta_{i-1}}_{\text{Slope at } x_{i-1}} = \int_{x_{i-1}}^{x} \frac{\varepsilon(x)}{c(x)} dx + \tan\theta_{i-1} \quad ; \quad x_{i-1} \le x \le x_i \tag{22}$$

By substituting strain equation (5) and half-depth equation (19) into slope equation (22), and carrying out the integration, one obtains the slope, $\tan\theta_i \equiv [\tan\theta(x_i)]$, at the strain-sensing station, x_i , as (see Appendix D for details of integration) (ref. 4)

$$\tan\theta_i = \Delta l \left[\frac{\varepsilon_{i-1} - \varepsilon_i}{c_{i-1} - c_i} + \frac{\varepsilon_{i-1}c_i - \varepsilon_i c_{i-1}}{(c_{i-1} - c_i)^2} \log\frac{c_i}{c_{i-1}} \right] + \tan\theta_{i-1} \quad ; \quad (i = 1, 2, 3, ..., n) \tag{23}$$

Deflection Equations

The deflection, $y(x)$, of the tapered beam in the region, $x_{i-1} \le x \le x_i$, between the two adjacent strain-sensing stations, $\{x_{i-1}, x_i\}$, can be obtained by integrating slope equation (22), with the constant of integration determined by enforcing the continuity of deflection at the inboard adjacent strain-sensing station, x_{i-1} , as

$$y(x) = \underbrace{\int_{x_{i-1}}^{x} \tan\theta(x)dx}_{\text{Integration of slope}} + \underbrace{y_{i-1}}_{\substack{\text{Deflection} \\ \text{at } x_{i-1}}} = \underbrace{\int_{x_{i-1}}^{x} \int_{x_{i-1}}^{x} \frac{\varepsilon(x)}{c(c)} dxdx}_{\text{Deflection increment}} + \underbrace{\int_{x_{i-1}}^{x} \tan\theta_{i-1}dx}_{\substack{\text{Deflection at } x \\ \text{due to } \tan\theta_{i-1}}} + \underbrace{y_{i-1}}_{\substack{\text{Deflection} \\ \text{at } x_{i-1}}} \quad ; \quad x_{i-1} \le x \le x_i \tag{24}$$

By substituting strain equation (5) and half-depth equation (19) into deflection equation (24), and carrying out the integration, one obtains the deflection, $y_i \equiv [y(x_i)]$, at the strain-sensing station, x_i , as (see Appendix D for details of integration) (ref. 4)

$$y_i = (\Delta l)^2 \left[\frac{\varepsilon_{i-1} - \varepsilon_i}{2(c_{i-1} - c_i)} - \frac{\varepsilon_{i-1}c_i - \varepsilon_i c_{i-1}}{(c_{i-1} - c_i)^3} \left(c_i \log\frac{c_i}{c_{i-1}} + (c_{i-1} - c_i) \right) \right] + y_{i-1} + \Delta l \tan\theta_{i-1} \tag{25}$$

$$(i = 1, 2, 3, ..., n); y_0 = \tan\theta_0 = 0$$

SLIGHTLY TAPERED CANTILEVER BEAMS

For a slightly tapered cantilever beam, the perturbation and stepwise methods can be used to develop the slope and deflection equations. This section discusses these two methods.

14

Perturbation Method

When the cantilever beam is slightly tapered (that is, $(c_i/c_{i-1}) \to 1$), the logarithmic terms in slope equation (23) and deflection equation (25) will approach zero [that is, $\log(c_i/c_{i-1}) \to 0$]. Therefore, the perturbation method must be used to expand the logarithmic term, $\log(c_i/c_{i-1})$, in the neighborhood of $(c_i/c_{i-1}) \approx 1$ and then obtain nonzero mathematical expressions so that the slope and deflection equations could degenerate into those for the uniform cantilever beam case, $(c_i/c_{i-1}) = 1$.

Slope Equations

For a slightly tapered beam, the logarithm term, $\log(c_i/c_{i-1}) \to 1$, in slope equation (23) can be expanded in the neighborhood of $(c_i/c_{i-1}) \approx 1$ [that is, $\log(c_i/c_{i-1}) \approx 0$]. Carrying out the expansion up to the second order terms in $(c_{i-1} - c_i)^2$, the logarithm term, $\log(c_i/c_{i-1})$, takes on the following form as c_i approaches $c_{i-1} \left[(c_i/c_{i-1}) \to 1\right]$ (see Appendix E for details of mathematical expansions) (ref. 4):

$$\log \frac{c_i}{c_{i-1}} \approx \frac{c_{i-1} - c_i}{2c_{i-1}^2}(c_i - 3c_{i-1}) \quad ; \quad \frac{c_i}{c_{i-1}} \to 1 \tag{26}$$

In light of equation (26), slope equation (23) becomes the following form for the slightly tapered beam:

$$\tan \theta_i = \frac{\Delta l}{2c_{i-1}}\left[\left(2 - \frac{c_i}{c_{i-1}}\right)\varepsilon_{i-1} + \varepsilon_i\right] + \tan \theta_{i-1} \quad ; \quad \frac{c_i}{c_{i-1}} \to 1 \tag{27}$$

When the tapering diminishes (that is, $c_i = c_{i-1} = c$), equation (27) degenerates into the slope equation for the uniform cantilever beams as

$$\tan \theta_i = \frac{\Delta l}{2c}(\varepsilon_{i-1} + \varepsilon_i) + \tan \theta_{i-1} \quad ; \quad c_i = c_{i-1} = c \tag{28}$$

which is exactly the same as slope equation (7) for the uniform beam.

Deflection Equations

When the beam becomes slightly tapered (that is, $c_i \to c_{i-1}$, the term, $\left[c_i \log(c_i/c_{i-1}) + (c_{i-1} - c_i)\right]$, in equation (25) can be expanded in the vicinity of $(c_i / c_{i-1}) \approx 1$ (that is, $\log(c_i/c_{i-1}) \approx 0$). Carrying out the expansion up to the third order terms of $(c_{i-1} - c_i)^3$, the term, $\left[c_i \log(c_i/c_{i-1}) + (c_{i-1} - c_i)\right]$, takes on the following form as c_i approaches $c_{i-1}\left[(c_i/c_{i-1}) \to 1\right]$ (see Appendix E for details of mathematical expansions) (ref. 4):

$$\left[c_i \log(\frac{c_i}{c_{i-1}}) + (c_{i-1} - c_i) \right] \approx \frac{(c_{i-1} - c_i)^2}{6c_{i-1}} \left[3 + \frac{(c_{i-1} - c_i)}{c_{i-1}} \right] \quad ; \quad \frac{c_i}{c_{i-1}} \to 1 \tag{29}$$

In light of equation (29), deflection equation (25) becomes the following form for the slightly tapered cantilever beam:

$$y_i = \frac{(\Delta l)^2}{6c_{i-1}} \left[\left(3 - \frac{c_i}{c_{i-1}} \right) \varepsilon_{i-1} + \varepsilon_i \right] + y_{i-1} + \Delta l \tan \theta_{i-1} \quad ; \quad \frac{c_i}{c_{i-1}} \to 1 \tag{30}$$

When the beam taper diminishes (that is, $c_i = c_{i-1} = c$), equation (30) degenerates into the deflection equation for the uniform cantilever beam as

$$y_i = \frac{(\Delta l)^2}{6c} (2\varepsilon_{i-1} + \varepsilon_i) + y_{i-1} + \Delta l \tan \theta_{i-1} \quad ; \quad c_i = c_{i-1} = c \tag{31}$$

which is identical to the last expression of deflection equation (10) for the uniform cantilever beam.

Stepwise Method

The slightly tapered cantilever beam can also be approximated with a stepwise tapered cantilever beam. The beam segment between the two adjacent strain-sensing stations, { x_{i-1}, x_i }, can be considered as a uniform beam segment with an average constant semi-depth of $c = (1/2)(c_{i-1} + c_i)$. Slope equation (8) and displacement equation (12) can be modified for the stepwise tapered cantilever beam as follows.

Slope Equation

The slope equation of the stepwise tapered cantilever beam can be written as

$$\tan \theta_1 = \Delta l \left[\frac{\varepsilon_0 + \varepsilon_1}{c_0 + c_1} \right] + \tan \theta_0 \quad ; \quad \tan \theta_0 = 0 \tag{32-a}$$

$$\tan \theta_2 = \Delta l \left[\frac{\varepsilon_1 + \varepsilon_2}{c_1 + c_2} \right] + \tan \theta_1 = \Delta l \left[\frac{\varepsilon_1 + \varepsilon_2}{c_1 + c_2} + \frac{\varepsilon_0 + \varepsilon_1}{c_0 + c_1} \right] + \tan \theta_0 \tag{32-b}$$

$$\tan \theta_3 = \Delta l \left[\frac{\varepsilon_2 + \varepsilon_3}{c_2 + c_3} \right] + \tan \theta_2 = \Delta l \left[\frac{\varepsilon_2 + \varepsilon_3}{c_2 + c_3} + \frac{\varepsilon_1 + \varepsilon_2}{c_1 + c_2} + \frac{\varepsilon_0 + \varepsilon_1}{c_0 + c_1} \right] + \tan \theta_0 \tag{32-c}$$

$$\tan\theta_4 = \Delta l\left[\frac{\varepsilon_3+\varepsilon_4}{c_3+c_4}\right]+\tan\theta_3 = \Delta l\left[\frac{\varepsilon_3+\varepsilon_4}{c_3+c_4}+\frac{\varepsilon_2+\varepsilon_3}{c_2+c_3}+\frac{\varepsilon_1+\varepsilon_2}{c_1+c_2}+\frac{\varepsilon_0+\varepsilon_1}{c_0+c_1}\right]+\tan\theta_0 \tag{32-d}$$

....

$$\tan\theta_n = \Delta l\left[\frac{\varepsilon_{n-1}+\varepsilon_n}{c_{n-1}+c_n}\right]+\tan\theta_{n-1} = \Delta l\sum_{i=1}^{n}\left[\frac{\varepsilon_{i-1}+\varepsilon_i}{c_{i-1}+c_i}\right]+\tan\theta_0 \tag{32-e}$$

Deflection Equations

The deflection equation of the stepwise tapered cantilever beam can be written as

$$y_1 = \frac{\Delta l^2}{3(c_0+c_1)}\left(2\varepsilon_0+\varepsilon_1\right)+y_0+\Delta l\tan\theta_0 = \frac{\Delta l^2}{3}\left[\frac{2\varepsilon_0+\varepsilon_1}{c_0+c_1}\right] \quad ; \quad y_0=0,\ \tan\theta_0=0 \tag{33-a}$$

$$y_2 = \frac{\Delta l^2}{3(c_1+c_2)}\left(2\varepsilon_1+\varepsilon_2\right)+y_1+\Delta l\tan\theta_1 = \frac{\Delta l^2}{3}\left[\frac{2\varepsilon_1+\varepsilon_2}{c_1+c_2}+\frac{2\varepsilon_0+\varepsilon_1}{c_0+c_1}\right]+\Delta l\tan\theta_1 \tag{33-b}$$

$$y_3 = \frac{\Delta l^2}{3(c_2+c_3)}\left(2\varepsilon_2+\varepsilon_3\right)+y_2+\Delta l\tan\theta_2 = \frac{\Delta l^2}{3}\left[\frac{2\varepsilon_2+\varepsilon_3}{c_2+c_3}+\frac{2\varepsilon_1+\varepsilon_2}{c_1+c_2}\right]$$
$$+\Delta l\left(\tan\theta_1+\tan\theta_2\right) \tag{33-c}$$

$$y_4 = \frac{\Delta l^2}{3(c_3+c_4)}\left(2\varepsilon_3+\varepsilon_4\right)+y_3+\Delta l\tan\theta_3 = \frac{\Delta l^2}{3}\left[\frac{2\varepsilon_3+\varepsilon_4}{c_3+c_4}+\frac{2\varepsilon_2+\varepsilon_3}{c_2+c_3}\right]$$
$$+\Delta l\left(\tan\theta_1+\tan\theta_2+\tan\theta_3\right) \tag{33-d}$$

....

$$y_n = \frac{\Delta l^2}{3(c_{n-1}+c_n)}\left(2\varepsilon_{n-1}+\varepsilon_n\right)+y_{n-1}+\Delta l\tan\theta_{n-1} = \frac{\Delta l^2}{3}\left[\frac{2\varepsilon_{n-1}+\varepsilon_n}{c_{n-1}+c_n}+\frac{2\varepsilon_{n-2}+\varepsilon_{n-1}}{c_{n-2}+c_{n-1}}\right]$$
$$+\Delta l\sum_{i=1}^{n-1}\tan\theta_i \tag{33-e}$$

The last term in equation (33-e) can be expressed as

$$\sum_{i=1}^{n-1} \tan\theta_i = \Delta l \left\{ (n-1)\frac{\varepsilon_0 + \varepsilon_1}{c_0 + c_1} + (n-2)\frac{\varepsilon_1 + \varepsilon_2}{c_1 + c_2} + (n-3)\frac{\varepsilon_2 + \varepsilon_3}{c_2 + c_3} + \dots + [n-(n-1)]\frac{\varepsilon_{n-2} + \varepsilon_{n-1}}{c_{n-2} + c_{n-1}} \right\}$$

$$= \Delta l \sum_{i=1}^{n-1} \left[(n-i)\frac{\varepsilon_{i-1} + \varepsilon_i}{c_{i-1} + c_i} \right] \tag{34}$$

In light of equation (34), deflection equation (33-e) becomes

$$y_n = \frac{(\Delta l)^2}{3} \left[\frac{2\varepsilon_{n-1} + \varepsilon_n}{c_{n-1} + c_n} + \frac{2\varepsilon_{n-2} + \varepsilon_{n-1}}{c_{n-2} + c_{n-1}} \right] + (\Delta l)^2 \sum_{i=1}^{n-1} \left[(n-i)\frac{\varepsilon_{i-1} + \varepsilon_i}{c_{i-1} + c_i} \right] \tag{35}$$

Note that equation (35) is for the last span-wise strain-sensing station, n. It can, however, be used to calculate the deflection at any strain-sensing station, x_i ($= 1,2,3,\dots, n$), by simply replacing the indices, $\{n, i\}$, with $\{i, j\}$.

OTHER APPLICATIONS

The bending deflection equations developed for the uniform and tapered cantilever beams in the previous sections can also be applied to predict the deformed shapes of other types of structures. This section discusses the application of these equations to cantilever wing boxes, two-point supported beams (simple beams), and plates.

Wing Boxes

Figure 4 shows a wing box, which is a type of a tapered cantilever beam. The simple way to monitor the wing box deformation under combined bending and torsion is to use two parallel bending strain-sensing lines in the span-wise direction (fig. 4). If $\{y_i, y_i'\}$ denote the deflections of the front and rear sensors, respectively, at the same span-wise strain-sensing cross section, x_i ($i = 1, 2, 3, \dots n$), and if d is the chord-wise distance between the front and rear sensor lines, then the cross-sectional twist angle, ϕ_i, at any strain-sensing cross section, x_i (fig. 4), can be calculated from the following equation:

$$\phi_i = \sin^{-1}\left(\frac{y_i - y_i'}{d} \right) \tag{36}$$

In equation (36), $\{y_i, y_i'\}$ can be calculated from deflection equation (25) (or eq. (30) or (35)) for a tapered cantilever beam by using the strain data obtained from the two-line sensing system as inputs. With equation (36) on hand, the distortion sensor is not required.

18

Two-Point Supported Beams

Deflection equation (12) was developed for a uniform cantilever beam with a clamped left end (that is, zero slope and zero deflection, $y_n = \tan\theta_0 = 0$) and a finite deflection (y_n) at the beam tip. If the strains, $y_n = 0$, of the two-point supported beam with a clamped left end are used as inputs, then equation (12) theoretically should give zero deflection ($y_n = 0$) at the right end. If the calculated right end deflection is not zero, however, and it has a small value because of possible measurement errors, then equation (12) must be corrected.

To eliminate the nonzero ($y_n \neq 0$) right end deflection, the deflection curve is rotated slightly as a whole, with respect to the left end support point, in such a way as to bring the tip deflection, y_n (eq. (12-e)), down to zero ($y_n = 0$). Therefore, the deflection calculated from equation (12) for each strain-sensing station, x_i, is reduced by an amount of $(i/n)y_n$ (i = 1, 2, 3 ….. n), a linearly varying fraction of the nonzero right end cantilever tip deflection, y_n.

If y_i^B denotes the deflection of the two-point supported beam at the strain-sensing station, x_i, then the deflection equation for the two-point supported beam can be established from cantilever deflection equation (12) with corrections as follows:

$$y_1^B = y_1 - \frac{1}{n}y_n$$
$$= \frac{(\Delta l)^2}{6c}\left(2\varepsilon_0 + \varepsilon_1\right) - \frac{1}{n}y_n \qquad (37\text{-a})$$

$$y_2^B = y_2 - \frac{2}{n}y_n$$
$$= \frac{(\Delta l)^2}{6c}\left(5\varepsilon_0 + 6\varepsilon_1 + \varepsilon_2\right) - \frac{2}{n}y_n \qquad (37\text{-b})$$

$$y_3^B = y_3 - \frac{3}{n}y_n$$
$$= \frac{(\Delta l)^2}{6c}\left[8\varepsilon_0 + 6\left(2\varepsilon_1 + \varepsilon_2\right) + \varepsilon_3\right] - \frac{3}{n}y_n \qquad (37\text{-c})$$

$$y_4^B = y_4 - \frac{4}{n}y_n$$
$$= \frac{(\Delta l)^2}{6c}\left[11\varepsilon_0 + 6\left(3\varepsilon_1 + 2\varepsilon_2 + \varepsilon_3\right) + \varepsilon_4\right] - \frac{4}{n}y_n \qquad (37\text{-d})$$

……………………………

19

$$y_n^B = y_n - \frac{n}{n} y_n$$

$$= \frac{(\Delta l)^2}{6c} \left[(3n-1)\varepsilon_0 + 6\sum_{i=1}^{n-1}(n-i)\varepsilon_i + \varepsilon_n \right] - \frac{n}{n} y_n = 0 \qquad \text{(37-e)}$$

In equation (37), y_i ($i = 1, 2, 3 \ldots\ldots n$) represents the deflections calculated from cantilever beam deflection equation (12).

If the two-point supported beam is symmetrically loaded, the distribution of the strain, ε_i, will be symmetrical with respect to the point of symmetry, and the mathematical expressions of the deflections obtained from equation (37) can be proven to be identical for the two mirror image sensing stations. Deflection equation (37) established for the two-point supported beam can also be used to predict the deformed shapes of plates.

Beam With Two Ends Clamped

For the beam with two ends clamped, the support conditions for the two ends are as follows:

At the left clamped end: $\quad\quad y_0 = 0 \quad ; \quad \tan\theta_0 = 0$ $\hfill$ (38)

At the right clamped end: $\quad\quad y_n = 0 \quad ; \quad \tan\theta_n = 0$ $\hfill$ (39)

When the strain values, ε_i, for the present case are used, beam deflection equation (37) should produce condition (39) ($y_n = \tan\theta_n = 0$) at the right clamped end.

Clamped and Simply Supported Beam

The two-point supported beam with the left end clamped and right end simply supported is a special case of a cantilever beam with the tip deflection, y_n (fig. 2) (eq. (12-e)), forced to zero. The end support conditions for the clamped and simply supported beam are as follows:

At the clamped end: $\quad\quad y_0 = 0 \quad ; \quad \tan\theta_0 = 0$ $\hfill$ (40)

At the simply supported end: $\quad y_n = 0 \quad ; \quad \tan\theta_n \neq 0$ $\hfill$ (41)

When the strain values, ε_i, for the present case are used as inputs, beam deflection equation (37) results in condition (41) ($y_n \approx 0$, $\tan\theta_n \neq 0$) at the right simply supported end.

Beam With Two Ends Simply Supported

For the beam with two ends simply supported, the beam deflection slope at the simply supported left end is no longer zero ($\tan\theta_0 \neq 0$). Therefore, to formulate the slope and deflection

equations for this beam, the nonzero term, $\tan\theta_0 \neq 0$ (which was neglected for the cantilever beam case), must be retained in both slope equation (8) and deflection equation (12).

Slope Equation

The slope equation for the beam with two ends simply supported can be written as

$$\tan\theta_1 = \frac{\Delta l}{2c}(\varepsilon_0 + \varepsilon_1) + \tan\theta_0 \quad ; \quad (\tan\theta_0 \neq 0 \text{ at left support}) \qquad (42\text{-}a)$$

$$\tan\theta_2 = \frac{\Delta l}{2c}(\varepsilon_1 + \varepsilon_2) + \tan\theta_1 = \frac{\Delta l}{2c}(\varepsilon_0 + 2\varepsilon_1 + \varepsilon_2) + \tan\theta_0 \qquad (42\text{-}b)$$

$$\tan\theta_3 = \frac{\Delta l}{2c}(\varepsilon_2 + \varepsilon_3) + \tan\theta_2 = \frac{\Delta l}{2c}\left[\varepsilon_0 + 2(\varepsilon_1 + \varepsilon_2) + \varepsilon_3\right] + \tan\theta_0 \qquad (42\text{-}c)$$

$$\tan\theta_4 = \frac{\Delta l}{2c}(\varepsilon_3 + \varepsilon_4) + \tan\theta_3 = \frac{\Delta l}{2c}\left[\varepsilon_0 + 2(\varepsilon_1 + \varepsilon_2 + \varepsilon_3) + \varepsilon_4\right] + \tan\theta_0 \qquad (42\text{-}d)$$

$$\dots\dots\dots\dots\dots\dots\dots\dots\dots$$

$$\tan\theta_n = \frac{\Delta l}{2c}(\varepsilon_{n-1} + \varepsilon_n) + \tan\theta_{n-1} = \frac{\Delta l}{2c}\left[\varepsilon_0 + 2(\varepsilon_1 + \varepsilon_2 + \varepsilon_3 + \dots + \varepsilon_{n-1}) + \varepsilon_n\right] + \tan\theta_0$$

$$= \frac{\Delta l}{2c}\left[\varepsilon_0 + 2\sum_{i=1}^{n-1}\varepsilon_i + \varepsilon_n\right] + \tan\theta_0 \qquad (42\text{-}e)$$

Deflection Equations

Let y_i^B be the deflection of the two-point supported beam at the strain-sensing station, x_i. Deflection equation (12) can then be modified for the beam with two ends simply supported as

$$y_1^B = y_1 + \Delta l \tan\theta_0$$
$$= \frac{(\Delta l)^2}{6c}(2\varepsilon_0 + \varepsilon_1) + \Delta l \tan\theta_0 \quad ; \quad (y_0 = \varepsilon_0 = 0, \ \tan\theta_0 \neq 0 \text{ at left support}) \qquad (43\text{-}a)$$

$$y_2^B = y_2 + 2\Delta l \tan\theta_0$$
$$= \frac{(\Delta l)^2}{6c}(5\varepsilon_0 + 6\varepsilon_1 + \varepsilon_2) + 2\Delta l \tan\theta_0 \qquad (43\text{-}b)$$

$$y_3^B = y_3 + 3\Delta l \tan\theta_0$$
$$= \frac{(\Delta l)^2}{6c}\left[8\varepsilon_0 + 6(2\varepsilon_1 + \varepsilon_2) + \varepsilon_3\right] + 3\Delta l \tan\theta_0 \qquad (43\text{-}c)$$

21

$$y_4^B = y_4 + 4\Delta l \tan\theta_0$$

$$= \frac{(\Delta l)^2}{6c}\left[11\varepsilon_0 + 6\left(3\varepsilon_1 + 2\varepsilon_2 + \varepsilon_3\right) + \varepsilon_4\right] + 4\Delta l \tan\theta_0 \tag{43-d}$$

....

$$y_n^B = y_n + n\Delta l \tan\theta_0$$

$$= \frac{(\Delta l)^2}{6c}\left[(3n-1)\varepsilon_0 + 6\sum_{i=1}^{n-1}(n-i)\varepsilon_i + \varepsilon_n\right] + n\Delta l \tan\theta_0 \quad ; \quad (\varepsilon_0 = \varepsilon_n = 0) \tag{43-e}$$

in which y_i ($i = 1, 2, 3 \dots n$) is the deflection calculated from cantilever beam deflection equation (12). By setting $y_n^B = 0$ in equation (43-e) for the right simply supported end, the unknown slope, $\tan\theta_0$, at the left simply supported end can be expressed in terms of the measured strains, ε_i, as

$$\tan\theta_0 = -\frac{1}{n(\Delta l)}\frac{(\Delta l)^2}{6c}\left[(3n-1)\varepsilon_0 + 6\sum_{i=1}^{n-1}(n-i)\varepsilon_i + \varepsilon_n\right] = -\frac{1}{n(\Delta l)}y_n \tag{44}$$

In equation (44), the last term (containing y_n) can be obtained from equation (12-e). In light of equation (44), beam deflection equation (43) takes on the form of equation (37). Thus, for the beam with two ends simply supported, equations (43) and (37) will result in identical beam deflection curves.

Symmetrically Loaded Beam

If the beam is symmetrically loaded (concentrated or distributed), then $\tan\theta_0 = -\tan\theta_n$, and equation (42-e) becomes

$$\tan\theta_0 = -\frac{\Delta l}{4c}\left[\varepsilon_0 + 2(\varepsilon_1 + \varepsilon_2 + \varepsilon_3 + \dots + \varepsilon_{n-1}) + \varepsilon_n\right] \quad ; \quad (\varepsilon_0 = \varepsilon_n = 0) \tag{45}$$

For a beam that is symmetrically loaded and simply supported, the slopes, $\tan\theta_0$, calculated from equations (44) and (45) should be identical, although their mathematical expressions are different. This match can be verified by considering an example of a simply supported beam in which $n = 4$ ($\varepsilon_0 = \varepsilon_4 = 0$) under central vertical load. The symmetry condition results in ($\varepsilon_3 = \varepsilon_1$), and equation (44) becomes

$$\tan\theta_0 = -\frac{\Delta l}{24c}[11\varepsilon_0 + 6(3\varepsilon_1 + 2\varepsilon_2 + \varepsilon_3) + \varepsilon_4]$$

$$= -\frac{\Delta l}{2c}(2\varepsilon_1 + \varepsilon_2) \quad ; \quad (n = 4;\ \varepsilon_0 = \varepsilon_4 = 0;\ \varepsilon_3 = \varepsilon_1) \tag{46}$$

When the same strain conditions are applied ($\varepsilon_0 = \varepsilon_4 = 0;\ \varepsilon_3 = \varepsilon_1$), slope equation (45) becomes

$$\tan\theta_0 = -\frac{\Delta l}{4c}\left[\varepsilon_0 + 2(\varepsilon_1 + \varepsilon_2 + \varepsilon_3) + \varepsilon_4\right]$$
$$= -\frac{\Delta l}{2c}(2\varepsilon_1 + \varepsilon_2)$$
$$;\quad (n = 4; \varepsilon_0 = \varepsilon_4 = 0; \varepsilon_3 = \varepsilon_1) \qquad (47)$$

For the present centrally loaded simply supported beam ($n = 4$; $\varepsilon_0 = \varepsilon_4 = 0$; $\varepsilon_3 = \varepsilon_1$), equations (46) and (47) result in identical mathematical expressions for the left end slope, $\tan\theta_0$.

Plates

For plates, the strain-sensing system requires multiple parallel strain-sensing lines (fig. 5) across the two opposite edges to generate a three-dimensional deformed shape. A narrow strip of the plate along each sensing line can be considered as a two-point supported beam. Hence, deflection equations (37) or (43) developed for the two-point supported beam also are applicable to the predictions of the deformed shapes of plates.

VALIDATION OF THEORY

This section verifies the mathematical accuracy of the bending and torsion displacement equations developed for the uniform cantilever beam. The mathematical expressions of the displacement equations are compared with those of classical cantilever beam theory.

Bending Case

To test the accuracy of the mathematical expressions of the slope and deflection equations, a cantilever beam of length l subjected to an upward tip load of P is used as an example. For this case the moment, M, and associated bending strain are linearly decreasing functions of x from the built-in end of the beam toward zero at the beam tip.

Assume that the cantilever beam has five bending strain sensors $\{\varepsilon_0, \varepsilon_1, \varepsilon_2, \varepsilon_3, \varepsilon_4\}$ equally spaced over the span by $\Delta l = l/4$ along the bottom surface of the beam. The purpose is to determine whether the calculated functional expressions of the tip slope and tip deflection of the cantilever beam match those given by classical beam theory.

Bending Strains

For a cantilever beam of length l subjected to a tip load of P, the bending strain (or bending moment) is a linearly decreasing function of x from the built-in end of the beam down to zero at the free end of the beam. The bending strains at the strain-sensing stations, x_i ($= 0, 1, 2, 3, 4$), can then be written as

$$\varepsilon_1 = \left(1 - \frac{\Delta l}{l}\right)\varepsilon_0 = \left(1 - \frac{\Delta l}{4\Delta l}\right)\varepsilon_0 = \frac{3}{4}\varepsilon_0 \qquad (48\text{-}a)$$

$$\varepsilon_2 = \left(1 - \frac{2\Delta l}{l}\right)\varepsilon_0 = \left(1 - \frac{2\Delta l}{4\Delta l}\right)\varepsilon_0 = \frac{2}{4}\varepsilon_0 \qquad (48\text{-}b)$$

$$\varepsilon_3 = \left(1 - \frac{3\Delta l}{l}\right)\varepsilon_0 = \left(1 - \frac{3\Delta l}{4\Delta l}\right)\varepsilon_0 = \frac{1}{4}\varepsilon_0 \qquad (48\text{-}c)$$

$$\varepsilon_n = \varepsilon_4 = \left(1 - \frac{4\Delta l}{l}\right)\varepsilon_0 = \left(1 - \frac{4\Delta l}{4\Delta l}\right)\varepsilon_0 = 0 \quad \text{(Beam tip)} \qquad (48\text{-}d)$$

Tip Slope

When strain equation (48) is substituted into slope equation (8-d), the beam tip slope is calculated as

$$\tan\theta_n = \tan\theta_4 = \frac{\Delta l}{2c}\left[\varepsilon_0 + 2(\varepsilon_1 + \varepsilon_2 + \varepsilon_3) + \varepsilon_4\right] = \frac{\Delta l \varepsilon_0}{2c}\left[1 + 2\left(\frac{3}{4} + \frac{2}{4} + \frac{1}{4}\right) + 0\right]$$

$$= \frac{l}{2c}\varepsilon_0 = \frac{l}{2c}\left(\frac{M(0)c}{EI}\right) = \frac{l}{2c}\left(\frac{Plc}{EI}\right) \qquad (49)$$

$$= \frac{Pl^2}{2EI}$$

in which the moment-strain relationship, $\varepsilon_o = \dfrac{M(0)c}{EI}$ (eq. (2)), with $M(0) = Pl$ at the built-in end

$(x = 0)$ is used. Equation (49) is identical to the classical tip slope expressions for a cantilever beam of length l subjected to a vertical load of P at the free end (refs. 2, 3).

Tip Deflection

When strain equation (48) is substituted into deflection equation (12-d), the beam tip deflection is calculated as

24

$$y_n = y_4 = \frac{(\Delta l)^2}{6c}\left[11\varepsilon_0 + 6(3\varepsilon_1 + 2\varepsilon_2 + \varepsilon_3) + \varepsilon_4\right] = \left(\frac{l}{4}\right)^2 \frac{\varepsilon_0}{6c}\left[11 + 6\left(3\times\frac{3}{4} + 2\times\frac{2}{4} + \frac{1}{4}\right) + 0\right]$$

$$= \frac{l^2}{3c}\varepsilon_0 = \frac{l^2}{3c}\frac{M(0)c}{EI} = \frac{l^2}{3c}\frac{(Pl)c}{EI} \tag{50}$$

$$= \frac{Pl^3}{3EI}$$

Again, the relationship $\varepsilon_0 = \dfrac{M(0)c}{EI}$ (eq. (2)) at the built-in end ($x = 0$) and $M(0) = Pl$ is used.

Equation (50) is identical to the tip deflection expressions for a classical cantilever beam of length l subjected to a vertical load of P at the free end (refs. 2, 3).

The present example verifies the accuracy and dependability of the slope and deflection equations that have been developed. This example also provides confidence for applying these displacement equations to monitor the in-flight deformed shape of the Helios flying wing.

Torsion Case

Assume that the cantilever beam has four distortion strain sensors $\{\gamma_0, \gamma_1, \gamma_2, \gamma_3\}$ equally spaced by $\Delta l = l/4$ along the cantilever beam, which is subjected to a twisting moment of T at the tip. The purpose is to determine whether the calculated functional expression of the tip twist angle matches that given by classical beam theory.

Distortion Strains

For the case of constant twisting along the span (that is, $T_0 = T_1 = T_2 = T_3 = T_4 = T$), the surface twist angles (shear strains) are constant at all sensing stations. Namely,

$$\gamma_1 = \gamma_2 = \gamma_3 = \gamma_0 \tag{51}$$

Tip Twist Angle

From equation (15-d), the tip twist angle, $\phi_n (= \phi_4)$, can be written as

$$\phi_n = \phi_4 = \frac{\Delta l}{c}(\gamma_0 + \gamma_1 + \gamma_2 + \gamma_3) \tag{52}$$

In light of equation (51), the tip twist angle of equation (52) becomes

$$\phi_n = \phi_4 = \frac{\Delta l}{c}(\gamma_0 + \gamma_1 + \gamma_2 + \gamma_3) = \frac{l}{4c}(4\gamma_0) = \frac{l}{c}\gamma_0 = \frac{l}{c}\left(\frac{Tc}{GJ}\right)$$
$$= \frac{Tl}{GJ}$$

(53)

Equation (53) is exactly the same as the expression for the tip cross-sectional twist angle of the classical cantilever beam of length l subjected to a tip twisting moment of T (refs. 2, 3).

FINITE-ELEMENT ANALYSIS

To test the prediction accuracy of deflection equation (12), strain sensor data and measured deflection data are needed. Before the experimental data are available, an alternative approach is to use finite-element analysis to generate the desired bending strain and deflection data. The Structural Performance And Resizing (SPAR) finite-element computer program (ref. 5) has been used for this purpose. The next section describes the method for generating the bending strains, ε_i, from the SPAR outputs.

Generation of the Bending Strains

From the SPAR nodal displacements outputs, the axial displacements, $\{\delta_1, \delta_2\}$, at the two ends of the element lying in the lower outermost surface can be used to calculate the bending strain for that particular element. If the strain-sensing station, x_i, is located in the middle of the element, then the displacement differential, $(\delta_2 - \delta_1)$, can be divided by the finite-element span-wise length, e, to generate the desired bending strain, ε_i, at the strain-sensing station, x_i. Namely,

$$\varepsilon_i = \left(\frac{\delta_2 - \delta_1}{e}\right)_i$$

(54)

If the strain-sensing station, x_i, is located at the juncture of two adjacent elements, then the following average strain value is used for the strain, ε_i, at the strain-sensing station, x_i:

$$\varepsilon_i = \frac{1}{2}\left[\left(\frac{\delta_2 - \delta_1}{e}\right)_{i+} + \left(\frac{\delta_2 - \delta_1}{e}\right)_{i-}\right]$$

(55)

In equation (55), $\{()_{i+}, ()_{i-}\}$ denote the elements on the outboard and inboard side, respectively, of the strain-sensing station, x_i.

The SPAR bending strains calculated from equations (54) and (55) can be input to equation (12) to calculate the beam deflections. These calculations can then be compared to the deflections obtained from the SPAR outputs to check the prediction accuracy of displacement equation (12).

Cantilever Tube Models

Figure 6 shows a typical finite-element model for a cantilever tube with a length of $l = 100.5$ in. The model consists of 100 four-node shell elements in the axial direction and 36 in the circumferential direction. The end disk was added so that the tip load can be applied at the disk center. The cantilever tube is fixed in space at the left end and subjected to an upward vertical load of $P = 100$ lb at the tip. The following three types of tubes fabricated with different materials were considered:

1. Aluminum tube

2. Four-ply composite tube: (45/-45/-45/45) carbon fiber composite tube

3. Helios composite tube: 4 plies (45/-45/-45/45) of carbon fiber composite wall with 27 plies ($0_8/90/0_8/90/0_9$) of carbon fiber composite reinforcements in the 60-deg regions of the top and bottom of the spar caps (actual Helios wing spar).

Table 1 lists the dimensions and table 2 lists the material properties of these types of tubes.

Table 1. Dimensions of three types of tubular spars.

Tube type	l, in.	a, in.	c, in.	t, in.
Aluminum	100.5	4.0	4.01148	0.02296
Four-ply composite	100.5	4.0	4.01148	0.02296
Helios composite	100.5	4.0[*] (4.07749)[**]	4.16646[**]	0.02296[*] (0.17794)[**]

* Four-ply regions, ** 31-ply regions

Table 2. Material properties of carbon fiber composite and aluminum tubes.

Carbon fiber composite	Aluminum
$E_L = 16.3 \times 10^6$ lb/in^2	$E = 10.5 \times 10^6$ lb/in^2
$E_T = 0.98 \times 10^6$ lb/in^2	NA
$G_{LT} = 0.71$ lb/in^2	$G = 4.0 \times 10^6$ lb/in^2
$\nu_{LT} = 0.34$	$\nu = 0.33$

Wing Box Model

Figure 7 shows the tapered cantilever wing box model. The box is made of aluminum (table 2), and has a length of $l = 100$ in., width of $w = 17$ in., and depth of $2c_0 = 4$ in. at the root, which tapers down to a depth of $2c_n = 3$ in. at the tip. The upper and lower skins and the vertical walls have an identical thickness of $t = 0.02296$ in. (wall thickness of an aluminum cantilever tube). The wing box was subjected to a vertical load of $P = 100$ lb and a torque of

$T = (P/2) \times w = 850$ in-lb at the wing box tip. The torque was generated by applying two equal and opposite forces of $P/2 = 50$ lb at the two corners of the wing box tip (fig. 7).

Beam Models

The two-point supported beam models are identical to the cantilever tube model (fig. 6) except that the support conditions have been changed. Figure 8 shows the two-point supported tubular beam models subjected to a downward force of $P = -200$ lb at the beam center, under three cases of support conditions: (1) both ends clamped (fig. 8(a)), (2) left end clamped and right end simply supported (fig. 8(b)), and (3) both ends simply supported (fig. 8(c)). The deformed shapes also are shown.

Plate Model

Figure 9 shows the dimensions of an aluminum square plate (l = 24 in., w = 24 in., t = 0.2 in.). The plate was subjected to a downward force of P = -400 lb at the plate center, under two edge-support conditions: (1) four edges clamped (fig. 9(a)), and (2) four edges simply supported (fig. 9 (b)). Because of loading symmetry, only one quarter of the plate was modeled. For the quarter model, a downward force of only $P/4 = -100$ lb was applied.

RESULTS

The SPAR displacement outputs were used to generate the bending strain, ε_i, for each strain-sensing station. These strain values were then input to the appropriate deflection equations to calculate the deflections at all the strain-sensing stations of all the study cases.

Cantilever Tubes

This section presents the results of three types of cantilever tubes (aluminum, four-ply composite, and Helios composite). The deflections calculated from the Ko displacement theories are compared with those calculated from the SPAR finite-element analysis.

Aluminum Cantilever Tube

Figure 10 shows the bending strains, ε_i, at the strain-sensing stations on the aluminum tube, calculated from the SPAR nodal displacement outputs. The strain data from figure 10 were used to calculate the deflections, y_i, from deflection equation (12). To find the minimum number of strain sensors required for acceptable accuracy of the deflection predictions, three cases of n (2, 4, 8), were considered. Table 3 compares the deflections, y_i, calculated from deflection equation (12) to those obtained from the SPAR outputs for the different n values. Note that the difference between the deflection values calculated from the SPAR program and those calculated from deflection equation (12) is minimal. Also note that the effect of the number of sensing stations, n, is negligible for the present uniform cantilever aluminum tube.

Table 3(a). Comparison of deflections calculated from SPAR with those calculated from deflection equation (12); aluminum cantilever tube; $n = 2$.

	Deflection (y_i), in.		
	y_0	y_1	y_2
SPAR	0.0000	0.2253	0.7138
Deflection equation (12)	0.0000	0.2184	0.7000
Difference, percent	0.0000	3.0451	1.9389

Table 3(b). Comparison of deflections calculated from SPAR with those calculated from deflection equation (12); aluminum cantilever tube; $n = 4$.

	Deflection (y_i), in.				
	y_0	y_1	y_2	y_3	y_4
SPAR	0.0000	0.0636	0.2253	0.4530	0.7138
Deflection equation (12)	0.0000	0.0604	0.2206	0.4468	0.7056
Difference, percent	0.0000	5.1242	2.0996	1.3707	1.1544

Table 3(c). Comparison of deflections calculated from SPAR with those calculated from deflection equation (12); aluminum cantilever tube; $n = 8$.

	Deflection (y_i), in.								
	y_0	y_1	y_2	y_3	y_4	y_5	y_6	y_7	y_8
SPAR	0.0000	0.0179	0.0636	0.1341	0.2253	0.3330	0.4530	0.5814	0.7138
Deflection equation (12)	0.0000	0.0157	0.0605	0.1302	0.2205	0.3273	0.4465	0.5738	0.7051
Difference, percent	0.0000	12.2142	4.9356	2.9223	2.1262	1.7208	1.4524	1.3072	1.2230

Data from table 3 are plotted in figure 11 for different n values. The two sets of deflection curves are quite close, indicating the accuracy of displacement equation (12). The deflection curves calculated from deflection equation (12) lie slightly below those obtained from the SPAR outputs. Notice that the difference in the tip deflection did not improve when n was increased from 4 to 8.

Four-Ply Composite Cantilever Tube

Figure 12 shows the bending strains, ε_i, at the strain-sensing stations on the four-ply composite tube calculated from the SPAR outputs. In this case the SPAR strain curve is practically linear. The strain data from figure12 were used to calculate the deflections, y_i, from deflection equation (12) under three cases of n (2, 4, 8). Table 4 compares the deflections, y_n, calculated from deflection equation (12) to those obtained from the SPAR outputs. Again, the difference between the values calculated from the SPAR program and those calculated from deflection equation (12) is minimal.

Table 4(a). Comparison of deflections calculated from SPAR with those calculated from deflection equation (12); four-ply composite cantilever tube; $n = 2$.

	Deflection (y_i), in.		
	y_0	y_1	y_2
SPAR	0.0000	0.9110	2.8946
Deflection equation (12)	0.0000	0.9170	2.9373
Difference, percent	0.0000	0.6641	1.4741

Table 4(b). Comparison of deflections calculated from SPAR with those calculated from deflection equation (12); four-ply composite cantilever tube; $n = 4$.

	Deflection (y_i), in.				
	y_0	y_1	y_2	y_3	y_4
SPAR	0.0000	0.2577	0.9110	1.8347	2.8946
Deflection equation (12)	0.0000	0.2515	0.9156	1.8553	2.9331
Difference, percent	0.0000	2.4058	0.5116	1.1223	1.3290

Table 4(c). Comparison of deflections calculated from SPAR with those calculated from deflection equation (12); four-ply composite cantilever tube; $n = 8$.

	Deflection (y_i), in.								
	y_0	y_1	y_2	y_3	y_4	y_5	y_6	y_7	y_8
SPAR	0.0000	0.0749	0.2577	0.5421	0.9110	1.3475	1.8347	2.3558	2.8946
Deflection equation (12)	0.0000	0.0658	0.2519	0.5413	0.9167	1.3610	1.8570	2.3877	2.9356
Difference, percent	0.0000	12.2264	2.2545	0.1531	0.6301	1.0000	1.2176	1.3526	1.4154

Data from table 4 are plotted in figure 13 for different n values. The two sets of deflection curves are quite close, indicating the accuracy of deflection equation (12). The deflection curves calculated from deflection equation (12) lie slightly above those obtained from the SPAR outputs. Again, the effect of n is negligible.

Helios Composite Cantilever Tube

Figure 14 shows the bending strains, ε_i, at the strain-sensing stations on the Helios composite tube calculated from the SPAR outputs. In this case the SPAR strain curve is nearly linear. The strain data from figure 14 were used to calculate the deflections, y_i, from deflection equation (12) under three cases of n (2, 4, 8). Table 5 compares the deflections, y_i, calculated from deflection equation (12) to those obtained from the SPAR outputs. Again, the difference between the values calculated from the SPAR program and those calculated from deflection equation (12) is minimal.

Table 5(a). Comparison of deflections calculated from SPAR with those calculated from deflection equation (12); Helios composite cantilever tube; $n = 2$.

	Deflection (y_i), in.		
	y_0	y_1	y_2
SPAR	0.0000	0.2167	0.6721
Deflection equation (12)	0.0000	0.2115	0.6739
Difference, percent	0.0000	2.3863	0.2678

Table 5(b). Comparison of deflections calculated from SPAR with those calculated from deflection equation (12); Helios composite cantilever tube; $n = 4$.

	Deflection (y_i), in.				
	y_0	y_1	y_2	y_3	y_4
SPAR	0.0000	0.0673	0.2167	0.4284	0.6721
Deflection equation (12)	0.0000	0.0580	0.2096	0.4232	0.6677
Difference, percent	0.0000	13.7952	3.2726	1.1976	0.6443

Table 5(c). Comparison of deflections calculated from SPAR with those calculated from deflection equation (12); Helios composite cantilever tube; $n = 8$.

	Deflection (y_i), in.								
	y_0	y_1	y_2	y_3	y_4	y_5	y_6	y_7	y_8
SPAR	0.0000	0.0240	0.0673	0.1324	0.2167	0.3166	0.4284	0.5479	0.6721
Deflection equation (12)	0.0000	0.0152	0.0577	0.1235	0.2089	0.3099	0.4227	0.5432	0.6676
Difference, percent	0.0000	36.7126	14.2263	6.6853	3.5818	2.1381	1.3307	0.8669	0.6725

Data from table 5 are plotted in figure 15 for different n values. The two sets of deflection curves are quite close, indicating the accuracy of deflection equation (12). The deflection curves calculated from deflection equation (12) lie slightly below those obtained from the SPAR outputs (especially at lower values of n). Again, the effect of n is insignificant.

Wing Box

Figure 16 shows plots of the front and rear bending strains, $\{\varepsilon_i, \varepsilon_i'\}$, for the tapered wing box obtained from the SPAR outputs. Because of the taper and torsion effect, the two SPAR strain curves are no longer linear. The front strain curve is convex downward from the wing root toward zero at the wingtip. Conversely, the rear strain curve is convex downward near the wing root and then turns to concave downward toward zero at the wingtip. The strain data from figure 16 were used to calculate the front and rear deflections, $\{y_i \ y_i'\}$, from deflection equations (30) (tapered) and (35) (stepwise) for $n = 8$. Tables 6 and 7 compare the front and rear deflections, $\{y_i \ y_i'\}$,

respectively, calculated from equations (30) and (35) ({n, i} replaced with {i, j}) to those obtained from the SPAR outputs.

Table 6. Comparison of front deflections calculated from SPAR with those calculated from deflection equations (30) (tapered) and (35) (stepwise); aluminum wing box; $n = 8$; front sensors.

	Deflection (y_i), in.								
	y_0	y_1	y_2	y_3	y_4	y_5	y_6	y_7	y_8
SPAR	0.0000	0.0229	0.0864	0.1892	0.3285	0.5008	0.7008	0.9218	1.1559
Tapered deflection equation (30)	0.0000	0.0208	0.0818	0.1807	0.3138	0.4771	0.6656	0.8725	1.0894
Difference from SPAR, percent	0.0000	9.3961	5.3910	4.5190	4.4956	4.7332	5.0255	5.3481	5.7489
Stepwise deflection equation (35)	0.0000	0.0209	0.0820	0.1809	0.3141	0.4774	0.6658	0.8725	1.0892
Difference, from SPAR, percent	0.0000	8.9601	5.1596	4.3816	4.4074	4.6813	4.9984	5.3470	5.7714

Table 7. Comparison of rear deflections calculated from SPAR with those calculated from deflection
equations (30) (tapered) and (35) (stepwise); aluminum wing box; $n = 8$; rear sensors.

	Deflection (y_i'), in.								
	y_0'	y_1'	y_2'	y_3'	y_4'	y_5'	y_6'	y_7'	y_8'
SPAR	0.0000	0.0227	0.0844	0.1801	0.3045	0.4525	0.6182	0.7960	0.9813
Tapered deflection equation (30)	0.0000	0.0200	0.0779	0.1688	0.2868	0.4259	0.5805	0.7450	0.9140
Difference from SPAR, percent	0.0000	11.9683	7.6339	6.2398	5.8383	5.8830	6.0998	6.4161	6.8661
Stepwise deflection equation (35)	0.0000	0.0201	0.0781	0.1690	0.2869	0.4259	0.5804	0.7446	0.9133
Difference from SPAR, percent	0.0000	11.5274	7.4206	6.1342	5.7891	5.8764	6.1224	6.4651	6.9385

Note from tables 6 and 7 that the difference between the values of { y_i y_i' } calculated from the SPAR program and those calculated from equations (30) and (35) is minimal. Tapered deflection equation (30) and stepwise deflection equation (35) resulted in extremely close deflections, which implies that the tapered and stepwise theories are quite accurate for the present slightly tapered cantilever wing box.

Figure 17 compares the deflections, y_i (table 6) and y_i' (table 7), calculated by means of different methods. Note that the deflection curves generated from equations (30) and (35) for each sensing line are pictorially indistinguishable and reasonably close to the corresponding SPAR deflection curves.

Table 8 shows the cross-sectional twist angle, ϕ_i, calculated from equation (36) using the data of { y_i y_i' } provided in tables 6 and 7, respectively. The data in table 8 show that both tapered deflection equation (30) and stepwise deflection equation (35) resulted in extremely close values of ϕ_i, which are very close to the values of ϕ_i calculated from the SPAR program. The similarity

among these values implies that either of the two tapered beam theories can be used to obtain quite accurate results for the present slightly tapered cantilever wing box.

Table 8. Comparison of cross-sectional twist angles calculated from SPAR and equation (36) using tapered deflection equation (30) and stepwise deflection equation (35); aluminum wing box; $n = 8$.

	Cross-sectional twist angle (ϕ_i), deg								
	ϕ_0	ϕ_1	ϕ_2	ϕ_3	ϕ_4	ϕ_5	ϕ_6	ϕ_7	ϕ_8
SPAR	0.0000	0.0008	0.0070	0.0308	0.0809	0.1629	0.2784	0.4239	0.5883
Tapered deflection equation (30)	0.0000	0.0027	0.0130	0.0399	0.0910	0.1727	0.2868	0.4299	0.5914
Difference from SPAR, percent	0.0000	224.0000	85.5769	29.3603	12.5417	6.0308	3.0142	1.4113	0.5328
Stepwise deflection equation (35)	0.0000	0.0027	0.0131	0.0401	0.0915	0.1735	0.2879	0.4312	0.5929
Difference from SPAR, percent	0.0000	224.0000	86.5385	30.1258	13.1250	6.5067	3.4136	1.7293	0.7906

Note that the high percentage of errors shown in $\{\phi_1, \phi_2, \phi_3\}$ is not significant, because the small numbers are divided by small numbers (that is, noise level). The low error levels at the wingtip, however, are significant.

Figure 18 compares the cross-sectional twist angles, ϕ_i, using the data from table 8. The cross-sectional twist angle curves generated by equation (36) using the deflections calculated from tapered deflection equation (30) and stepwise deflection equation (35) are pictorially on top of each other and very close to the cross-sectional twist angle curve generated from the SPAR program.

These results demonstrate that the two-line strain-sensing system could produce quite accurate bending deflection and twist angle curves for the present slightly tapered wing box without the need for shear strain sensors.

Simple Beams

This section presents the results of three types of two-point supported beams (both ends clamped, left end clamped and right end simply supported, and both ends simply supported). The deflections calculated from the Ko displacement theories are compared with those calculated from the SPAR finite-element analysis.

Both Ends Clamped

Figure 19 shows the bending strains, ε_i, for the beam with both ends clamped, calculated from equations (54) and (55) using the SPAR displacement outputs. The beam deflections, y_i, were then calculated from deflection equation (12) using the SPAR strain values presented in figure 19. Table 9 presents these deflections and compares them to the deflections, y_i, obtained from the SPAR outputs and those calculated from classical beam theory.

Table 9. Comparison of deflections calculated from deflection equation (12) with those calculated from SPAR and classical beam theory; two-point supported aluminum tubular beam with both ends clamped; $P = -200$ lb at beam center; $n = 8$.

	Deflection (y_i), in.								
	y_0	y_1	y_2	y_3	y_4 (load point)	y_5	y_6	y_7	y_8
SPAR	0.0000	-0.0047	-0.0132	-0.0217	-0.0264	-0.0217	-0.0132	-0.0047	0.0000
Classical beam theory	0.0000	-0.0034	-0.0109	-0.0184	-0.0218	-0.0184	-0.0109	-0.0034	0.0000
Deflection equation (12)	0.0000	-0.0032	-0.0107	-0.0182	-0.0215	-0.0182	-0.0107	-0.0032	0.0000
Difference from SPAR, percent	0.0000	31.9149	18.9394	16.1290	18.5606	16.1290	18.9394	31.9149	0.0000
Difference from classical beam theory, percent	0.0000	5.8824	1.8349	1.0870	1.3761	1.0870	1.8349	5.8824	0.0000

(-) implies downward deflections.

The deflections, y_i, presented in table 9 are plotted in figure 20 for visual comparison. Note that the deflection curves generated from equation (12) and those generated from classical beam theory agree very well with only a 1.08-percent difference at the beam center. The difference between the deflections calculated from equation (12) and those calculated from the SPAR program (16.51 percent at the beam center) is attributed to the shear effect, which tends to increase the beam deflections. To prove this point, the SPAR program was run again under two cases of input conditions. In case 1, the nodal axial displacements were set to zero to eliminate beam cross-sectional rotations and obtain deflections purely caused by shear deformation. In case 2, the shear modulus, G, was set to infinity ($G \rightarrow \infty$) in the SPAR program to simulate the classical beam case. Table 10 compares the beam center deflections calculated from the SPAR program under different input conditions to those calculated from classical beam theory.

Table 10. Comparison of beam center deflections calculated from SPAR with those calculated from classical beam theory; two-point supported aluminum tubular beam with both ends clamped; $P = -200$ lb at beam center.

	SPAR $(G \neq \infty)$	SPAR (shear only)	SPAR $(G \rightarrow \infty)$	Classical beam theory
Beam center deflection, in.	0.2636-1	0.0442-1	0.2194-1	0.2181-1

The data presented in table 10 prove that the shear effect is indeed considerable for the present tubular beam with both ends clamped. In general, the shear effect becomes important only when the beam is short with an aspect ratio of $l/2a$ less than 4 ($l/2a < 4$, ref. 3, p. 201). The present tubular beam has an aspect ratio of $l/2a = 12.56$ (=100.5 ÷ 8) and therefore does not belong in the short beam category. The thin walled tubular geometry, however, and the two inflection points (curvature sign changes) in the deflection curve that divide the beam into three deformed segments (fig. 20) seem to cause the beam to exhibit considerable shear effect of approximately 17 percent of the total deflection at the beam center.

Clamped and Simply Supported

Figure 21 shows the strains, ε_i, for the beam with a clamped left end and simply supported right end calculated from equations (54) and (55) using the SPAR displacement outputs. The SPAR strain values presented in figure 21 were used to calculate the beam deflections, y_i, from deflection equation (12). Table 11 presents these deflections and compares them to the deflections, y_i, calculated from the SPAR program and those calculated from classical beam theory.

Table 11. Comparison of deflections calculated from deflection equation (12) with those calculated from SPAR and classical beam theory; two-point supported aluminum tubular beam with a clamped left end and simply supported right end; $P = -200$ lb at beam center; $n = 8$.

	Deflection (y_i), in.								
	y_0	y_1	y_2	y_3	y_4 (load point)	y_5	y_6	y_7	y_8
SPAR	0.0000	-0.0069	-0.0200	-0.0340	-0.0439	-0.0415	-0.0320	-0.0173	0.0000
Classical beam theory	0.0000	-0.0052	-0.0170	-0.0299	-0.0382	-0.0376	-0.0293	-0.0159	0.0000
Deflection equation (12)	0.0000	-0.0053	-0.0172	-0.0300	-0.0383	-0.0378	-0.0297	-0.0162	0.0000
Difference from SPAR, percent	0.0000	23.1884	14.000	11.7647	12.7563	8.9157	7.1875	6.3584	0.0000
Difference from classical beam theory, percent	0.0000	1.9231	1.1765	0.3344	0.2618	0.5319	1.3652	1.8868	0.0000

(-) implies downward deflections.

The deflection data listed in table 11 are plotted in figure 22 for graphical comparison. As in the previous case, the deflection curve generated from equation (12) agrees fairly well with that generated from classical beam theory with only a 0.36-percent difference at the beam center. It is off by 12.79 percent, however, from the SPAR deflection curve at the beam center. Again, the difference between the deflections calculated from the SPAR program and those calculated from deflection equation (12) is caused by shear deformation. When the shear modulus, G, was set to infinity ($G \rightarrow \infty$) in the SPAR program, the deflection curve closely approached that calculated from classical beam theory. Again, the present tubular beam exhibited the short beam behavior ($l/2a < 4$, ref. 3, p. 201) caused by the existence of one inflection point in the deflection curve.

Both Ends Simply Supported

Figure 23 plots the strains, ε_i, for the beam with both ends simply supported, calculated from equations (54) and (55) using the SPAR displacement outputs. The SPAR strain values presented in figure 23 were used to calculate the beam deflections, y_i, from deflection equation (12).

Table 12 presents these deflections and compares them to the deflections calculated from the SPAR program and those calculated from classical beam theory.

Table 12. Comparison of deflections calculated from deflection equation (43) with those calculated from SPAR and classical beam theory; two-point supported aluminum tubular beam with both ends simply supported; $P = -200$ lb at beam center; $n = 8$.

	Deflection (y_i^B), in.								
	y_0^B	y_1^B	y_2^B	y_3^B	y_4^B (load point)	y_5^B	y_6^B	y_7^B	y_8^B
SPAR	0.0000	–0.0333	–0.0624	–0.0834	–0.0924	–0.0834	–0.0624	–0.0333	0.0000
Classical beam theory	0.0000	–0.0320	–0.0600	–0.0798	–0.0873	–0.0798	–0.0600	–0.0320	0.0000
Deflection equation (43)	0.0000	–0.0318	–0.0594	–0.0787	–0.0860	–0.0787	–0.0594	–0.0318	0.0000
Difference from SPAR, percent	0.0000	4.5045	4.8077	5.6355	6.9264	5.6355	4.8077	4.5045	0.0000
Difference from classical beam theory, percent	0.0000	0.6250	1.0000	1.3784	1.4891	1.3784	1.0000	0.6250	0.0000

The deflection data listed in table 12 are plotted in figure 24 for visual comparison. Note that the deflection curve generated from equation (12) is very close to that generated from classical beam theory with a small difference of only 1.49 percent at the beam center. For the beam with both ends simply supported, which has no inflection points, the difference between the deflections calculated from equation (43) and those calculated from the SPAR program is only 6.93 percent at the beam center. Again, this deflection differential is caused by the shear effect, because when the shear modulus, G, was set to infinity ($G \to \infty$), the SPAR program produced a deflection curve that was very close to that generated from classical beam theory.

Plates

This section presents the deflection predictions of plates under two different edge support conditions (four edges clamped and four edges simply supported). The deflections calculated from the Ko displacement theories are compared with those calculated from the SPAR finite-element analysis.

Four Edges Clamped

Figure 25 shows the strains, ε_i, along the axis of symmetry of a clamped square plate (fig. 5), calculated from the SPAR displacement outputs using strain equations (54) and (55). The SPAR strain values presented in figure 25 were used to calculate the deflections, y_i, along the axis of symmetry from cantilever beam deflection equation (12). Table 13 lists the results and compares them with the deflections calculated from the SPAR program.

Table 13. Comparison of deflections along the axis of symmetry calculated from SPAR with those calculated from cantilever beam deflection equation (12); square plate with four edges clamped; $P = -400$ lb at plate center; $n = 8$.

	Deflection (y_i), in.								
	y_0	y_1	y_2	y_3	y_4 (load point)	y_5	y_6	y_7	y_8
SPAR	0.0000	-0.0067	-0.0213	-0.0380	-0.0481	-0.0380	-0.0213	-0.0067	0.0000
Deflection equation (12)	0.0000	-0.0066	-0.0213	-0.0378	-0.0469	-0.0367	-0.0189	-0.0031	0.0047
Difference, percent	0.0000	1.6442	0.0939	0.4474	2.5572	3.5263	11.0798	54.1106	--------

|<----------------Left-hand region --------------->|<---------------Right-hand region-------------->

Note from table 13 that the deflections calculated from equation (12) and those calculated from the SPAR program are very similar in the left-hand region ($i = 0 - 4$). Beyond the center loading point ($i = 4$), the differences between the deflections gradually increase in the right-hand region ($i = 4 - 8$), resulting in a small nonzero upward deflection, $y_8 = 0.0047$ in., at the right support. The reason for this nonzero upward deflection is the local strain perturbation created by the concentrated load at the station, $i = 4$ (plate center), which affects the deflection calculations for the right-hand region. For the present symmetrical loading case, the deflection data calculated from deflection equation (12) for the left-hand region can be used for the right-hand region to avoid error accumulation in the direct deflection calculations.

When deflection equation (37) (corrected for the two-point supported beam) is used, the resulting deflection curve falls very close to the deflection curve calculated from the SPAR program for the right-hand region. As shown in table 14, however, the percent difference for the left-hand region increases slightly.

Table 14. Comparison of deflections along the axis of symmetry calculated from SPAR with those calculated from simple beam deflection equation (37); square plate with four edges clamped; $P = -400$ lb at plate center; $n = 8$.

	Deflection (y_i), in.								
	y_0	y_1	y_2	y_3	y_4 (load point)	y_5	y_6	y_7	y_8
SPAR	0.0000	-0.0067	-0.0213	-0.0381	-0.0481	-0.0380	-0.0213	-0.0067	0.0000
Deflection equation (37)	0.0000	-0.0072	-0.0225	-0.0396	-0.0492	-0.0396	-0.0225	-0.0072	0.0000
Difference, percent	0.0000	7.4627	5.6338	4.2105	2.2869	4.2105	5.6338	7.4627	0.0000

|<----------------Left-hand region -------------->|<---------------Right-hand region-------------->

The deflection data from tables 13 and 14 are plotted in figure 26 for graphical comparison. Note that the deflection curves generated from equation (12) and those generated from the SPAR program are very close in the left-hand region but gradually deviate as the right end is approached. The curve generated from equation (37) exhibits better overall predictions.

Four Edges Simply Supported

Figure 27 shows the strains, ε_i , along the axis of symmetry of a four-edge simply supported square plate (fig. 5), calculated from the SPAR displacement outputs using strain equations (54) and (55). The SPAR strain values presented in figure 27 were used as inputs to deflection equation (43) to calculate the deflections, y_i , along the axis of symmetry. Table 15 compares these results to the deflections, y_i , calculated from the SPAR program.

Table 15. Comparison of deflections along the axis of symmetry calculated from SPAR with those calculated from deflection equation (43); square plate with four edges simply supported; $P = -400$ lb at plate center; $n = 8$.

	Deflection (y_i^B), in.								
	y_0^B	y_1^B	y_2^B	y_3^B	y_4^B (load point)	y_5^B	y_6^B	y_7^B	y_8^B
SPAR	0.0000	-0.0320	-0.0622	-0.0876	-0.1005	-0.0876	-0.0622	-0.0320	0.0000
Deflection equation (43)	0.0000	-0.0330	-0.0640	-0.0898	-0.1021	-0.0898	-0.0640	-0.0330	0.0000
Difference, percent	0.0000	3.1250	2.8939	2.5114	1.5920	2.5114	2.8939	3.1250	0.0000

|<----------------Left-hand region -------------->|<--------------Right-hand region--------------->

The deflection data from table 15 are plotted in figure 28 for visual comparison. Note that the deflection curve calculated from equation (43) and the deflection curve calculated from the SPAR program are quite close. The slight difference between the two curves is pictorially inconspicuous.

DISCUSSION

In-flight predictions of the deformed shape of the ultralightweight flying wing require the installation of multiple bending and distortion strain sensors, equally spaced on the surface of the wing tubular spar, for measuring the bending and distortion strains of the wings. The strain sensor data can then be input to theoretical displacement equations for calculations of slope, deflection, and twisting of the wing tubular spar at all strain-sensing stations, including the spar tip sensing station.

Because the accuracy of the displacement (bending and torsion) equations have been validated by the classical beam theory and finite-element analysis, the equations are ready for application. To solidify confidence, however, the accuracy of the displacement equations must be checked extensively by testing several types of continuous and composite cantilever tubular beams under bending, torsion, and combined bending and torsion. The validation experiments are presently being conducted.

When strain sensors are installed on the wing spar (or wing box), the displacement equations together with strain sensor data can be used to construct the in-flight deformed shape of an aircraft such as the Helios flying wing. Because they are lightweight, fiber optic sensors

may be the optimal choice for the embedded strain-sensing system on the wing spar surface.

The use of a conventional strain gage sensing system is impractical, because it has numerous lead wires that add weight, thus it is too heavy for the lightweight flying wing to carry.

CONCLUDING REMARKS

Displacement equations were developed for a cantilever wing tubular spar under bending, torsion, and combined bending and torsion loading. These displacement equations were expressed in terms of strains measured at multiple sensing stations equally spaced on the surface of the wing spar. The principal results are as follows:

1. The displacement equations developed for the uniform cantilever beam were successfully validated for accuracy by classical beam theory and finite-element analysis.

2. The deflections for the three types of cantilever tubular spars predicted from the deflection equations agreed quite well with those calculated from the finite-element analysis.

3. The deflection equations developed for the uniform cantilever beam were extended to predict, with adequate accuracy, the deformed shapes of a two-point supported uniform beam (simple beam).

4. By means of a multiple-line strain-sensing system, the deflection equations developed for simple beams can be applied to predict the deformed shapes of plates.

5. Deflection equations were also developed for tapered, slightly tapered, and stepwise tapered cantilever beams. These displacement equations were applied to predict the deflections and twist angles of a tapered cantilever wing box (for which two strain-sensing lines are required) with reasonable accuracy compared to the finite-element predictions.

6. The displacement equations and associated strain-sensing system (such as fiber optic sensors) create a powerful means for in-flight calculations of slopes, deflections, and cross-sectional twist angles of the wing spar at any strain-sensing station. These calculated displacements can be used to construct the deformed shape of the long-span flying wing. Ultimately, the calculated deformation data can be visually displayed for the ground-based pilot to monitor the in-flight deformed shape of the long-span flying wing.

ED01-0209-2

Figure 1. Solar powered Helios prototype flying wing during a test flight over the Pacific Ocean.

$$M(x) = M_{i-1} - \left(M_{i-1} - M_i\right) \frac{x - x_{i-1}}{\Delta l} \; ; \; x_{i-1} < x < x_i$$

060097
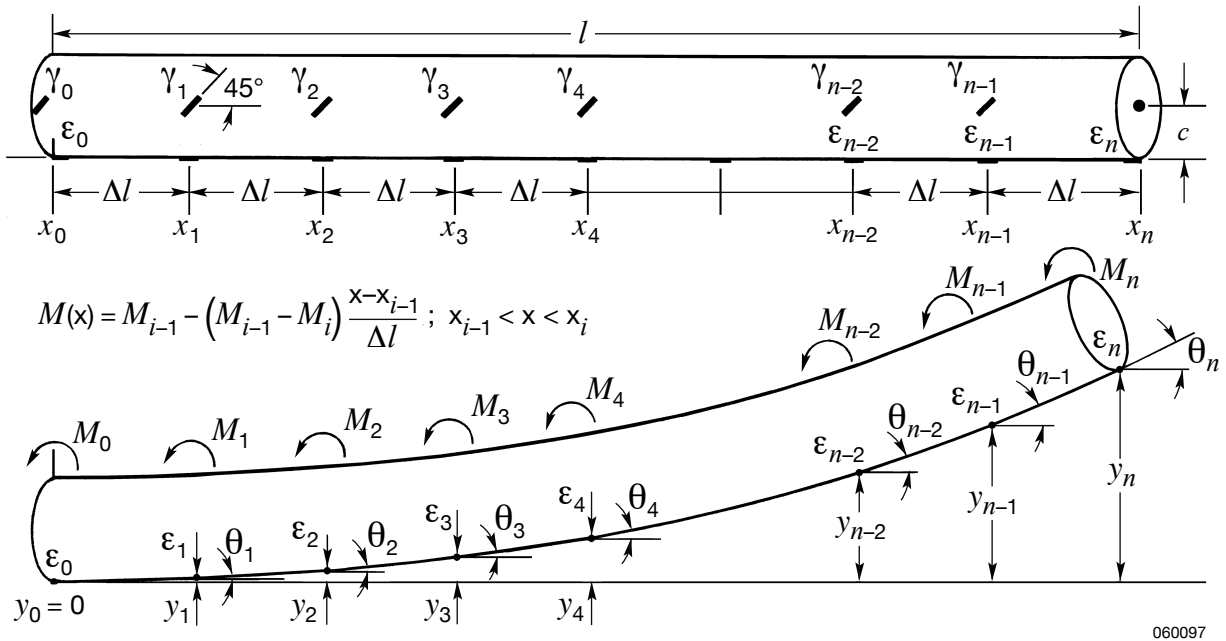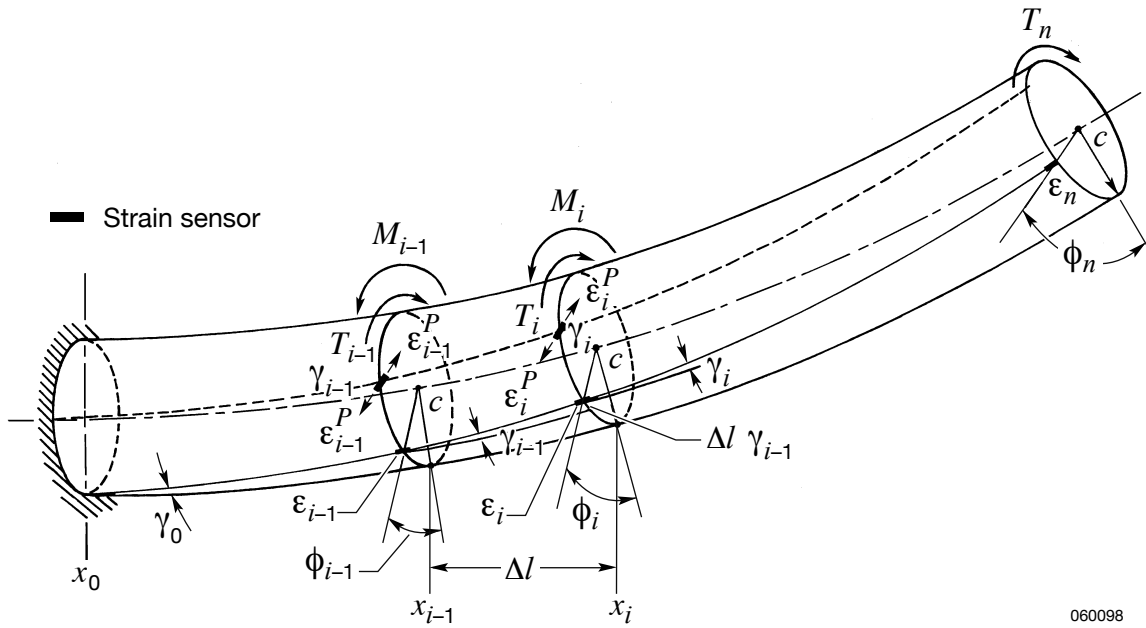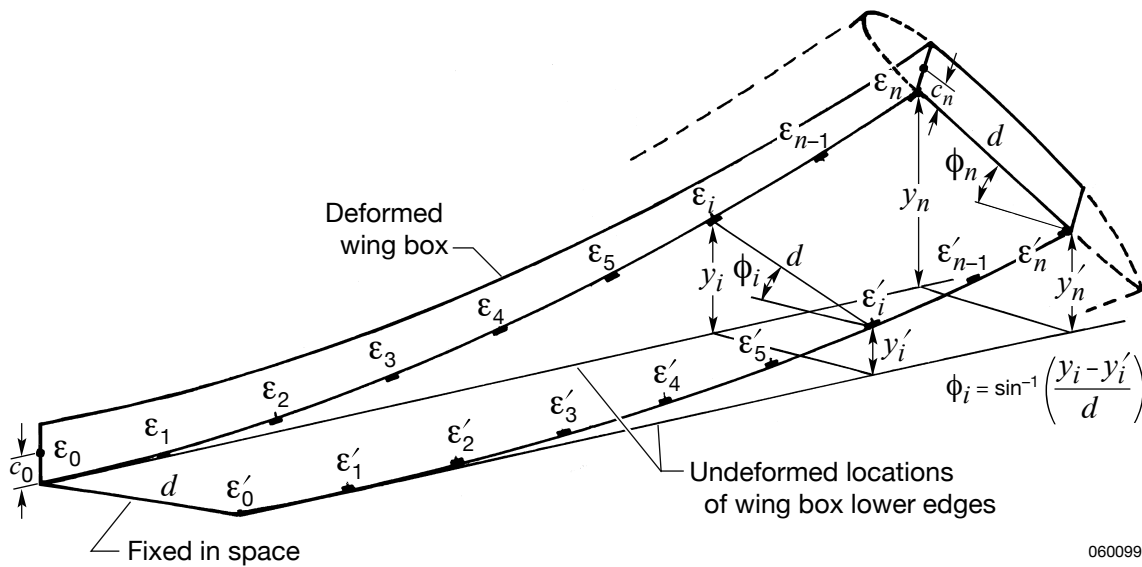
Figure 2. Cantilever tubular spar with equally spaced bending and torsion strain sensors.

Figure 3. Instrumented cantilever tubular spar under combined bending and torsion.

$$\phi_i = \sin^{-1}\left(\frac{y_i - y_i'}{d}\right)$$

Figure 4. Wing box instrumented with a two–parallel-line strain sensor system.
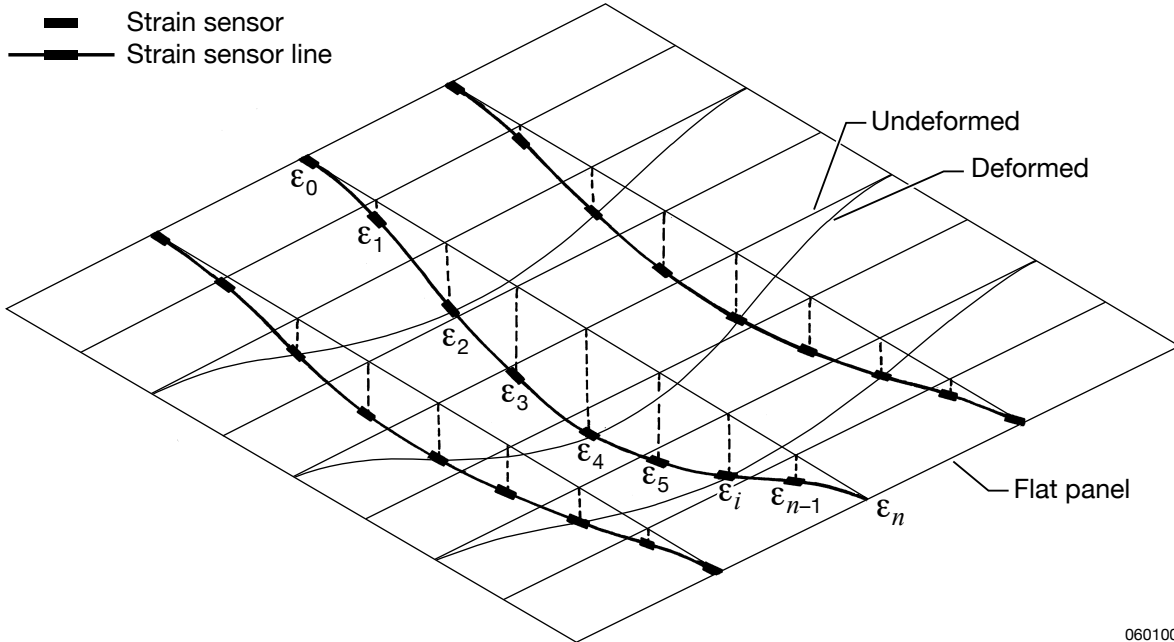
Figure 5. Flat panel instrumented with a multiple–parallel-line strain sensor system.
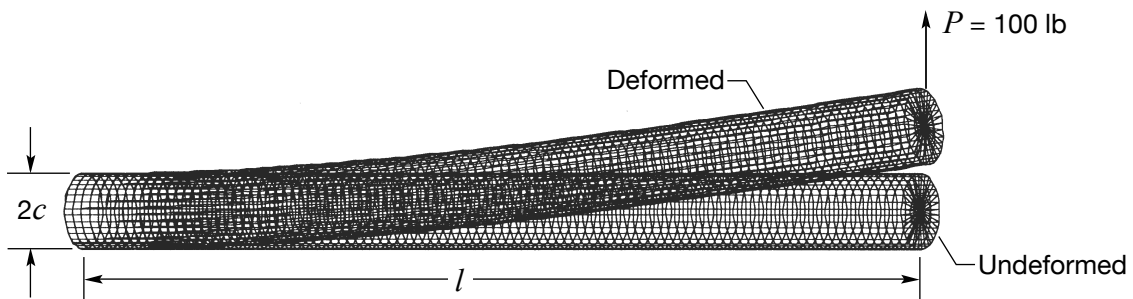
l = 100.5 in.

a = 4 in.   (Al, four-ply walls)

t = 0.02296 in. (Al, four-ply walls)

a = 4.07749 in. (Helios spar caps)

$\bar{t}$ = 0.17784 in. (Helios spar caps)

Nodes   3673

Four-node elements   3636

Three-node elements   36

Figure 6. Helios tubular spar finite-element model subjected to a vertical tip load of P = 100 lb.

47

l = 100 in.
w = 17 in.
$2c_0$ = 4 in.
$2c_n$ = 3 in.
t = 0.02296 in.
$c_i = c_0 - (c_0 - c_n)\,[(i\Delta l)/l]$

Nodes 3636
Four-node elements 3617

060102

Figure 7. Wing box finite-element model subjected to bending and torsion.
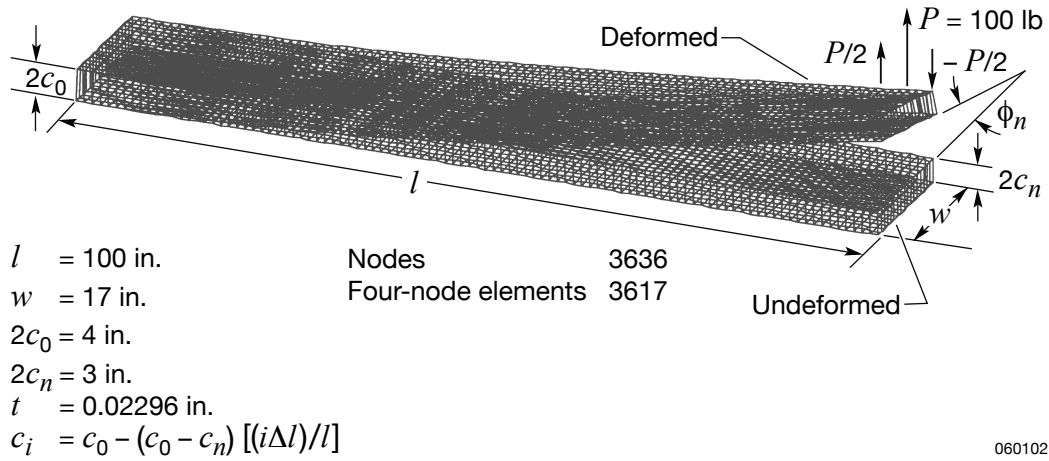

l = 100.5 in.
a = 4 in.
t = 0.02296 in.
$c = a + 0.5t$

Nodes 3673
Four-node elements 3636
Three-node elements 36

060103
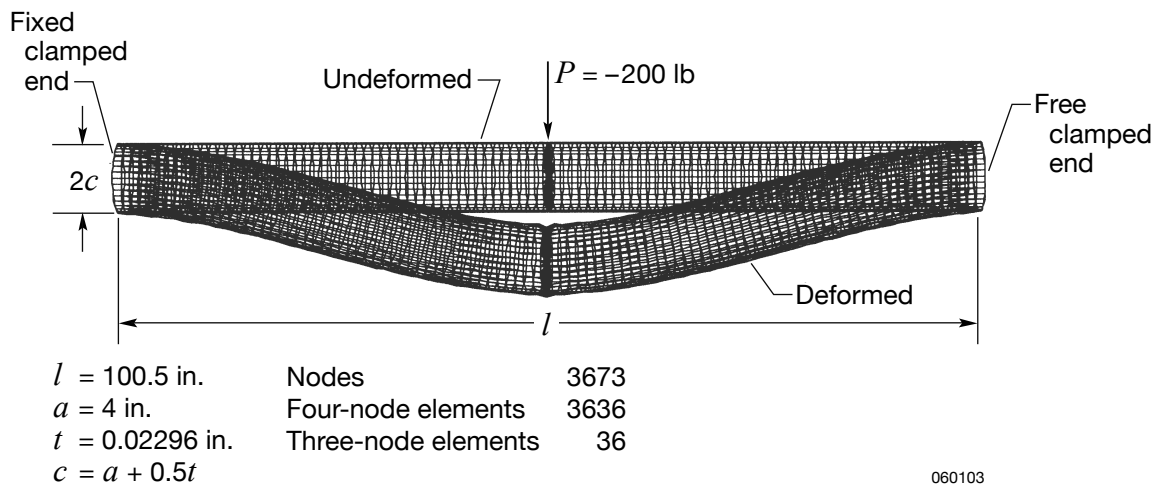
(a) Both ends clamped.

Figure 8. Finite-element model for an aluminum tubular beam subjected to a downward central vertical load of $P = -200$ lb.

Built-in
end

$P = -200$ lb

Undeformed

Free simply
supported
end

$2c$

Deformed

l

l = 100.5 in.   Nodes   3673
a = 4 in.   Four-node elements   3636
t = 0.02296 in.   Three-node elements   36
$c = a + 0.5t$

060104

(b) Left end clamped and right end simply supported.

Fixed simply
supported end

Undeformed

$P = -200$ lb

Free simply
supported
end

$2c$

Deformed

l

l = 100.5 in.   Nodes   3673
a = 4 in.   Four-node elements   3636
t = 0.02296 in.   Three-node elements   36
$c = a + 0.5t$

060105
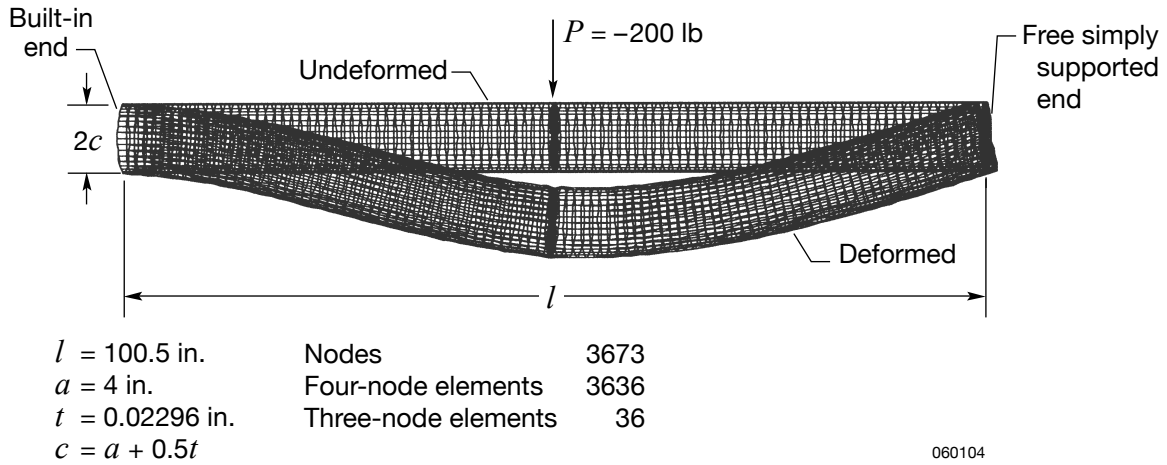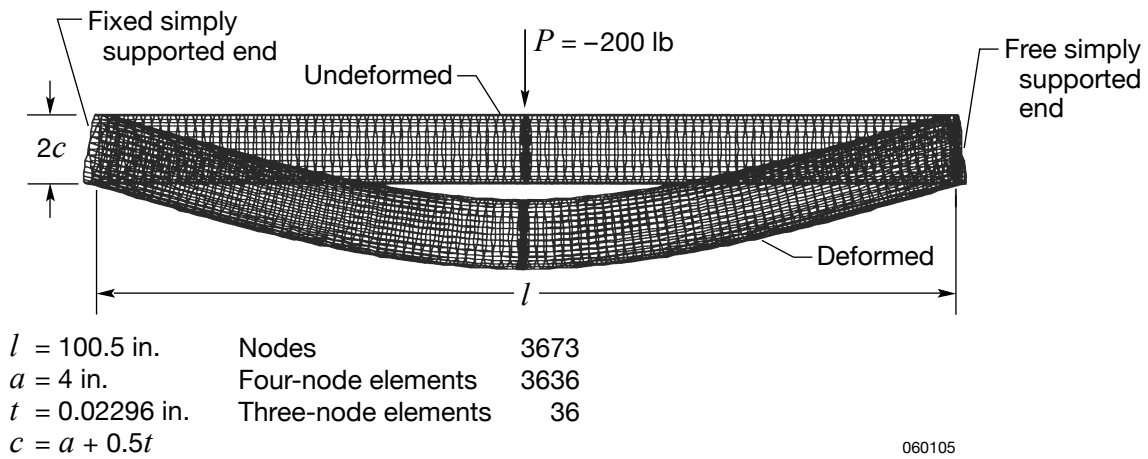
(c) Both ends simply supported.

Figure 8. Concluded.

49

l = 24 in.   Nodes   1250
w = 24 in.   Four-node elements   2356
h = 0.2 in.
c = $h/2$ = 0.1 in.

060106

(a) Four edges clamped.

l = 24 in.   Nodes   1299
w = 24 in.   Four-node elements   2356
h = 0.2 in.   Two-node elements   98
c = $h/2$ = 0.1 in.

060107
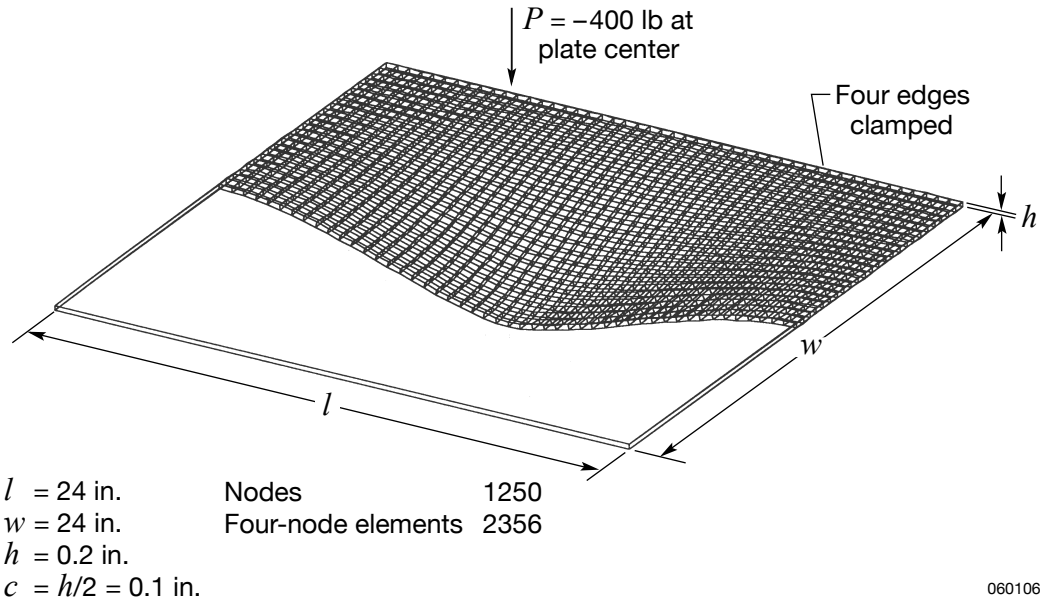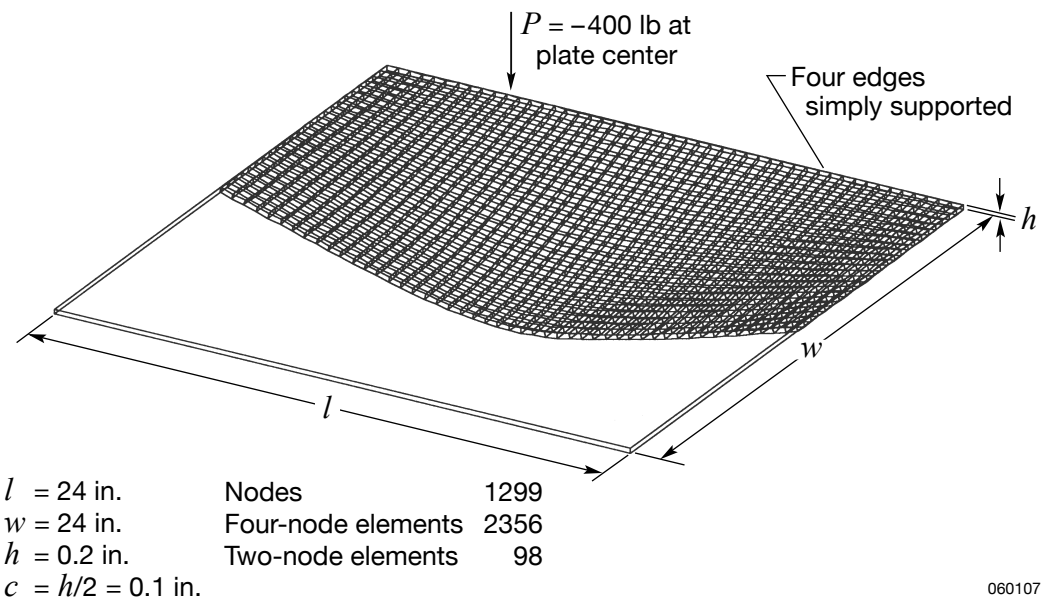
(b) Four edges simply supported.

Figure 9. Quarter panel finite-element model (with mirror image) for a square plate subjected to a downward central vertical load of $P = -400$ lb.

50

Figure 10. Bending strains, ε_i, at different strain-sensing stations, x_i, calculated from the SPAR program; aluminum cantilever tube; $n = 8$; $P = 100$ lb.
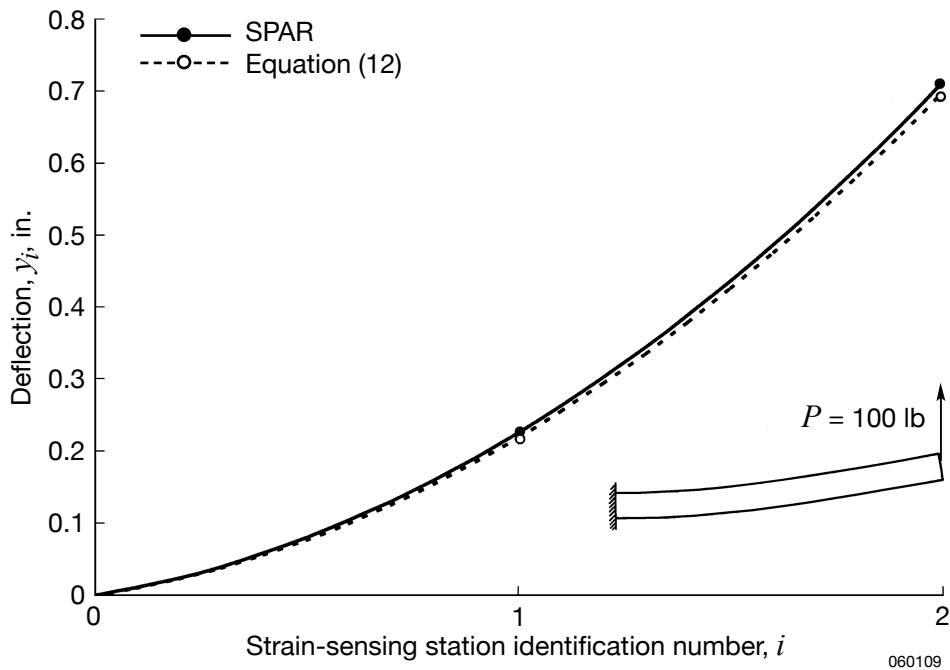
(a) $n = 2$; $P = 100$ lb.

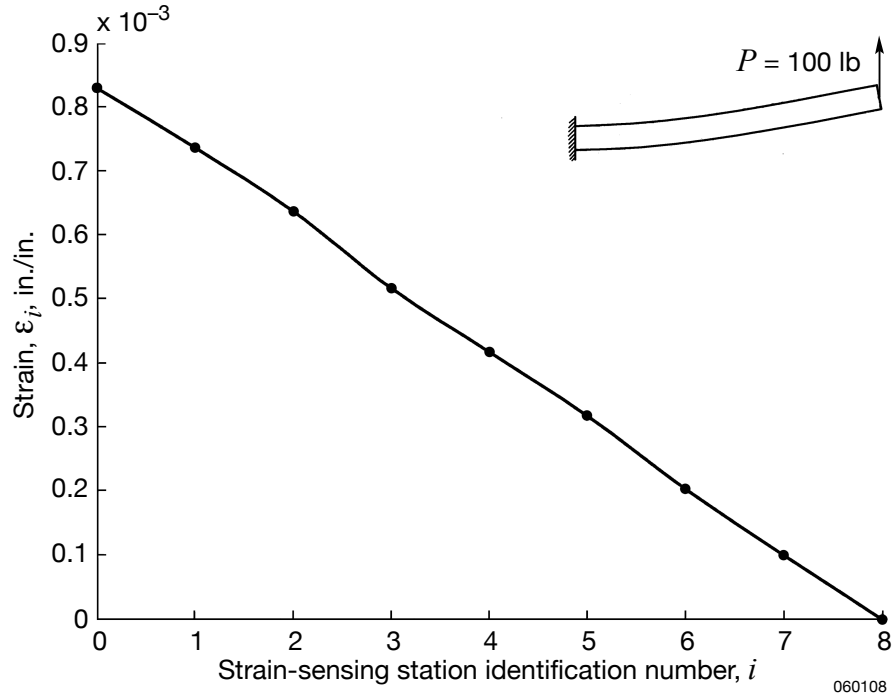Figure 11. Comparison of deflections calculated from SPAR with those calculated from deflection equation (12); aluminum cantilever tube.
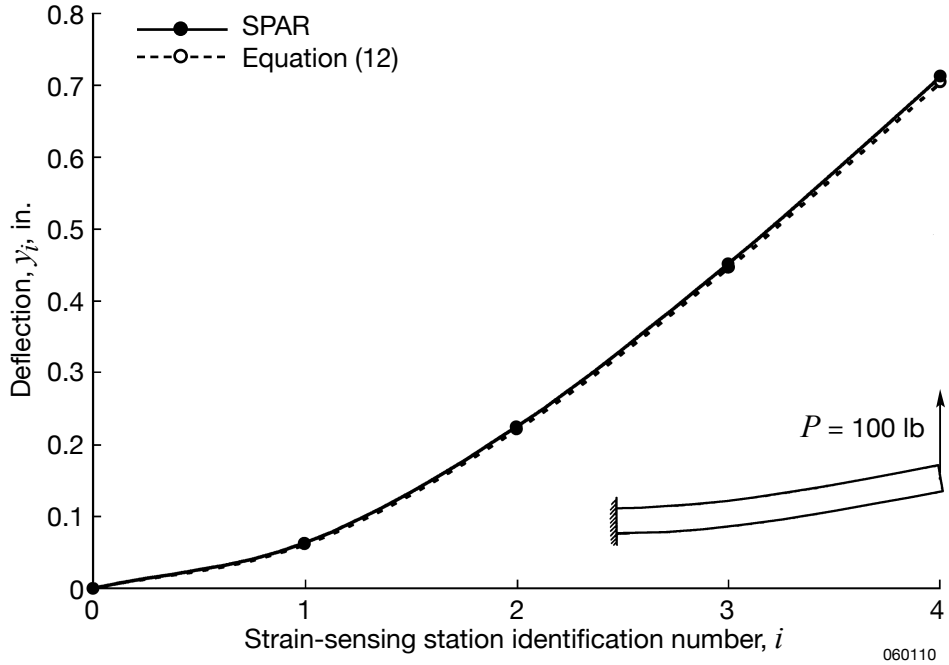
(b) $n = 4$; $P = 100$ lb.

(c) $n = 8$; $P = 100$ lb.

Figure 11. Concluded.
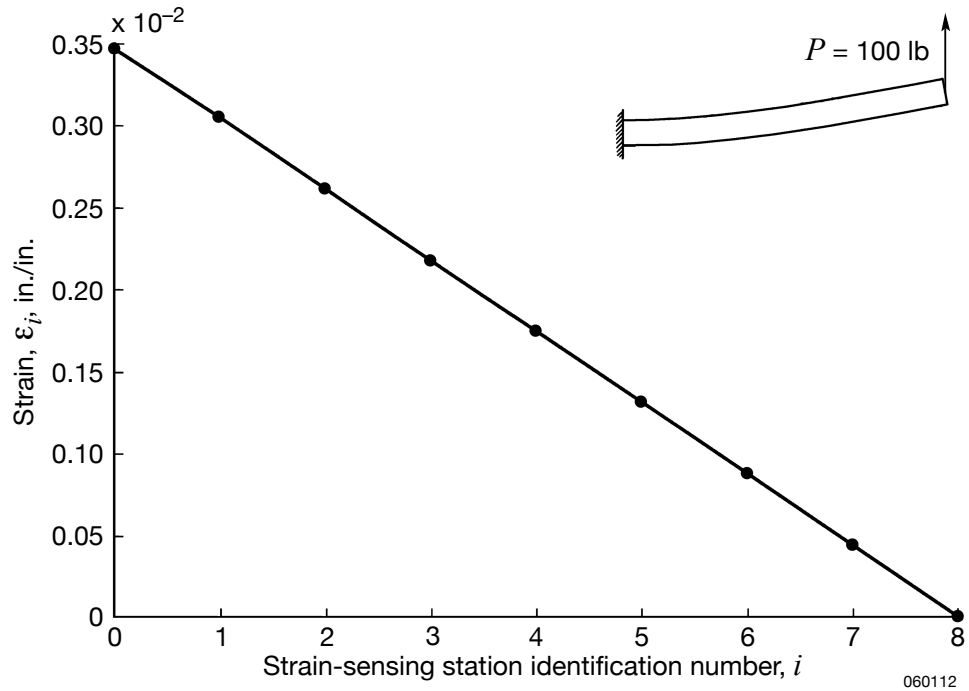
Figure 12. Bending strains, ε_i, at different sensing stations, x_i, calculated from the SPAR program; four-ply composite cantilever tube; $n = 8$; $P = 100$ lb.
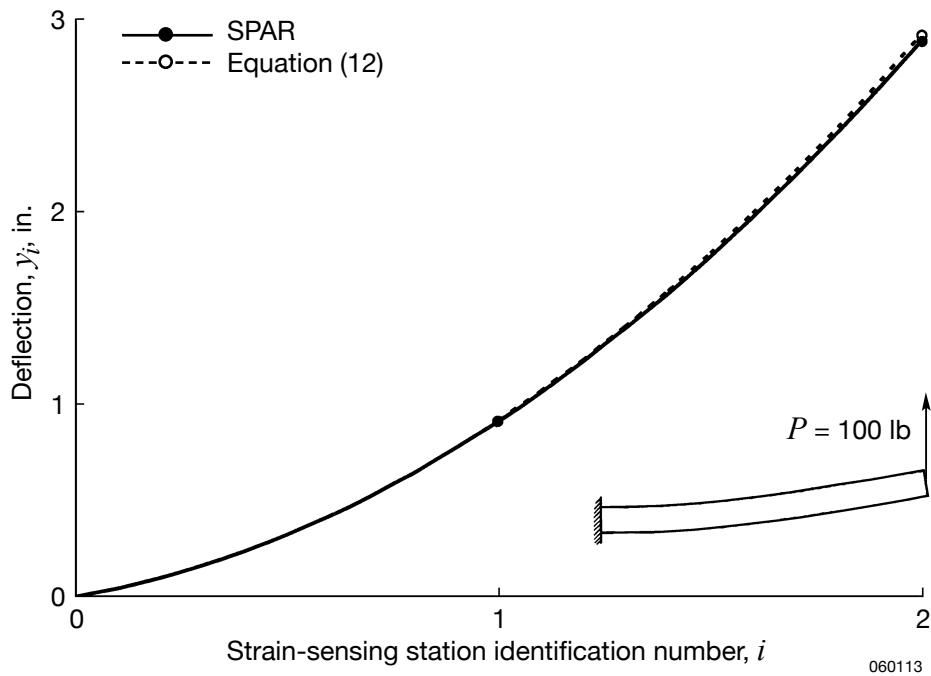
(a) $n = 2$; $P = 100$ lb.

Figure 13. Comparison of deflections calculated from SPAR with those calculated from deflection equation (12); four-ply composite cantilever tube.
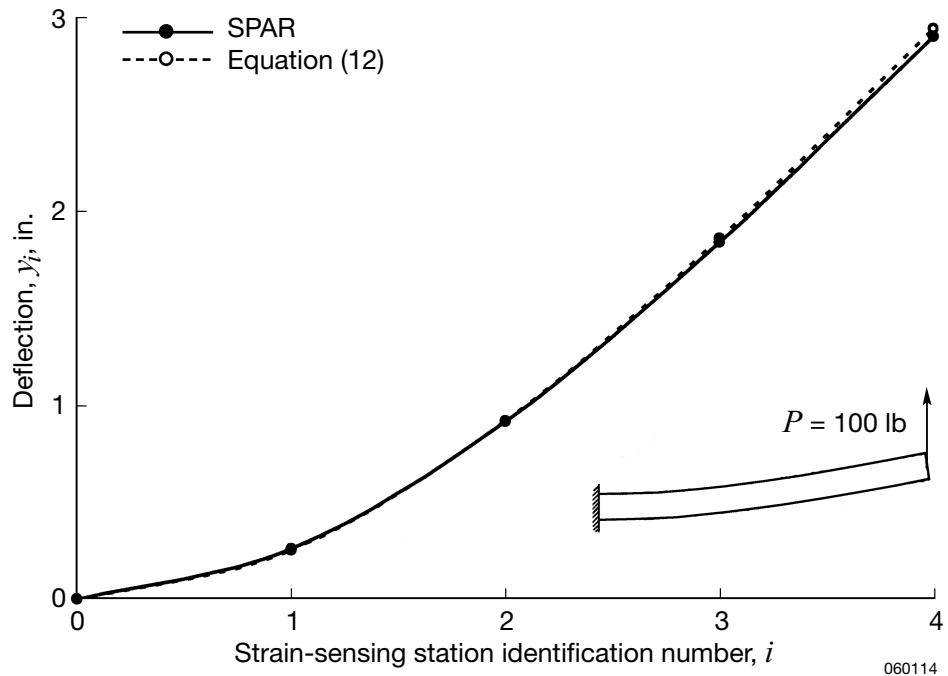
(b) $n = 4$; $P = 100$ lb.
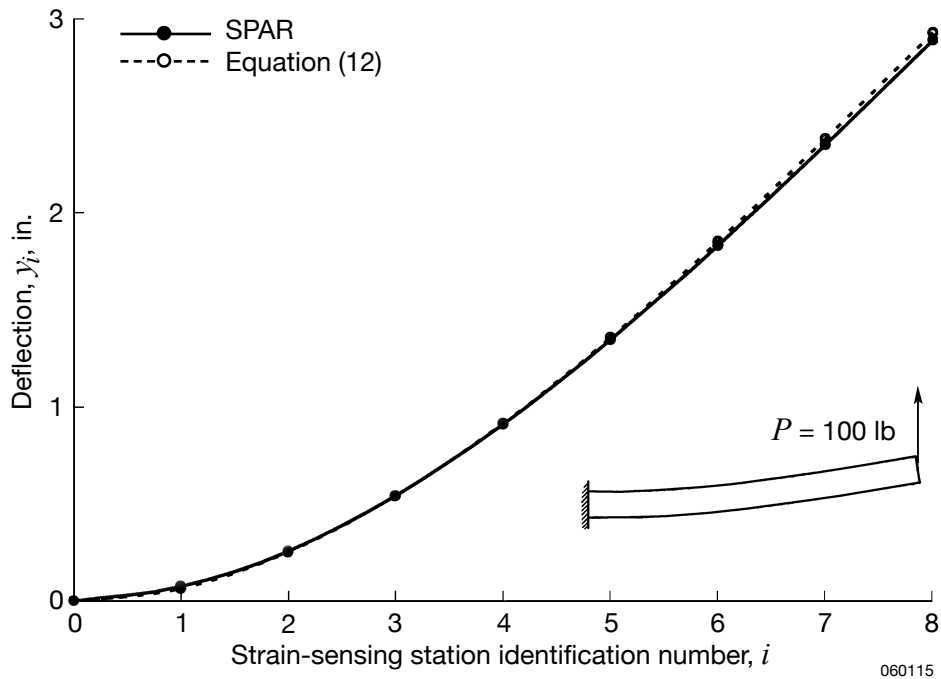
(c) $n = 8$; $P = 100$ lb.

Figure 13. Concluded.
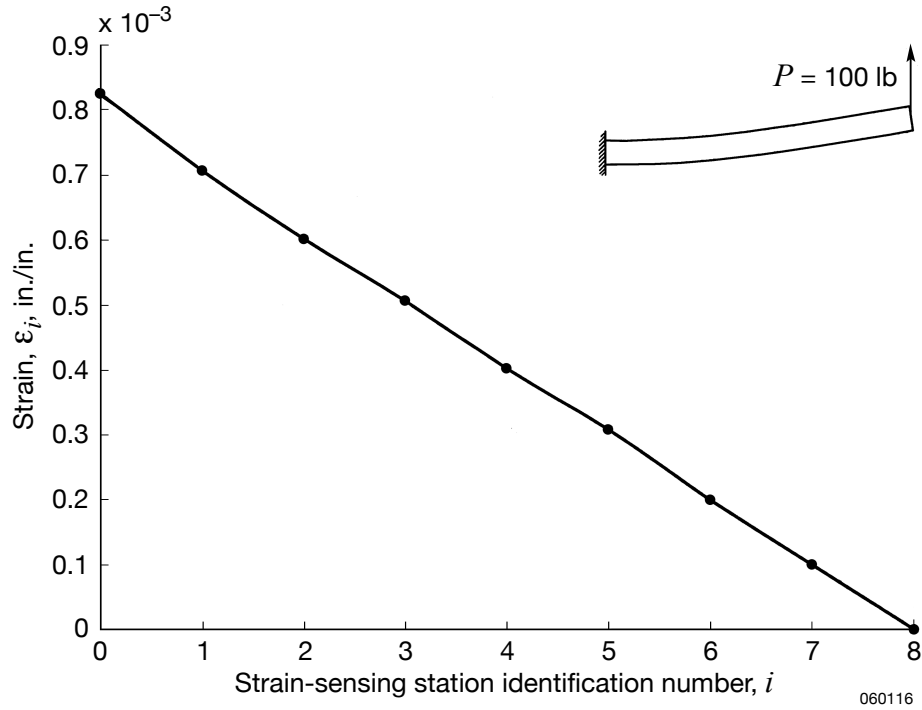
Figure 14. Bending strains, ε_i, at different sensing stations, x_i, calculated from the SPAR program; Helios composite cantilever tube; $n = 8$; $P = 100$ lb.
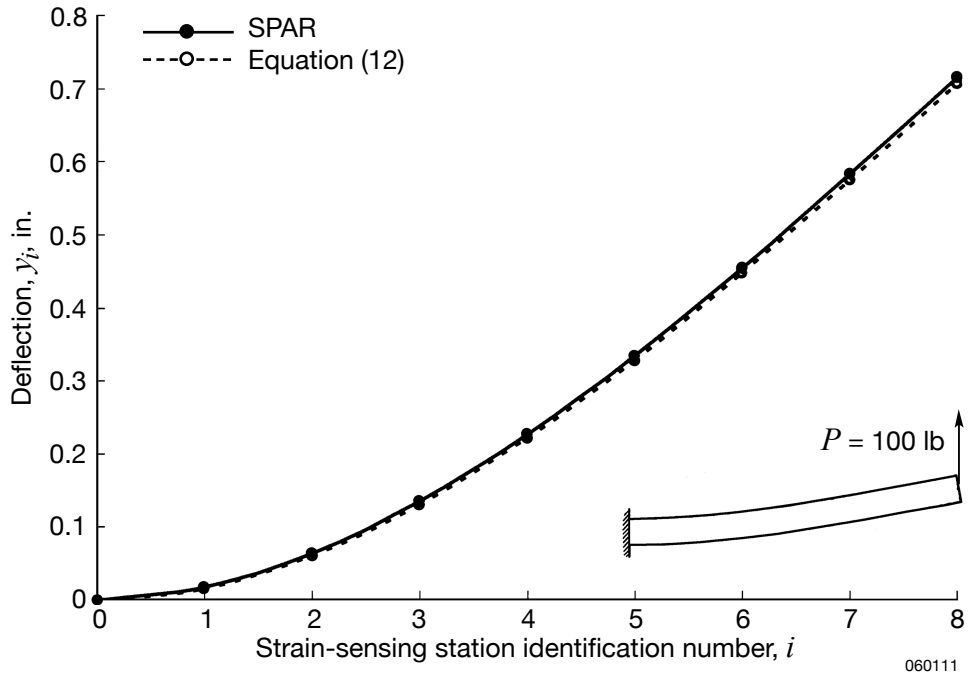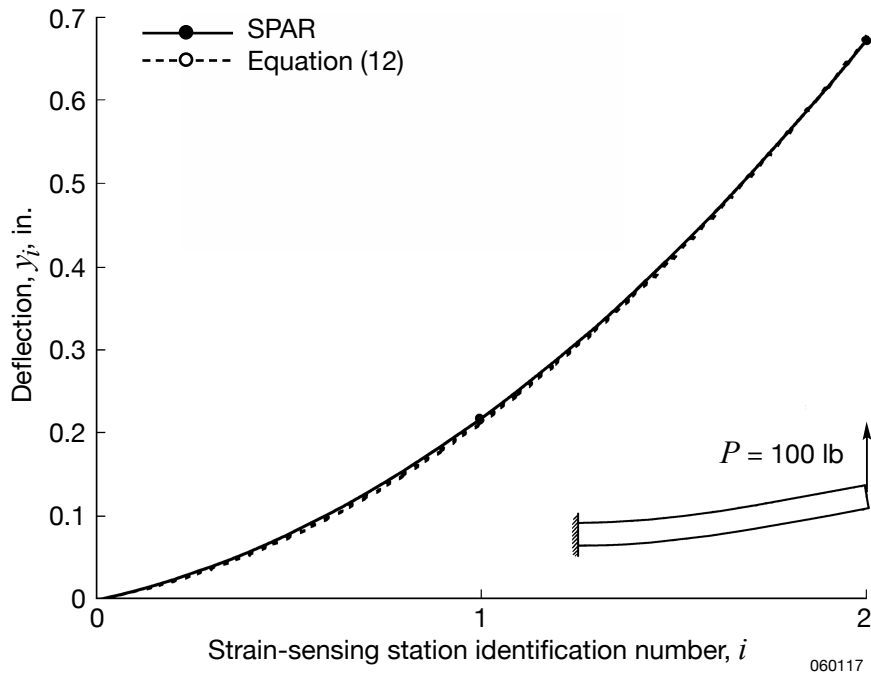

(a) $n = 2$; $P = 100$ lb.

Figure 15. Comparison of deflections calculated from SPAR with those calculated from deflection equation (12); Helios composite cantilever tube.

55
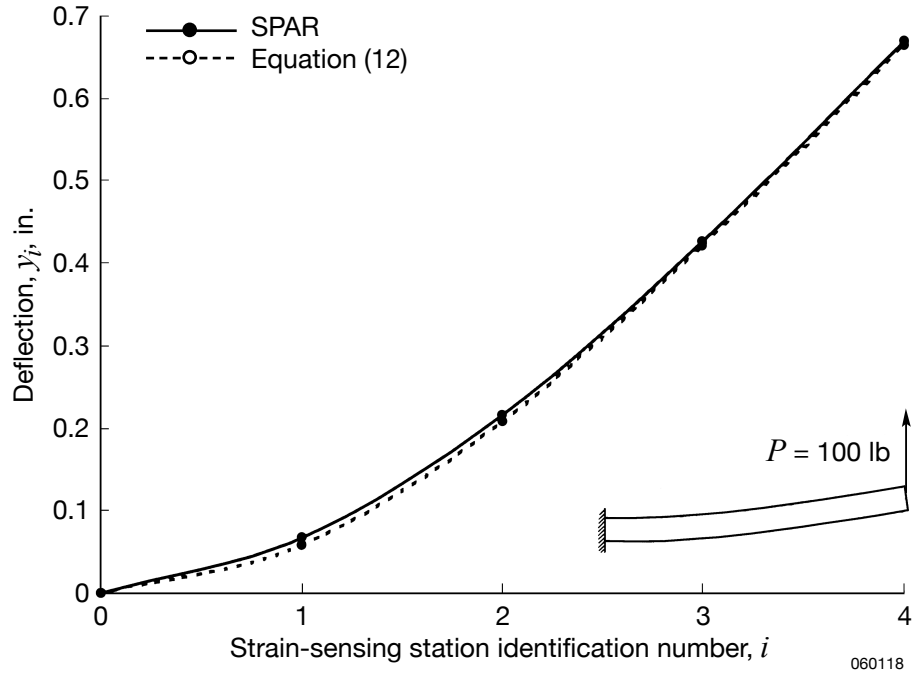
(b) $n = 4$; $P = 100$ lb.

(c) $n = 8$; $P = 100$ lb.

Figure 15. Concluded.
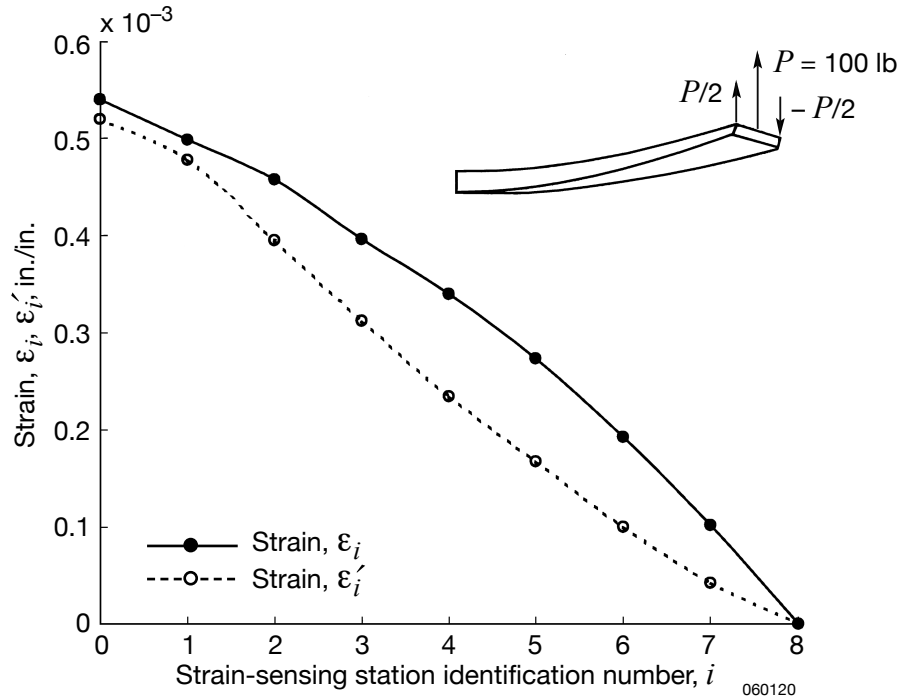
Figure 16. Front and rear bending strains, $\{\varepsilon_i, \varepsilon_i'\}$, at different span-wise locations, x_i, calculated from the SPAR program; tapered cantilever wing box; $n = 8$; $P = 100$ lb; $T = 50 \times 17$ in-lb.
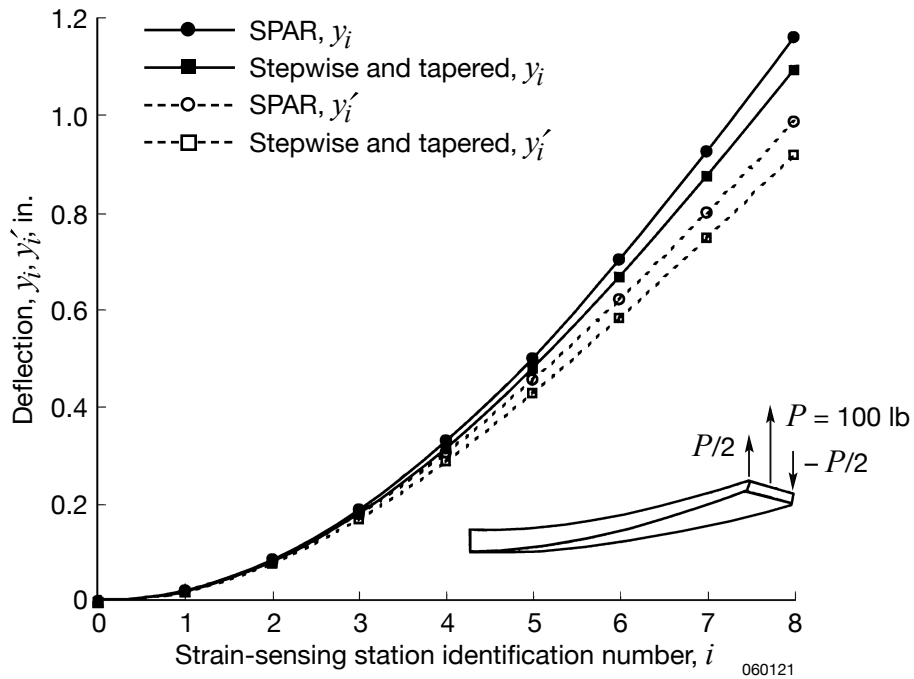
Figure 17. Comparison of front and rear deflections, $\{y_i, y_i'\}$, calculated from SPAR with those calculated from deflection equations (35) (stepwise) and (30) (tapered); tapered cantilever wing box; $n = 8$; $P = 100$ lb; $T = 50 \times 17$ in-lb.
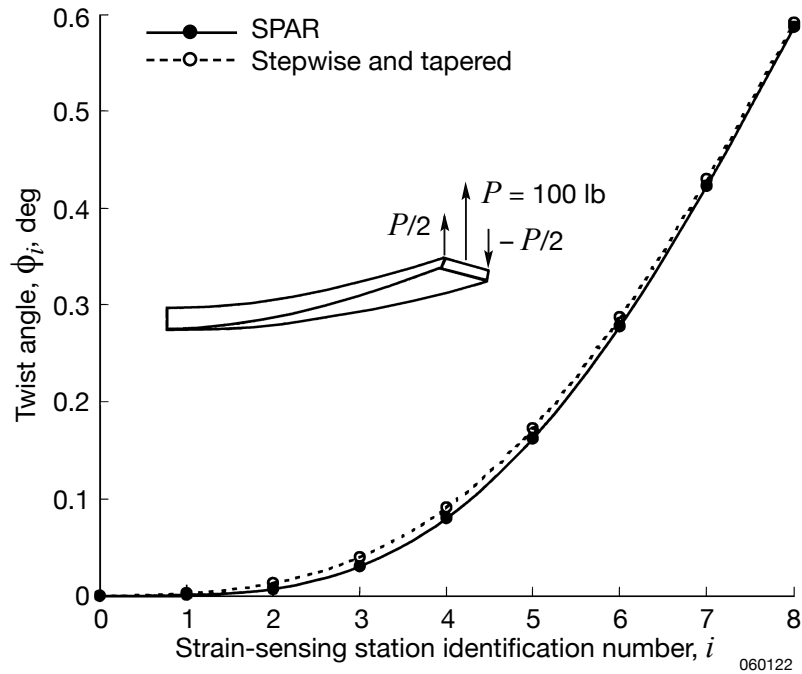
Figure 18. Comparison of twist angles, ϕ_i , calculated from equation (36) using the SPAR program and deflections calculated from equations (35) (stepwise) and (30) (tapered); tapered cantilever wing box; $n = 8$; $P = 100$ lb; $T = 50 \times 17$ in-lb.
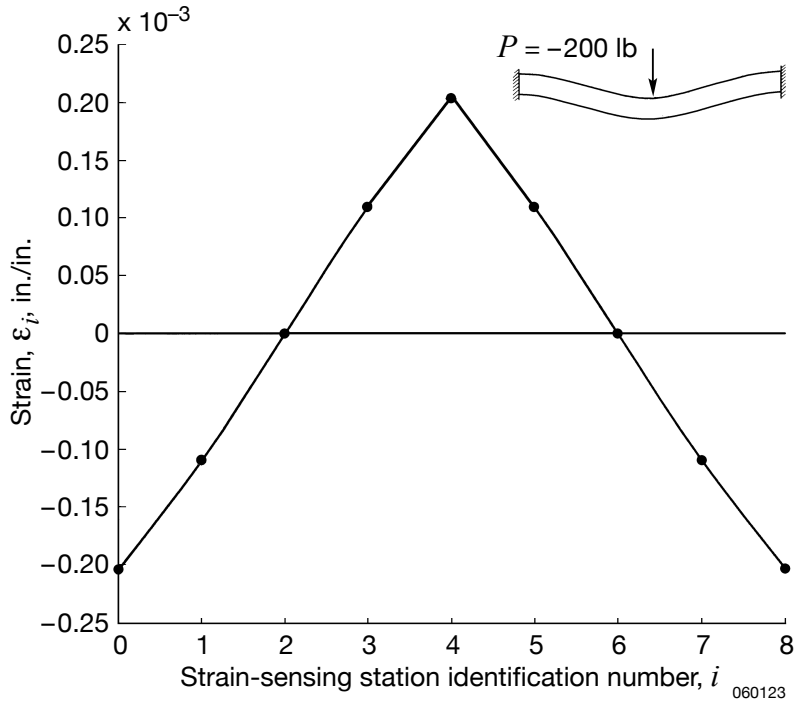
Figure 19. Bending strains, ε_i, at different sensing stations, x_i, calculated from the SPAR program; two-point supported beam with both ends clamped; $n = 8$; $P = -200$ lb.
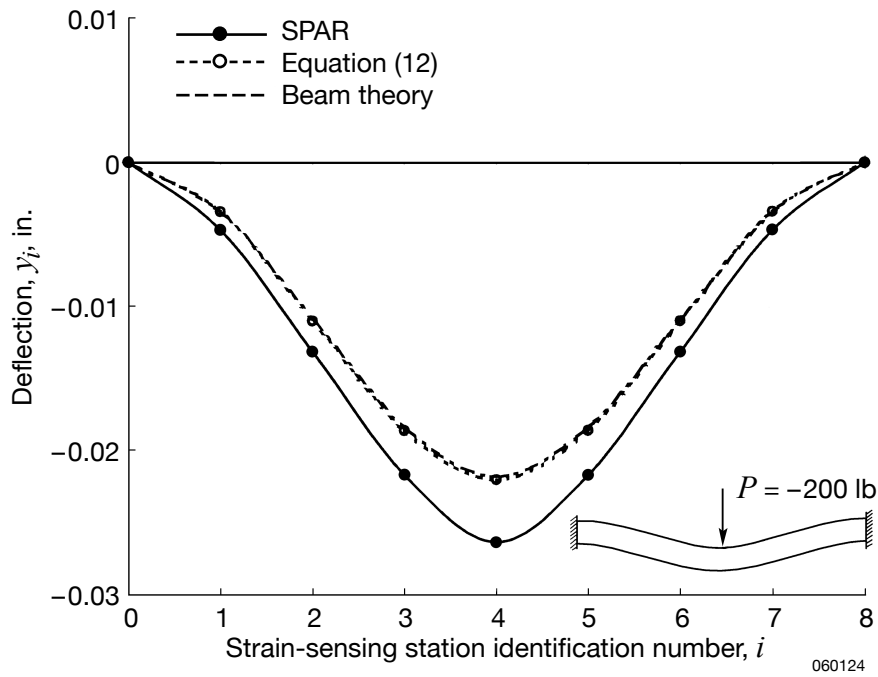
Figure 20. Comparison of deflections calculated from the SPAR program, deflection equation (12), and classical beam theory; two-point supported beam with both ends clamped; $n = 8$; $P = -200$ lb.

59
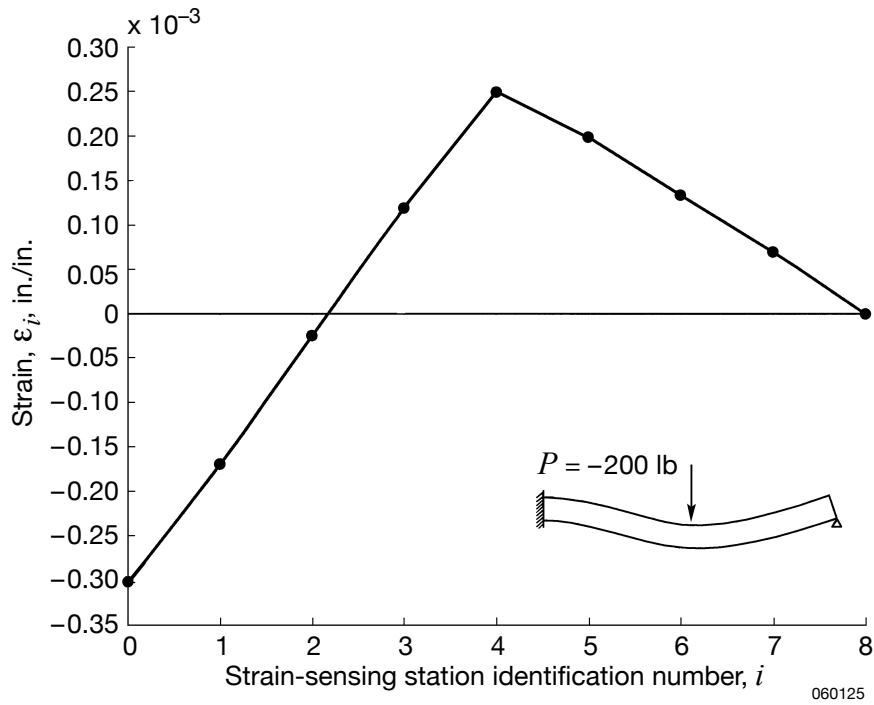
Figure 21. Bending strains, ε_i , at different sensing stations, x_i , calculated from the SPAR program; two-point supported beam with a clamped left end and simply supported right end; $n = 8$; $P = -200$ lb.
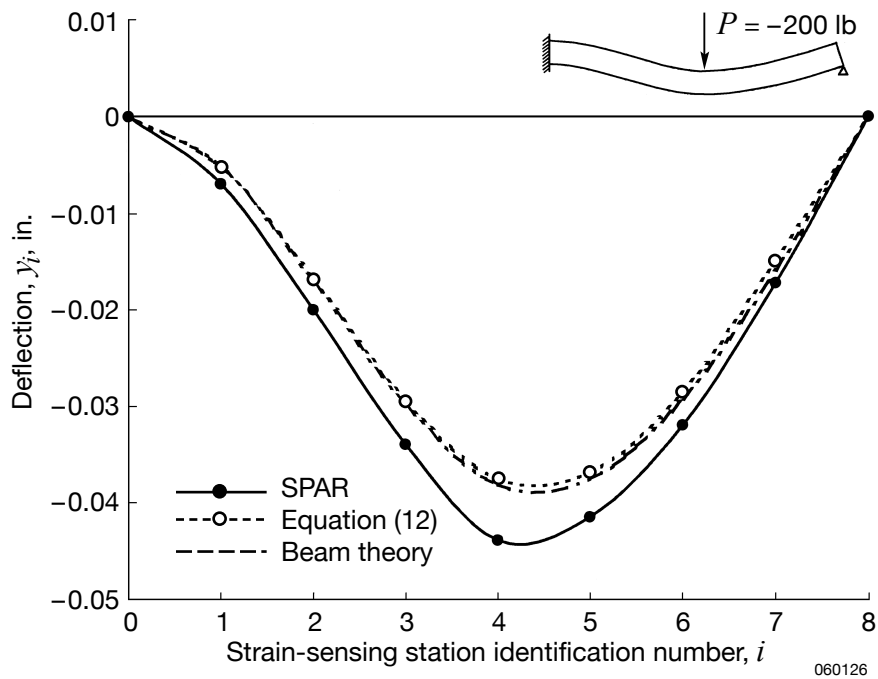
Figure 22. Comparison of deflections calculated from the SPAR program, deflection equation (12), and classical beam theory; two-point supported beam with a clamped left end and simply supported right end; $n = 8$; $P = -200$ lb.

60
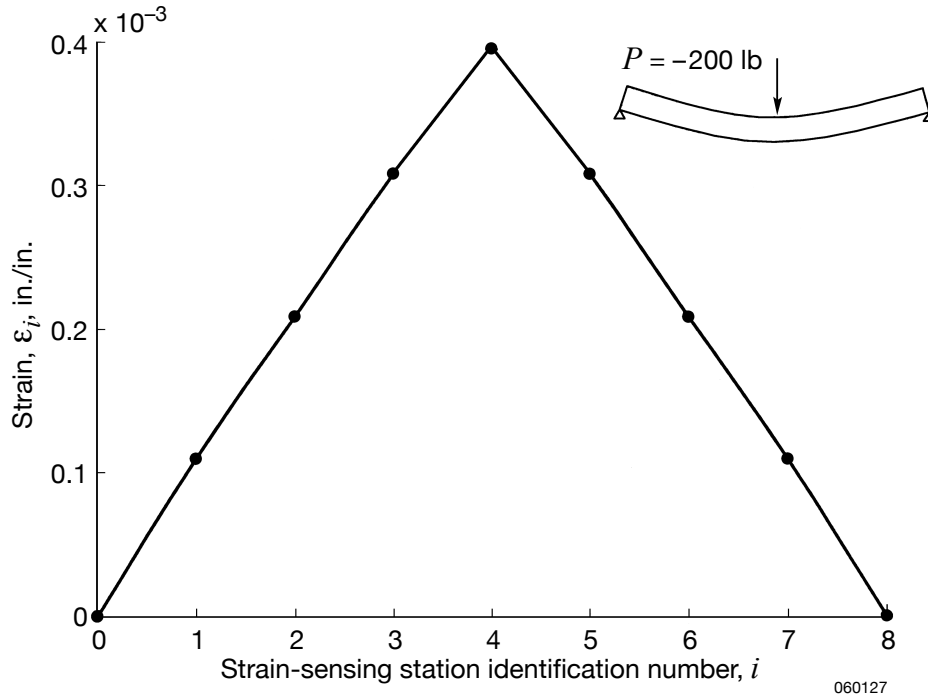
Figure 23.   Bending strains, ε_i, at different sensing stations, x_i, calculated from the SPAR program; two-point supported beam with both ends simply supported; $n = 8$; $P = -200$ lb.
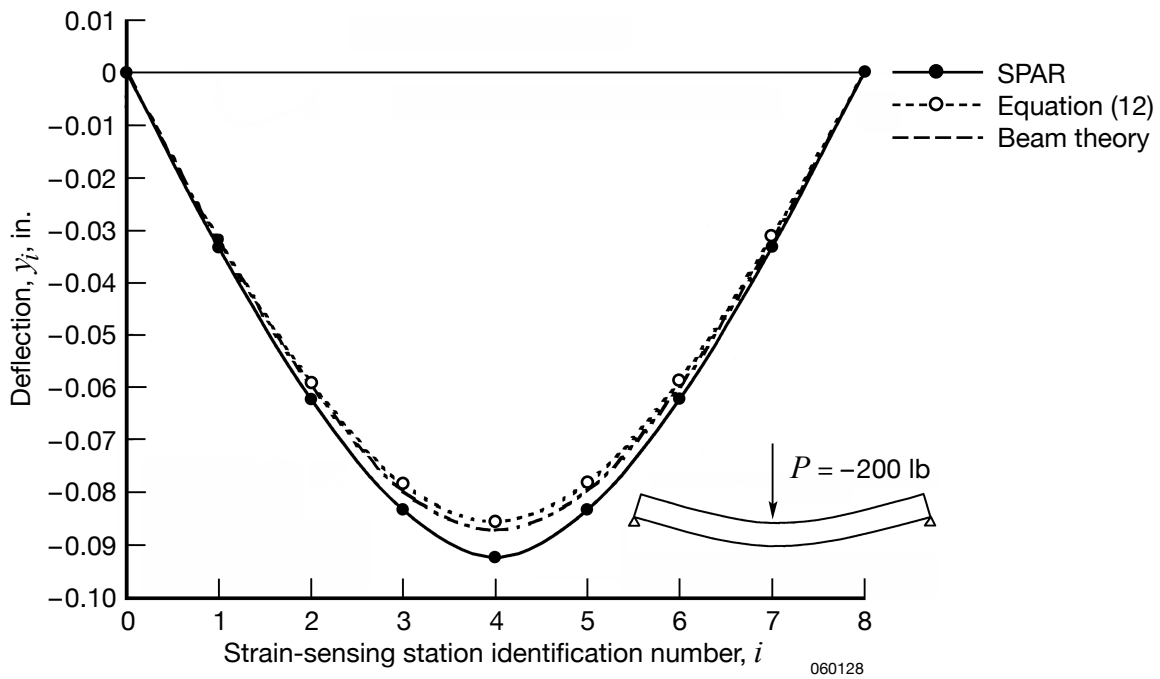
Figure 24.   Comparison of deflections calculated from the SPAR program, deflection equation (43), and classical beam theory; two-point supported beam with both ends simply supported; $n = 8$; $P = -200$ lb.
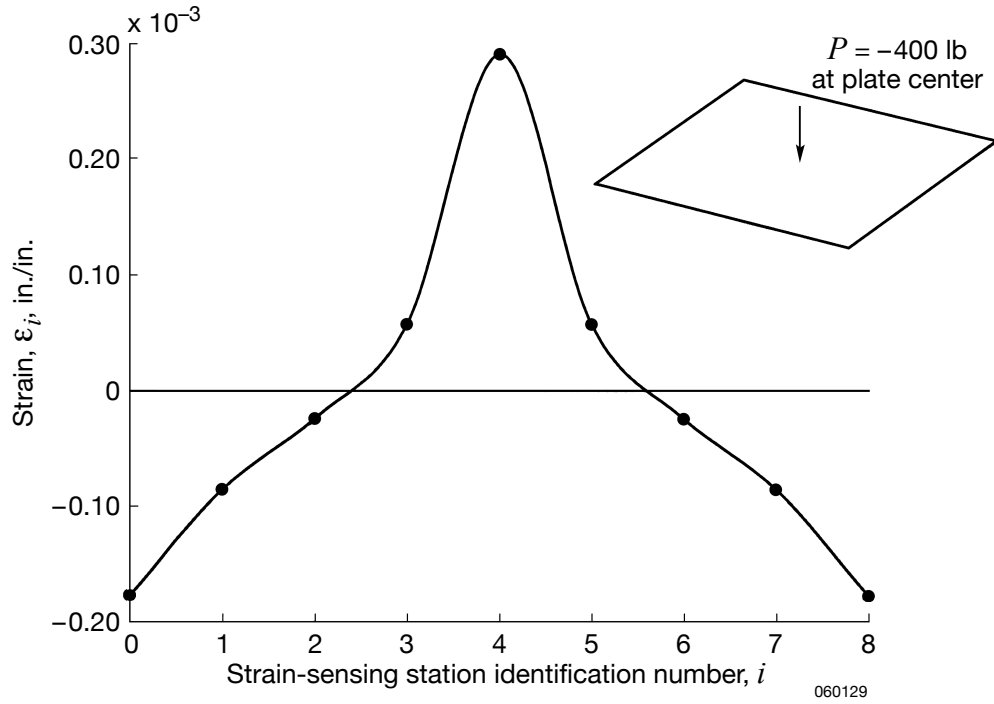
Figure 25. Bending strains, ε_i, at different sensing stations, x_i, calculated from the SPAR program; square plate with four edges clamped; $n = 8$; $P = -400$ lb.
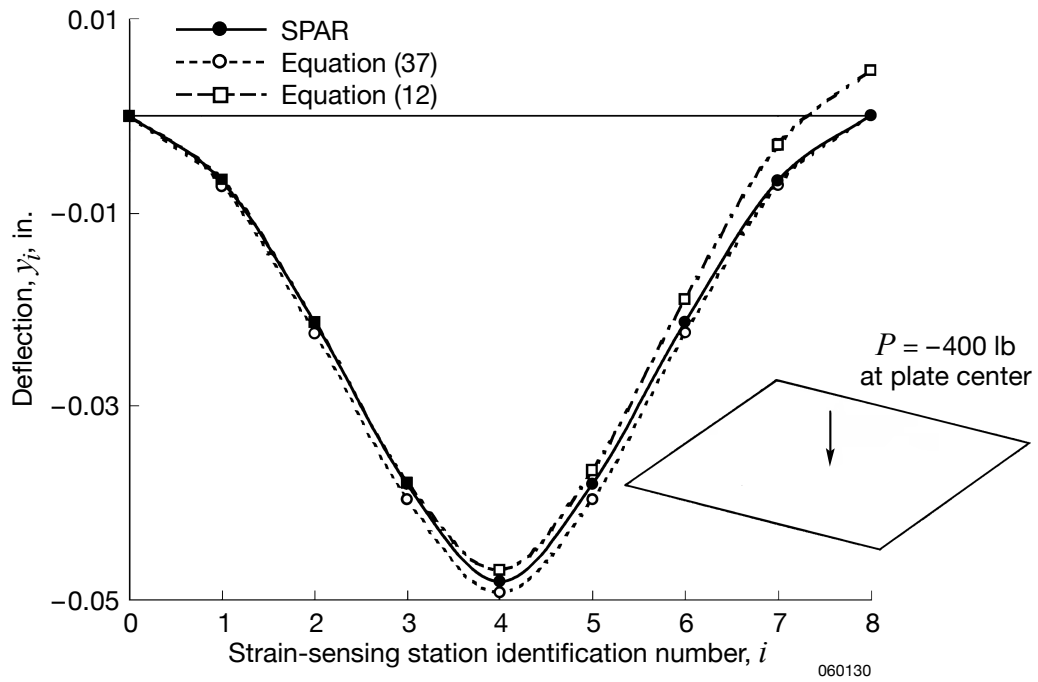
Figure 26. Comparison of deflections calculated from the SPAR program, equation (37), and deflection equation (12); square plate with four edges clamped; $n = 8$; $P = -400$ lb.
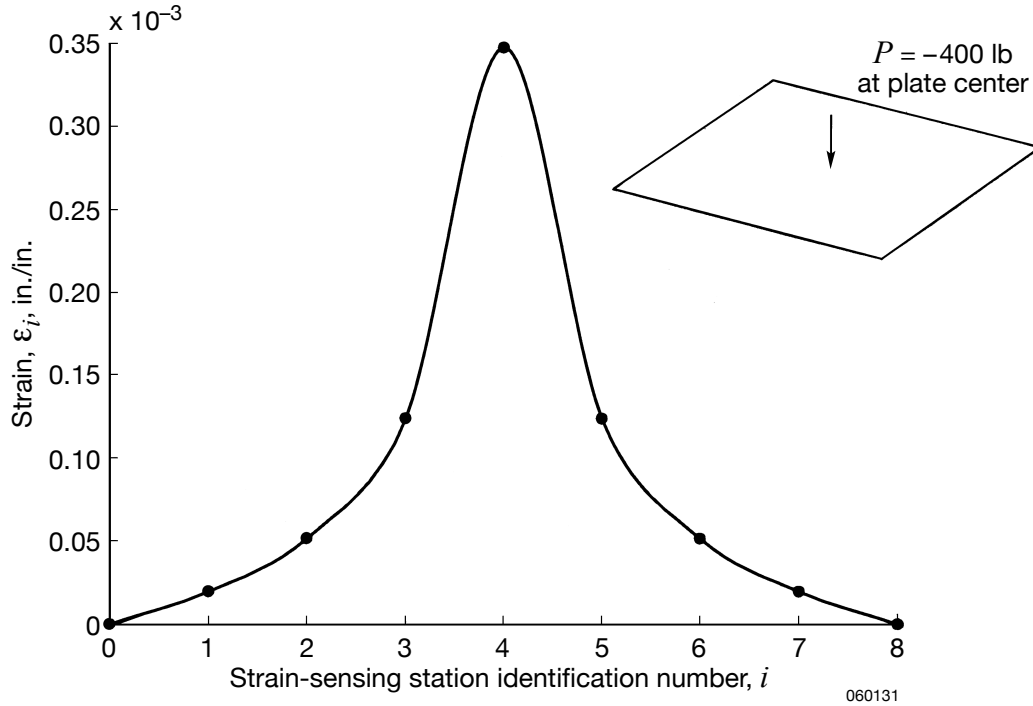
Figure 27. Bending strains, ε_i, at different strain-sensing stations, x_i, calculated from the SPAR program; square plate with four edges simply supported; $n = 8$; $P = -400$ lb.
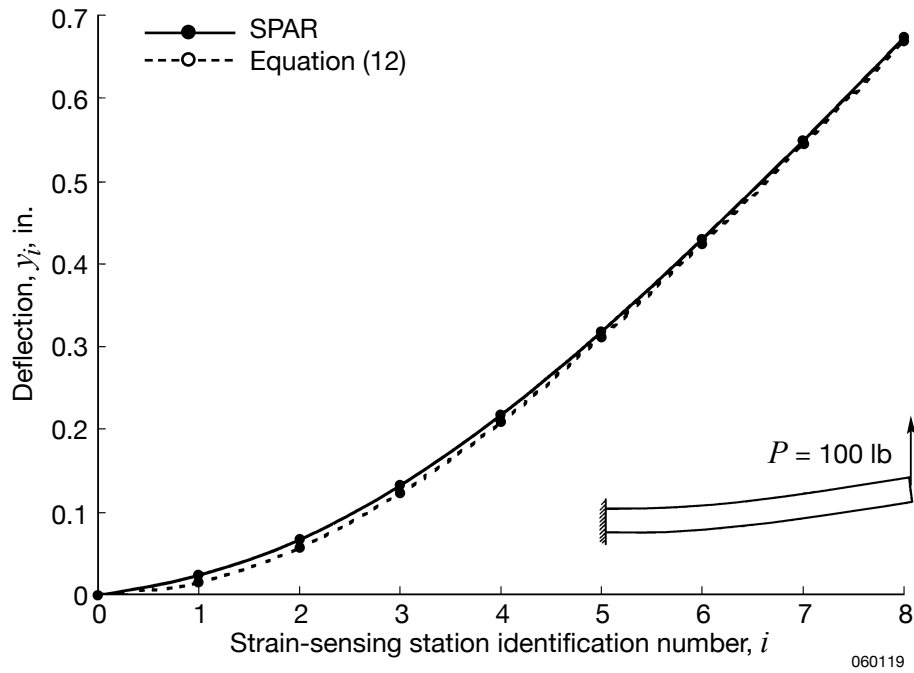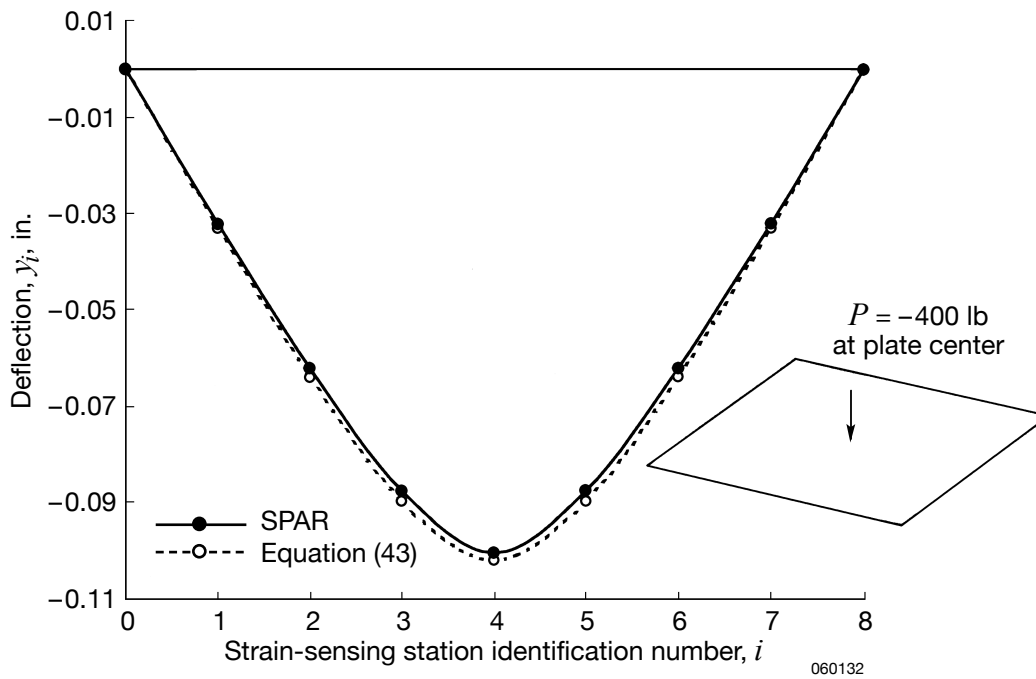

Figure 28. Comparison of deflections calculated from SPAR with those calculated from deflection equation (43); square plate with four edges simply supported; $n = 8$; $P = -400$ lb.

63

APPENDIX A
HELIOS FLYING WING

The Helios prototype (fig. 1) is an ultralightweight, unmanned, solar-powered flying wing aircraft (1,600 lb) designed to fly at altitudes up to 100,000 ft. The Helios wing has 14 electric motors (2 hp each) that drive 79-in.-diameter composite propellers. The current necessary to power these motors and other systems is generated by high efficiency solar cells spread over the upper surface of the wing. The cruising speed of the Helios is in the range of 19 to 27 mi/h.

The Helios wing has a chord length of 8 in. uniform over a 247-ft wingspan. The Helios wingspan is longer than the wingspan of the U.S. Air Force C-5 military transport (Lockheed Martin Aeronautics Company, Marietta, Georgia), which is 222 ft, and that of the Boeing 747 commercial jetliner (Boeing Company, Seattle, Washington), which ranges from 195 to 215 ft depending on the model. The Helios wing has an area of 1,976 ft^2 and a maximum wing loading of 0.81 lb/ft^2.

The wing thickness is 11.5 in. from tip to tip, without taper or sweep. The outer wing panels have built-in 10-deg dihedral. The Helios is constructed of mostly composite materials such as carbon fiber, graphite epoxy, Kevlar® (E.I. duPont de Nemours and Company, Wilmington, Delaware), Styrofoam® (Dow Chemical Company, Midland, Michigan), and a thin, transparent plastic skin. The main tubular wing spar is fabricated with four plies (45/-45/-45/45) of carbon fiber composite. To increase bending stiffness, an additional 27 plies ($0_8/90/0_8/90/0_9$) of carbon fiber composite were added in the 60-deg regions of the top and bottom of the spar. The spar is wrapped with Kevlar and Nomex® (E.I. duPont de Nemours and Company, Wilmington, Delaware) for additional strength. The wing ribs are made of epoxy and carbon fiber. Shaped Styrofoam is used for the leading edge of the wing, and a durable clear plastic film covers the entire wing.

APPENDIX B
INTEGRATIONS OF SLOPE AND DEFLECTION EQUATIONS FOR UNIFORM BEAMS

This section explains the details of the integrations of slope equation (6) and deflection equation (9) for uniform beams. These details provide the steps that result in the final mathematical forms given by equations (7) and (10), respectively.

Slope Equations

The slope, $\tan\theta(x)$, of the uniform beam in the region, $x_{i-1} \le x \le x_i$, between the two adjacent strain-sensing stations, $\{x_{i-1}, x_i\}$, can be obtained by integrating equation (3) with the constant of integration determined by enforcing the continuity of slope at the inboard adjacent strain-sensing station, x_{i-1}, as

$$\tan\theta(x) = \underbrace{\int_{x_{i-1}}^{x} \frac{d^2 y}{dx^2} dx}_{\text{Slope increment}} + \underbrace{\tan\theta_{i-1}}_{\text{Slope at } x_{i-1}} = \int_{x_{i-1}}^{x} \frac{\varepsilon(x)}{c} dx + \tan\theta_{i-1} \quad ; \quad x_{i-1} \le x \le x_i \tag{B-1}$$

The strain, $\varepsilon(x)$, in the region, $x_{i-1} \le x \le x_i$, between the two adjacent strain-sensing stations, $\{x_{i-1}, x_i\}$, is assumed to be a linear function as

$$\varepsilon(x) = \varepsilon_{i-1} - (\varepsilon_{i-1} - \varepsilon_i) \frac{x - x_{i-1}}{\Delta l} \tag{B-2}$$

Substitute equation (B-2) into equation (B-1), and carry out the integration as follows (ref. 4):

$$\tan\theta(x) = \frac{1}{c} \int_{x_{i-1}}^{x} \left[\varepsilon_{i-1} - (\varepsilon_{i-1} - \varepsilon_i) \frac{x - x_{i-1}}{\Delta l} \right] dx + \tan\theta_{i-1}$$

$$= \frac{1}{c} \left[\varepsilon_{i-1}(x - x_{i-1}) - (\varepsilon_{i-1} - \varepsilon_i) \frac{(x - x_{i-1})^2}{2\Delta l} \right] + \tan\theta_{i-1} \tag{B-3}$$

At the strain-sensing station, x_i, one can write $x_i - x_{i-1} \equiv \Delta l$, and equation (B-3) yields the slope, $\tan\theta_i [\equiv \tan\theta(x_i)]$, at the strain-sensing station, x_i, as

$$\tan\theta_i [\equiv \tan\theta(x_i)] = \frac{1}{c} \left[\varepsilon_{i-1}(\Delta l) - (\varepsilon_{i-1} - \varepsilon_i) \frac{(\Delta l)^2}{2\Delta l} \right] + \tan\theta_{i-1} \tag{B-4}$$

After grouping the terms, equation (B-4) takes on the final form of the slope equation for the uniform beam as

$$\tan\theta_i = \frac{\Delta l}{2c}\left(\varepsilon_{i-1} + \varepsilon\right) + \tan\theta_{i-1} \quad ; \quad \left(i = 1, 2, 3, ..., n\right) \tag{B-5}$$

which is equation (7) in the text.

Deflection Equations

The deflection, $y(x)$, of the uniform beam in the region, $x_{i-1} \le x \le x_i$, between the two adjacent strain-sensing stations, $\{x_{i-1}, x_i\}$, can be obtained by integrating slope equation (B-1) with the constant of integration determined by enforcing the continuity of deflection at the inboard adjacent strain-sensing station, x_{i-1}, as

$$y(x) = \underbrace{\int_{x_{i-1}}^{x}\tan\theta(x)dx}_{\substack{\text{Integration of slope}}} + \underbrace{y_{i-1}}_{\substack{\text{Deflection}\\\text{at } x_{i-1}}} = \underbrace{\int_{x_{i-1}}^{x}\int_{x_{i-1}}^{x}\frac{\varepsilon(x)}{c}dxdx}_{\substack{\text{Deflection increment}}} + \underbrace{\int_{x_{i-1}}^{x}\tan\theta_{i-1}dx}_{\substack{\text{Deflection at } x\\\text{due to }\tan\theta_{i-1}}} + \underbrace{y_{i-1}}_{\substack{\text{Deflection}\\\text{at } x_{i-1}}} \quad ; \quad x_{i-1} \le x \le x_i \tag{B-6}$$

Substitute equation (B-2) into equation (B-6), and carry out the integration as follows (ref. 4):

$$\begin{aligned}
y(x) &= \int_{x_{i-1}}^{x}\left\{\frac{1}{c}\int_{x_{i-1}}^{x}\left[\varepsilon_{i-1} - (\varepsilon_{i-1} - \varepsilon_i)\frac{x - x_{i-1}}{\Delta l}\right]dx + \tan\theta_{i-1}\right\}dx + y_{i-1} \\
&= \int_{x_{i-1}}^{x}\left\{\frac{1}{c}\left[\varepsilon_{i-1}(x - x_{i-1}) - (\varepsilon_{i-1} - \varepsilon_i)\frac{(x - x_{i-1})^2}{2\Delta l}\right] + \tan\theta_{i-1}\right\}dx + y_{i-1} \\
&= \frac{1}{c}\left[\varepsilon_{i-1}\frac{(x - x_{i-1})^2}{2} - (\varepsilon_{i-1} - \varepsilon_i)\frac{(x - x_{i-1})^3}{6\Delta l}\right] + (x - x_{i-1})\tan\theta_{i-1} + y_{i-1}
\end{aligned} \tag{B-7}$$

At the strain-sensing station, x_i, one can write $x_i - x_{i-1} \equiv \Delta l$, and equation (B-7) yields the deflection, $y_i[\equiv y(x_i)]$, at the strain-sensing station, x_i, as

$$y_i \equiv y(x_i) = \frac{1}{c}\left[\varepsilon_{i-1}\frac{(\Delta l)^2}{2} - (\varepsilon_{i-1} - \varepsilon_i)\frac{(\Delta l)^3}{6\Delta l}\right] + (\Delta l)\tan\theta_{i-1} + y_{i-1} \tag{B-8}$$

After grouping the terms, equation (B-8) takes on the final form of the deflection equation for the uniform beam as

$$y_i = \frac{(\Delta l)^2}{6c}\left(2\varepsilon_{i-1} + \varepsilon_i\right) + \Delta l\tan\theta_{i-1} + y_{i-1} \quad ; \quad \left(i = 1, 2, 3, ..., n\right) \tag{B-9}$$

which is equation (10) in the text.

66

APPENDIX C
DEFLECTION EQUATIONS WITH SHEAR EFFECTS

For a long cantilever beam, the contribution of deflection caused by transverse-shear effect is usually very small. If the transverse-shear effect is desired, however, additional transverse-shear–induced deflection terms must be added to deflection equation (12).

If V_i is the local shear force acting vertically at the strain-sensing station, x_i, then the averaged shear strain, $\bar{\gamma}_{i-1}$, at the strain-sensing stations, x_{i-1}, induced by V_i at the strain-sensing station, x_i, is given by

$$\bar{\gamma}_{i-1} = \frac{V_i}{AG} \tag{C-1}$$

in which A is the beam cross-sectional area, and G is the shear modulus.

The segment-wise transverse-shear–induced deflection at station x_i relative to station x_{i-1} can be written as $(\Delta l)\bar{\gamma}_{i-1}$. The total transverse-shear–induced deflection, y_i^s, at station x_i is then obtained by summing up all the segment-wise deflections from the support station $j = 0$ up to $j = (i-1)$. Namely,

$$y_i^s = (\Delta l)(\bar{\gamma}_0 + \bar{\gamma}_1 + \bar{\gamma}_2 + \bar{\gamma}_3 + \bar{\gamma}_4 + ... + \bar{\gamma}_{i-1}) \tag{C-2}$$

The transverse-shear–induced deflection, y_i^s, given in expression (C-2) can be added to the original cantilever beam deflection equation (12) to account for the shear effect:

$$y_i^s \text{ (transverse-shear effect term)}$$

$$y_1 = \frac{\Delta l^2}{6c}(2\varepsilon_0 + \varepsilon_1) \qquad\qquad +(\Delta l)\bar{\gamma}_o \tag{C-3a}$$

$$y_2 = \frac{\Delta l^2}{6c}(5\varepsilon_0 + 6\varepsilon_1 + \varepsilon_2) \qquad\qquad +(\Delta l)(\bar{\gamma}_0 + \bar{\gamma}_1) \tag{C-3b}$$

$$y_3 = \frac{\Delta l^2}{6c}\left[8\varepsilon_0 + 6(2\varepsilon_1 + \varepsilon_2) + \varepsilon_3\right] \qquad\qquad +(\Delta l)(\bar{\gamma}_0 + \bar{\gamma}_1 + \bar{\gamma}_2) \tag{C-3c}$$

$$y_4 = \frac{\Delta l^2}{6c}\left[11\varepsilon_0 + 6(3\varepsilon_1 + 2\varepsilon_2 + \varepsilon_3) + \varepsilon_4\right] \qquad\qquad +(\Delta l)(\bar{\gamma}_0 + \bar{\gamma}_1 + \bar{\gamma}_2 + \bar{\gamma}_3 \tag{C-3d}$$

……………...………………..

67

$$y_n = \frac{(\Delta l)^2}{6c}\left[(3n-1)\varepsilon_0 + 6\sum_{i=1}^{n-1}(n-i)\varepsilon_i + \varepsilon_n\right] \ + \ (\Delta l)(\bar{\gamma}_0 + \bar{\gamma}_1 + \bar{\gamma}_2 + \bar{\gamma}_3 + \bar{\gamma}_4 + \dots + \bar{\gamma}_{n-1}) \quad \text{(C-3e)}$$

If the uniform cantilever beam is loaded by the vertical tip load, P, then the segment-wise shear strains will be constant along the beam span. Namely,

$$\bar{\gamma}_0 = \bar{\gamma}_1 = \bar{\gamma}_2 = \bar{\gamma}_3 = \bar{\gamma}_4 = \dots = \bar{\gamma}_{n-1} \tag{C-4}$$

Then, in light of equation (C-4), deflection equation (C-3) becomes

$$y_i^s \text{ (transverse-shear effect term)}$$

$$y_1 = \frac{\Delta l^2}{6c}\left(2\varepsilon_0 + \varepsilon_1\right) \qquad\qquad +(\Delta l)\bar{\gamma}_0 \tag{C-5a}$$

$$y_2 = \frac{\Delta l^2}{6c}\left(5\varepsilon_0 + 6\varepsilon_1 + \varepsilon_2\right) \qquad\qquad +2(\Delta l)\bar{\gamma}_0 \tag{C-5b}$$

$$y_3 = \frac{\Delta l^2}{6c}\left[8\varepsilon_0 + 6\left(2\varepsilon_1 + \varepsilon_2\right) + \varepsilon_3\right] \qquad\qquad +3(\Delta l)\bar{\gamma}_0 \tag{C-5c}$$

$$y_4 = \frac{\Delta l^2}{6c}\left[11\varepsilon_0 + 6\left(3\varepsilon_1 + 2\varepsilon_2 + \varepsilon_3\right) + \varepsilon_4\right] \qquad\qquad +4(\Delta l)\bar{\gamma}_0 \tag{C-5d}$$

………………...………………..

$$y_n = \frac{(\Delta l)^2}{6c}\left[(3n-1)\varepsilon_0 + 6\sum_{i=1}^{n-1}(n-i)\varepsilon_i + \varepsilon_n\right] \qquad\qquad +n(\Delta l)\bar{\gamma}_0 \tag{C-5e}$$

APPENDIX D
INTEGRATIONS OF SLOPE AND DEFLECTION EQUATIONS FOR
TAPERED BEAMS

This section explains the details of the integrations of slope equation (22) and deflection equation (24) for tapered beams. These details provide the steps that result in the final mathematical forms given by equations (23) and (25), respectively.

Slope Equations

The slope, $\tan\theta(x)$, of the tapered beam in the region, $x_{i-1} \leq x \leq x_i$, between the two adjacent strain-sensing stations, $\{x_{i-1}, x_i\}$, can be obtained by integrating equation (3) (c is replaced with $c(x)$) with the constant of integration determined by enforcing the continuity of slope at the inboard adjacent strain-sensing station, x_{i-1}, as

$$\tan\theta(x) = \underbrace{\int_{x_{i-1}}^{x} \frac{d^2y}{dx^2} dx}_{\text{Slope increment}} + \underbrace{\tan\theta_{i-1}}_{\text{Slope at } x_{i-1}} = \int_{x_{i-1}}^{x} \frac{\varepsilon(x)}{c(x)} dx + \tan\theta_{i-1} \quad ; \quad x_{i-1} \leq x \leq x_i \tag{D-1}$$

In the region, $x_{i-1} \leq x \leq x_i$, between the two adjacent strain-sensing stations, $\{x_{i-1}, x_i\}$, the strain, $\varepsilon(x)$, and beam half depth, $c(x)$, are assumed to be of the following linear functions:

$$\varepsilon(x) = \varepsilon_{i-1} - (\varepsilon_{i-1} - \varepsilon_i)\frac{x - x_{i-1}}{\Delta l} \tag{D-2}$$

$$c(x) = c_{i-1} - (c_{i-1} - c_i)\frac{x - x_{i-1}}{\Delta l} \tag{D-3}$$

Substitute equations (D-2) and (D-3) into equation (D-1), and carry out the integration as follows (ref. 4):

$$\tan(x) = \int_{x_{i-1}}^{x} \left[\frac{\varepsilon_{i-1} - (\varepsilon_{i-1} - \varepsilon_i)\dfrac{x - x_{i-1}}{\Delta l}}{c_{i-1} - (c_{i-1} - c_i)\dfrac{x - x_{i-1}}{\Delta l}} \right] dx + \tan\theta_{i-1}$$

$$= \frac{\varepsilon_{i-1} - \varepsilon_i}{(c_{i-1} - c_i)}(x - x_{i-1}) + \frac{\dfrac{c_{i-1}(\varepsilon_{i-1} - \varepsilon_i)}{\Delta l} - \dfrac{\varepsilon_{i-1}(c_{i-1} - c_i)}{\Delta l}}{\dfrac{(c_{i-1} - c_i)^2}{(\Delta l)^2}} \left\{ \log\left[-\frac{(c_{i-1} - c_i)}{\Delta l}(x - x_{i-1}) + c_{i-1} \right] \right.$$

$$\left. - \log c_{i-1} \right\} + \tan\theta_{i-1}$$

$$= \frac{\varepsilon_{i-1} - \varepsilon_i}{(c_{i-1} - c_i)}(x - x_{i-1}) + \Delta l \frac{\varepsilon_{i-1}c_i - \varepsilon_i c_{i-1}}{(c_{i-1} - c_i)^2} \left\{ \log\left[-\frac{(c_{i-1} - c_i)}{\Delta l}(x - x_{i-1}) + c_{i-1} \right] \right.$$

$$\left. - \log c_{i-1} \right\} + \tan\theta_{i-1} \tag{D-4}$$

At the strain-sensing station, x_i, one can write $x_i - x_{i-1} \equiv \Delta l$, and equation (D-4) yields the slope, $\tan\theta_i [\equiv \tan\theta(x_i)]$, at the strain-sensing station, x_i, as

$$\tan\theta_i \equiv \tan\theta(x_i) = \frac{\varepsilon_{i-1} - \varepsilon_i}{(c_{i-1} - c_i)}\Delta l + \Delta l \frac{\varepsilon_{i-1}c_i - \varepsilon_i c_{i-1}}{(c_{i-1} - c_i)^2}\left(\log c_i - \log c_{i-1}\right) + \tan\theta_{i-1} \tag{D-5}$$

After grouping the term, one obtains the final form of the slope equation for tapered beams as

$$\tan\theta_i = \Delta l \left[\frac{\varepsilon_{i-1} - \varepsilon_i}{(c_{i-1} - c_i)} - \frac{\varepsilon_{i-1}c_i - \varepsilon_i c_{i-1}}{(c_{i-1} - c_i)^2}\log\frac{c_i}{c_{i-1}} \right] + \tan\theta_{i-1} \quad ; \quad (i = 1, 2, 3, ..., n) \tag{D-6}$$

which is equation (23) in the text.

Deflection Equations

The deflection, $y(x)$, of the tapered beam in the region, $x_{i-1} \le x \le x_i$, between the two adjacent strain-sensing stations, $\{x_{i-1}, x_i\}$, can be obtained by integrating slope equation (D-1) with the constant of integration determined by enforcing the continuity of deflection at the inboard adjacent strain-sensing station, x_{i-1}, as

$$y(x) = \underbrace{\int_{x_{i-1}}^{x} \tan\theta(x)dx}_{\text{Integration of slope}} + \underbrace{y_{i-1}}_{\substack{\text{Deflection} \\ \text{at } x_{i-1}}} = \underbrace{\int_{x_{i-1}}^{x}\int_{x_{i-1}}^{x} \frac{\varepsilon(x)}{c(c)}dxdx}_{\text{Deflection increment}} + \underbrace{\int_{x_{i-1}}^{x} \tan\theta_{i-1}dx}_{\substack{\text{Deflection at } x \\ \text{due to } \tan\theta_{i-1}}} + \underbrace{y_{i-1}}_{\substack{\text{Deflection} \\ \text{at } x_{i-1}}} \quad ; \quad x_{i-1} \le x \le x_i \tag{D-7}$$

Substitute equations (D-2) and (D-3) into equation (D-7), and carry out the integration as follows (ref. 4):

$$y(x) = \int_{x_{i-1}}^{x} \int_{x_{i-1}}^{x} \frac{\varepsilon_{i-1} - (\varepsilon_{i-1} - \varepsilon_i)\dfrac{x - x_{i-1}}{\Delta l}}{c_{i-1} - (c_{i-1} - c_i)\dfrac{x - x_{i-1}}{\Delta l}} \, dx + \int_{x_{i-1}}^{x} \tan\theta_{i-1} dx + y_{i-1}$$

$$= \int_{x_{i-1}}^{x_i} \left\{ \frac{\varepsilon_{i-1} - \varepsilon_i}{(c_{i-1} - c_i)}(x - x_{i-1}) + \Delta l \frac{\varepsilon_{i-1}c_i - \varepsilon_i c_{i-1}}{(c_{i-1} - c_i)^2} \left[\log\left(-\frac{(c_{i-1} - c_i)}{\Delta l}(x - x_{i-1}) + c_{i-1} \right) - \log c_{i-1} \right] \right\} dx$$

$$+ (x - x_{i-1})\tan\theta_{i-1} + y_{i-1}$$

$$= \frac{\varepsilon_{i-1} - \varepsilon_i}{2(c_{i-1} - c_i)}(x - x_{i-1})^2 + \Delta l \frac{\dfrac{\varepsilon_{i-1}c_i - \varepsilon_i c_{i-1}}{(c_{i-1} - c_i)^2}}{-\dfrac{(c_{i-1} - c_i)}{\Delta l}} \left[\frac{-(c_{i-1} - c_i)}{\Delta l}(x - x_{i-1}) + c_{i-1} \right]$$

$$\times \left\{ \left[\log\left(\frac{-(c_{i-1} - c_i)}{\Delta l}(x - x_{i-1}) + c_{i-1} \right) - \log c_{i-1} \right] - \left(-\frac{(c_{i-1} - c_i)}{\Delta l} \right)(x - x_{i-1}) \right\}$$

$$+ (x - x_{i-1})\tan\theta_{i-1} + y_{i-1}$$

$$(D\text{-}8)$$

At the strain-sensing station, x_i, one can write $x_i - x_{i-1} \equiv \Delta l$, and equation (D-8) yields the deflection $y_i [\equiv y(x_i)]$ at the strain-sensing station, x_i, as

$$y_i \equiv y(x_i) = \frac{\varepsilon_{i-1} - \varepsilon_i}{2(c_{i-1} - c_i)}(\Delta l)^2 - (\Delta l)^2 \frac{\varepsilon_{i-1}c_i - \varepsilon_i c_{i-1}}{(c_{i-1} - c_i)^3}$$

$$\times \left\{ \left[\frac{-(c_{i-1} - c_i)}{\Delta l}\Delta l + c_{i-1} \right] \left[\log\left(\frac{-(c_{i-1} - c_i)}{\Delta l}\Delta l + c_{i-1} \right) - \log c_{i-1} \right] + \frac{(c_{i-1} - c_i)}{\Delta l}\Delta l \right\}$$

$$+ \Delta l \tan\theta_{i-1} + y_{i-1}$$

$$= (\Delta l)^2 \left\{ \frac{\varepsilon_{i-1} - \varepsilon_i}{2(c_{i-1} - c_i)} - \frac{\varepsilon_{i-1}c_i - \varepsilon_i c_{i-1}}{(c_{i-1} - c_i)^3} \left[c_i \left(\log c_i - \log c_{i-1} \right) + (c_{i-1} - c_i) \right] \right\} + \Delta l \tan\theta_{i-1} + y_{i-1}$$

$$(D\text{-}9)$$

which can be written in a final form of the deflection equation for tapered beams as

$$y_i = (\Delta l)^2 \left\{ \frac{\varepsilon_{i-1} - \varepsilon_i}{2(c_{i-1} - c_i)} - \frac{\varepsilon_{i-1}c_i - \varepsilon_i c_{i-1}}{(c_{i-1} - c_i)^3} \left[c_i \log \frac{c_i}{c_{i-1}} + (c_{i-1} - c_i) \right] \right\} + \Delta l \tan\theta_{i-1} + y_{i-1}$$

$$(i = 1, 2, 3, ..., n)$$

$$(D\text{-}10)$$

which is equation (25) in the text.

APPENDIX E
EXPANSIONS OF LOGARITHMIC TERMS

When the cantilever beam is slightly tapered (that is, $c_i \to c_{i-1}$), the logarithmic terms in slope equation (23) and deflection equation (25) will approach zero [that is, $\log(c_i/c_{i-1}) \to 0$]. Therefore, the perturbation method must be used to expand the logarithmic term, $\log(c_i/c_{i-1})$, in the neighborhood of $(c_i/c_{i-1}) \approx 1$ to yield nonzero mathematical expressions, which are derived in this section.

Expansion of $\log(c_i/c_{i-1})$ for Slope Equation

When the beam is slightly tapered (that is, $c_i \to c_{i-1}$), the logarithmic term $\log(c_i/c_{i-1})$ can be expanded in series in the neighborhood of $c_i/c_{i-1} \approx 1$ (that is, $\log(c_i/c_{i-1}) \approx 0$) (ref. 4) as follows:

$$
\begin{aligned}
\log\frac{c_i}{c_{i-1}} &\approx \left(\frac{c_i}{c_{i-1}} - 1\right) - \frac{1}{2}\left(\frac{c_i}{c_{i-1}} - 1\right)^2 + \frac{1}{3}\left(\frac{c_i}{c_{i-1}} - 1\right)^3 - \dotso \\
&\approx \frac{c_i - c_{i-1}}{c_{i-1}}\left[1 - \frac{c_i - c_{i-1}}{2c_{i-1}} + \frac{(c_i - c_{i-1})^2}{3c_{i-1}^2}\right] - \dotso
\end{aligned}
\qquad ; \quad \frac{c_i}{c_{i-1}} \to 1 \qquad \text{(E-1)}
$$

Retaining the terms up to the second order terms in $(c_{i-1} - c_i)^2$, the logarithmic term $\log(c_i/c_{i-1})$ becomes the following form when c_i approaches c_{i-1} ($c_i \to c_{i-1}$):

$$
\log\frac{c_i}{c_{i-1}} \approx \frac{c_{i-1} - c_i}{2c_{i-1}^2}(c_i - 3c_{i-1}) \quad ; \quad \frac{c_i}{c_{i-1}} \to 1 \qquad \text{(E-2)}
$$

Equation (E-2) is identical to equation (26) in the text.

Expansion of $\left[c_i\log(c_i/c_{i-1}) + (c_{i-1} - c_i)\right]$ for Deflection Equation

When the beam is slightly tapered (that is, $c_i \to c_{i-1}$), the term, $\left[c_i\log(c_i/c_{i-1}) + (c_{i-1} - c_i)\right]$, in deflection equation (25) can be expanded in the neighborhood of $(c_i/c_{i-1}) \approx 1$ (that is, $\log(c_i/c_{i-1}) \approx 0$). In light of the $\log(c_i/c_{i-1})$ expansion equation (E-1), the expansion of $\left[c_i\log(c_i/c_{i-1}) + (c_{i-1} - c_i)\right]$ can be carried out up to the third order terms in $(c_{i-1} - c_i)^3$ when c_i approaches c_{i-1} ($c_i \to c_{i-1}$) as follows (ref. 4):

$$\left[c_i \log\left(\frac{c_i}{c_{i-1}}\right) + (c_{i-1} - c_i)\right] \approx c_i\left[\left(\frac{c_i}{c_{i-1}} - 1\right) - \frac{1}{2}\left(\frac{c_i}{c_{i-1}} - 1\right)^2 + \frac{1}{3}\left(\frac{c_i}{c_{i-1}} - 1\right)^3 - ...... \right] + (c_{i-1} - c_i)$$

$$\approx -\frac{c_i}{c_{i-1}}\left[(c_{i-1} - c_i) + \frac{(c_{i-1} - c_i)^2}{2c_{i-1}} + \frac{(c_{i-1} - c_i)^3}{3c_{i-1}^2} - ...... - \frac{c_{i-1}}{c_i}(c_{i-1} - c_i)\right]$$

$$\approx -\frac{c_i}{c_{i-1}}\left[(c_{i-1} - c_i)\left(1 - \frac{c_{i-1}}{c_i}\right) + \frac{(c_{i-1} - c_i)^2}{2c_{i-1}} + \frac{(c_{i-1} - c_i)^3}{3c_{i-1}^2} + ... \right]$$

$$\approx -\frac{c_i}{c_{i-1}}\left[-\frac{(c_{i-1} - c_i)^2}{c_i} + \frac{(c_{i-1} - c_i)^2}{2c_{i-1}} + \frac{(c_{i-1} - c_i)^3}{3c_{i-1}^2} + ... \right]$$

$$\approx -\frac{(c_{i-1} - c_i)^2}{6c_{i-1}}\left[-6 + 3\frac{c_i}{c_{i-1}} + 2\frac{c_i}{c_{i-1}^2}(c_{i-1} - c_i) + ... \right]$$

$$\approx \frac{(c_{i-1} - c_i)^2}{6c_{i-1}}\left[3 + 3 - 3\frac{c_i}{c_{i-1}} - 2\frac{c_i}{c_{i-1}^2}(c_{i-1} - c_i) + ... \right]$$

$$\approx \frac{(c_{i-1} - c_i)^2}{6c_{i-1}}\left[3 + 3\frac{(c_{i-1} - c_i)}{c_{i-1}} - 2\frac{c_i}{c_{i-1}^2}(c_{i-1} - c_i) + ... \right]$$

$$\approx \frac{(c_{i-1} - c_i)^2}{6c_{i-1}}\left[3 + \frac{(c_{i-1} - c_i)}{c_{i-1}} + 2\frac{(c_{i-1} - c_i)}{c_{i-1}} - 2\frac{c_i}{c_{i-1}^2}(c_{i-1} - c_i) + ... \right]$$

$$\approx \frac{(c_{i-1} - c_i)^2}{6c_{i-1}}\left[3 + \frac{(c_{i-1} - c_i)}{c_{i-1}} + 2\frac{(c_{i-1} - c_i)^2}{c_{i-1}^2} + ... \right] \quad ; \quad \frac{c_i}{c_{i-1}} \to 1$$

(E-3)

Neglecting the forth order term in $(c_{i-1} - c_i)^4$, one obtains the following final expression for $\left[c_i \log(c_i/c_{i-1}) + (c_{i-1} - c_i)\right]$ when c_i approaches c_{i-1} $(c_i \to c_{i-1})$:

$$\left[\log\frac{c_i}{c_{i-1}} + (c_{i-1} - c_i)\right] \approx \frac{(c_{i-1} - c_i)^2}{6c_{i-1}}\left[3 + \frac{(c_{i-1} - c_i)}{c_{i-1}}\right] \quad ; \quad \frac{c_i}{c_{i-1}} \to 1 \qquad \text{(E-4)}$$

which is equation (29) in the text.

REFERENCES

1. DeAngelis, V. Michael, and Fodale, Robert, "Electro-Optical Flight Deflection Measurement Systems," *Society of Flight Test Engineers 18th Annual Symposium*, Paper No. 22, Amsterdam, Netherlands, Sept. 1987.

2. Roark, Raymond J., *Formulas for Stress and Strain*, Third Edition, McGraw-Hill Book Company, Inc., New York, 1954.

3. Faupel, Joseph H., *Engineering Design: A Synthesis of Stress Analysis and Materials Engineering*, John Wiley and Sons, Inc., New York, 1964.

4. Hodgman, Charles D., *Standard Mathematical Tables*, Eleventh Edition, Chemical Rubber Publishing Company, Cleveland, Ohio, 1957.

5. Whetstone, W.D., *SPAR Structural Analysis System Reference Manual*, System Level 13A, Vol. 1, Program Execution, NASA CR-158970-1-VOL-1, 1978.

1. REPORT DATE *(DD-MM-YYYY)*	2. REPORT TYPE	3. DATES COVERED *(From - To)*
01-10-2007	Technical Publication	

4. TITLE AND SUBTITLE	5a. CONTRACT NUMBER
Displacement Theories for In-Flight Deformed Shape Predictions of Aerospace Structures	
	5b. GRANT NUMBER
	5c. PROGRAM ELEMENT NUMBER
6. AUTHOR(S)	5d. PROJECT NUMBER
William L. Ko; W. L. Richards; and Van T. Tran	
	5e. TASK NUMBER
	5f. WORK UNIT NUMBER

7. PERFORMING ORGANIZATION NAME(S) AND ADDRESS(ES)	8. PERFORMING ORGANIZATION REPORT NUMBER
NASA Dryden Flight Research Center (DFRC) P.O. Box 273 Edwards, California 93523-0273	H-2652

9. SPONSORING/MONITORING AGENCY NAME(S) AND ADDRESS(ES)	10. SPONSORING/MONITOR'S ACRONYM(S)
National Aeronautics and Space Administration Washington, DC 20546-0001	NASA
	11. SPONSORING/MONITORING REPORT NUMBER
	NASA/TP-2007-214612

12. DISTRIBUTION/AVAILABILITY STATEMENT

Unclassified -- Unlimited
Subject Category -- 39   Availability: NASA CASI (301) 621-0390   Distribution: Standard

13. SUPPLEMENTARY NOTES

Ko, Richards, and Tran, NASA Dryden. The invention described in this report is the subject of a currently pending patent application: Real-Time Structural Shape Sensing Techniques using Surface Strain Sensor Measurements (Inventors: William Leslie Ko and W. Lance Richards) before the U.S. Patent and Trademark Office.

14. ABSTRACT

Displacement theories are developed for a variety of structures with the goal of providing real-time shape predictions for aerospace vehicles during flight. These theories are initially developed for a cantilever beam to predict the deformed shapes of the Helios flying wing. The main structural configuration of the Helios wing is a cantilever wing tubular spar subjected to bending, torsion, and combined bending and torsion loading. The displacement equations that are formulated are expressed in terms of strains measured at multiple sensing stations equally spaced on the surface of the wing spar. Displacement theories for other structures, such as tapered cantilever beams, two-point supported beams, wing boxes, and plates also are developed. The accuracy of the displacement theories is successfully validated by finite-element analysis and classical beam theory using input-strains generated by finite-element analysis. The displacement equations and associated strain-sensing system (such as fiber optic sensors) create a powerful means for in-flight deformation monitoring of aerospace structures. This method serves multiple purposes for structural shape sensing, loads monitoring, and structural health monitoring. Ultimately, the calculated displacement data can be visually displayed to the ground-based pilot or used as input to the control system to actively control the shape of structures during flight.

15. SUBJECT TERMS

Deflection equations, Displacement theories, Embedded strain sensing, In-flight shape predictions, Slope equations

16. SECURITY CLASSIFICATION OF:			17. LIMITATION OF ABSTRACT	18. NUMBER OF PAGES	19a. NAME OF RESPONSIBLE PERSON
a. REPORT	b. ABSTRACT	c. THIS PAGE			STI Help Desk (email: help@sti.nasa.gov)
					19b. TELEPHONE NUMBER *(Include area code)*
U	U	U	UU	82	(301) 621-0390